“Mechanistic insights into carbon monoxide and CoA binding at the Ni,Ni-[4Fe-4S] active site of the acetyl-CoA synthase from *Carboxydothermus hydrogenoformans*”

Dissertation

zur Erlangung des akademischen Grades

docter rerum naturalium

(Dr. rer. nat.)

eingereicht an der

Lebenswissenschaftlichen Fakultät

der Humboldt-Universität zu Berlin

von

M.Sc. Julian Kreibich

Präsident der Humboldt-Universität zu Berlin

Prof. Dr.-Ing. Dr. Sabine Kunst

Dekan der Lebenswissenschaftlichen Fakultät

Prof. Dr. Dr. Christian Ulrichs

Gutachter/innen:

1. Prof. Dr. Holger Dobbek
2. Prof. Dr. Maria Andrea Mroginski
3. Prof. Dr. Christian Limberg

Tag der mündlichen Prüfung: 09.08.2021

Table of Contents

Zusammenfassung

Die Acetyl-CoA Synthase (ACS) beinhaltet ein einzigartiges [4Fe-4S]-(μ_2-SCys)-[Ni((μ_2-SCys)$_2$Gly)Ni] Metallcluster (Cluster A) in seinem aktiven Zentrum, welches wichtig für ein autotrophes Wachstum von Bakterien und Archaeen ist, die den reduktiven Acetyl-CoA-Weg zur Energiekonservierung oder Kohlenstofffixierung nutzen. Der letzte Schritt dieses Syntheseweges wird von der ACS am proximal zum [4Fe-4S] Cluster liegenden Ni ion katalysiert (Ni_p), in dessen Kondensationsreaktion aus CO, CoA und einem Methylkation Acetyl-CoA synthetisiert wird.

In meiner Arbeit wurde die monomere ACS von *Carboxydothermus hydrogenoformans* (ACS_{Ch}) heterolog in *Escherichia coli* exprimiert und aufgereinigt. Diese zeigte ein vollständig besetztes [4Fe-4S] Cluster, jedoch keine vollständige Besetzung der beiden Ni-Positionen, im Cluster A. Eine aktive ACS_{Ch} mit einem vollständig besetzten und intakten Cluster A konnte mithilfe chemischer Rekonstitution generiert werden, seine Ligandenbindung untersucht und in verschiedenen Konformationen kristallisiert werden.

Um die Interaktion der ACS_{Ch} mit seinen Substraten besser zu verstehen, wurde ACS_{Ch} in drei verschiedenen Stadien kristallisiert. Zuerst wurde die aufgereinigte ACS_{Ch} in einer neuen Konformation kristallisiert und deren Struktur mit einer Auflösung von 2.1 Å mit der Raumgruppe $P2_12_12_1$ bestimmt. Diese Konformation ($ACS_{Ch\text{-}closed}$) wies einen geringeren Kontakt zur Solventumgebung auf als die vorher bekannte Struktur der ACS_{Ch} ($ACS_{Ch\text{-}open}$, PDB-ID: 1RU3). Das aktive Zentrum des Clusters A der $ACS_{Ch\text{-}closed}$ unterscheidet sich von der $ACS_{Ch\text{-}open}$ in der Koordination des Ni_p, welches verzerrt tetraedrisch koordiniert in $ACS_{Ch\text{-}closed}$ vorliegt und quadratisch planar in $ACS_{Ch\text{-}open}$, wobei die Liganden in beiden Konformationen identisch sind. Eine Analyse des Modells wies einen molekularen Tunnel auf, der nur in $ACS_{Ch\text{-}closed}$ vorhanden ist, welcher als CO-Kanal zur Substratversorgung dienen könnte und besitzt einen zusätzlichen Schließmechanismus, welcher durch die Bewegung von Phe_{515} zwischen $ACS_{Ch\text{-}open}$ und $ACS_{Ch\text{-}closed}$ gesteuert wird.

Zweitens wurde die Kristallstruktur einer CO gebunden $ACS_{Ch\text{-}closed}$ mit einer Auflösung von 2.0 Å gelöst. Darin wurde eine Elektronendichte am Ni_p identifiziert, die zu einem zweiatomigen Liganden passt. Die Modellierung dieser Elektronendichte mit CO führte zu einer überzeugenden Beschreibung der Elektronendichte. CO bindet am ebenfalls verzerrt tetraedrisch koordinierten Ni_p anstelle eines Wassermoleküls. Im Vergleich zu $ACS_{Ch\text{-}closed}$ unterscheidet sich die CO gebundene Struktur nur geringfügig sowohl vom Cluster A als auch von der Gesamtstruktur des Proteins. Dies weist darauf hin, dass die Konformation der $ACS_{Ch\text{-}closed}$ sich in einem Stadium befindet, welches bereit für die CO

Bindung ist. Die Konformationsänderung von $ACS_{Ch\text{-}open}$ zu $ACS_{Ch\text{-}closed}$ ist dabei der entscheidende Schritt, um CO zur katalytischen Bindungsstelle zu leiten.

Weiterhin wurde Ni rekonstituierte ACS_{Ch} mit CoA kokristallisiert. Die daraus folgende CoA gebundene ACS_{ch} Struktur mit der Raumgruppe $H3_2$ wurde mit einer Auflösung von 2.3 Å gelöst und zeigt ACS_{Ch} in der offenen Konformation mit einer zusätzlichen positiven Elektronendichte über dem Ni_p des Cluster A. Die Gesamtstruktur der CoA gebundenen ACS_{Ch} ist vergleichbar mit der $ACS_{Ch\text{-}open}$ Struktur. CoA bindet am Ni_p über seine Thiolgruppe und erstreckt sich zwischen zwei Domänen, wobei Ni_p quadratisch planar koordiniert wird. Die Gegenwart von CoA wurde mit Berechnungen verschiedener Elektronendichte-Karten für CoA: *feature-enhanced*, *omit* und *polder maps* zusätzlich validiert und gibt damit erste Einsichten in die Interaktion und Koordinierung von CoA in ACS_{Ch}.

Die Bindung von CO und CoA an ACS_{Ch} wurde zudem mittels isothermaler Titrationskalorimetrie weiter charakterisiert. Dabei bindet CoA enthalpisch getrieben mit einem K_D von 3.1 µM und CO entropisch getrieben mit einem K_D von 9.4 µM an ACS_{Ch}. Der Konformationswechsel zwischen $ACS_{Ch\text{-}open}$ und $ACS_{Ch\text{-}closed}$ für die Bindung unterschiedlicher Substrate ist dabei wichtig für die Substratspezifität, welche mit einer Änderung der Koordination des Ni_p einhergehen. $ACS_{Ch\text{-}open}$ zeigt eine quadratisch planare Koordinierung des Ni_p und bietet genug Raum für eine CoA-Bindung. Im Vergleich dazu ist in $ACS_{Ch\text{-}closed}$ das Ni_p verzerrt tetraedrisch koordiniert und das Cluster A ist tiefer in der ACS_{Ch} verborgen. Dies resultiert in einem geringeren Kontakt mit der Solventumgebung und der Ausbildung einer hydrophoben Bindungstasche für die CO-Bindung, welche aus dem molekularen Tunnel in $ACS_{Ch\text{-}closed}$ zum aktiven Zentrum transportiert wird, wodurch die Bindung größerer Substrate wie CoA am Ni_p blockiert wird.

Die Ergebnisse dieser Arbeit verschaffen damit erste Einblicke in den Mechanismus der Substratbindung in ACS_{Ch} und unterstreicht die wichtige Funktion des Koordinierungswechsels des Ni_p für die Substratbindung, welche mit einer Domänenumlagerung der ACS_{Ch} einhergeht.

Abstract

The acetyl-CoA synthase (ACS) harbors a unique [4Fe-4S]-(μ_2-SCys)-[Ni((μ_2-SCys)$_2$Gly)Ni] cluster (cluster A) in its active site, which is important for bacteria and archaea to survive in autotrophic growth using the reductive acetyl-CoA pathway to conserve energy or fix carbon. The last step of this pathway is catalyzed by ACS in a final condensation reaction of CO, CoA and a methyl cation at the Ni_p, the Ni ion proximal to the [4Fe-4S] cluster.

In my study, the monomeric ACS of *Carboxydothermus hydrogenoformans* (ACS_{Ch}) was heterologously expressed in *Escherichia coli* and purified with [4Fe-4S] cluster, but lacking binuclear nickel. An intact and active cluster A containing binuclear Ni was generated by chemical reconstitution of ACS_{Ch}, which was used to study ligand binding and crystallized in different forms.

Crystal structures of three different states of ACS_{Ch} were resolved to understand how ACS accomplishes the interaction with those substrates. At first, as-isolated ACS_{Ch} structure was solved in a new conformation at d_{min} of 2.1 Å with a space group of $P2_12_12_1$ and less solvent exposed (called $ACS_{Ch\text{-}closed}$) than the known structure of ACS_{Ch} (called $ACS_{Ch\text{-}open}$, PDB-ID:1RU3). The active site cluster A of $ACS_{Ch\text{-}closed}$ differs to that of $ACS_{Ch\text{-}open}$ in the coordination of the proximal Ni, which is distorted tetrahedrally coordinated in $ACS_{Ch\text{-}closed}$ and square planar coordinated in $ACS_{Ch\text{-}open}$ without changing the coordinating ligands. Analysis of the model revealed a molecular tunnel that is only present in $ACS_{Ch\text{-}closed}$, which might act as CO channel for substrate delivery at the Ni_p site with an additional gating mechanism executed by the movement of the Phe_{515} between $ACS_{Ch\text{-}open}$ and $ACS_{Ch\text{-}closed}$ conformation.

Secondly, a CO-bound $ACS_{Ch\text{-}closed}$ crystal was obtained and solved at a resolution of 2.0 Å. An electron density fitting with a diatomic ligand at the Ni_p site was clearly identified and modeled as a CO molecule, which clearly satisfied the observed electron density. CO binds at the Ni_p site completing the tetrahedral coordination geometry of Ni_p by replacing a water molecule. Compared to $ACS_{Ch\text{-}closed}$, the CO-bound structure differs only slightly at cluster A and also in overall structure, indicating that the conformation observed in $ACS_{Ch\text{-}closed}$ is a ready state to bind CO and that the conformational switch between open and closed is responsible for CO migration and binding to the catalytic site.

Fully Ni-reconstituted ACS_{Ch} was co-crystallized with CoA. The CoA-bound ACS_{ch} structure was solved at 2.3 Å resolution in a space group of $H3_2$, depicting ACS_{Ch} in the open conformation with an additional positive electron density above Ni_p of cluster A. Overall structure of the CoA-bound ACS_{Ch} is similar to the $ACS_{Ch\text{-}open}$ state. CoA binds at the Ni_p site through its thiol group and flexibly extends to a gap between two domains, where the Ni_p shows square planar geometry. This was further supported by

calculating different electron density maps for CoA, feature-enhanced, omit and polder maps. This structure gives first insights into interaction and coordination of CoA inside ACS_{Ch}.

The binding of CO and CoA to ACS_{Ch} has been further characterized by isothermal calorimetry experiments. While CoA binding is enthalpically driven with a K_D of 3.1 µM, CO binds to ACS_{Ch} by entropic contribution with a K_D of 9.4 µM. The observed conformational switch between $ACS_{Ch\text{-}open}$ and $ACS_{Ch\text{-}closed}$ for the binding with different substrates is of importance in substrate specificity, accompanied by a different coordination of Ni_p. $ACS_{Ch\text{-}open}$ has a square planar coordination of Ni_p and enough space for CoA binding. In comparison, $ACS_{Ch\text{-}closed}$ depicts Ni_p in a distorted tetrahedral coordination and cluster A is more buried into the ACS_{Ch} interior, generating a hydrophobic binding pocket for CO that is delivered through the molecular tunnel in $ACS_{Ch\text{-}closed}$, consequently blocking access of large substrates like CoA.

The results of this work provide initial insights into the mechanism of substrate binding in ACS_{Ch} and point out the important role of the coordination switch of Ni_p coupled to domain rearrangement for substrate engagement.

1 Introduction

1.1 Nickel containing enzymes

Nature evolved biocatalysts which allows cells to perform a diverse range of chemical reactions to realize complex metabolism in cells. One way to obtain this variety is the complexation of transition metals in proteins. The chemical reactivity of the metal depends on the coordination geometry and oxidation state and proteins are used to coordinate metals in a framework to control these parameters. Additionally, metals play a crucial role in physiology and pathology of biological systems [1]. The composition of all life forms on earth consist of 25 essential elements including many metals e.g. Fe, Zn, Cu, Co, Se [2]. Bioinformatic studies of 1371 different enzymes with known structures show that 47% of these enzymes contain a metal and 40% of them do so at their catalytic site [3]. Metals are not only essential as catalysts for reactions, but they are also associated with proteins in storage and transport systems (e.g. methallothionine, Hpn and ferritin [4, 5]) as well as in signal transduction, regulation of transcription and chemotaxis [6]. Metallochaperones are a distinct class of chaperons that protect and facilitate the maturation of metalloproteins (e.g. HypA, Atx1, UreE [7-9]) and other metal binding proteins that are involved in the intracellular control of metal ions (e.g. Fur, NikR [10, 11]).

Although the metabolic importance of metals has been known since the beginning of the last century [12, 13], nickel was only discovered to be an important element in biological systems in 1965 [14]. Since then, nickel-associated proteins have been found in sensing, transport systems, acetogenesis and nickel insertion [15-18]. Despite the advantages of nickel as a transition metal, organisms have also to deal with the toxicity of nickel [19].

Thus far, eleven enzymes are known carrying nickel as an active site component: glyoxalase I from *Escherichia coli* [20], acireductone dioxygenase [21], urease [22], mononuclear nickel superoxide dismutase [23], [NiFe]-hydrogenase [24], carbon monoxide dehydrogenase (CODH) [25], acetyl-coenzyme A (CoA) synthase (ACS) [26], methyl-coenzyme M (CoM) reductase [27], lactate racemase [28], some quercetinase e.g. in *Streptomyces* sp. FLA [29] and glycerol-1-phosphate dehydrogenase from *Bacillus subtilis* [30]. The structural and catalytic complexity of these enzymes at the metal sites varies by the coordination and redox property, which ranges from mononuclear redox (in)active metals to heteronuclear metal cluster or a part of an organometallic cofactor (Fig. 1 and Tab. 1).

As depicted in Figure 1A-C, the nickel ion is in an octahedral geometry coordinated by His, Glu and water in the acireductone dioxygenase, quercetinase and glyoxalase I [31-33]. In urease, two nickel

ions are bridged by a carbamylated Lys and an additional water molecule. Each nickel ion is coordinated by two His residues, one of which is ligated by an additionally Asp residue. A water molecule completes coordination for each nickel as a square pyramidal and an octahedral (Fig. 1D) [34]. In the Ni-containing superoxide dismutase, the nickel ion is bound by an amide from a Cys residue, a primary amine from the N-terminus, two thiolate ligands from Cys residues and an additional His residue, forming a square pyramidal geometry (Fig. 1E) [35]. Upon reduction the Ni ion forms a square planar coordination by displacement of the His residue [36]. The lactate racemase from *Lactobacillus plantarum* uses the organic cofactor pyridinium-3-thioamide-5-thiocarboxylic acid mononucleotide, which is ligated by a lysine (Fig. 1F) to bind the nickel using two sulfur and the pyridinium C4 carbon atom and completes the nickel coordination by a histidine residue [37]. The nickel in the methyl-CoM reductase is mainly coordinated by the tetrapyrrole nitrogens in the porphyrin and only one axial coordination from a Gln residue, where the sixth axial coordination is lighted by CoM (Fig. 1G) [38]. In [NiFe]-hydrogenase the nickel ion is coordinated by four Cys thiolates and an oxygen, where two of the thiolates and the oxygen are bridged to the iron (Fig. 1H). The iron is further coordinated by two cyanide and one carbon monoxide [39]. Another hetero nuclear cluster with nickel in a protein is depicted in CODH and ACS (Fig. 1I and J), in which the nickel ion is part of a cluster consisting of other common metal clusters [40]. The [Ni4Fe4SOH$_x$] cluster (cluster C) of CODH can be described as a [3Fe-4S] cluster that is bridged to a Ni-Fe center and the nickel ion is coordinated by additional thiolates from Cys residues [41]. In ACS the [4Fe-4S]-(μ_2-SCys)-[Ni((μ_2-SCys)$_2$Gly)Ni] cluster (cluster A) consists of a [4Fe-4S] cluster bridged by a Cys residue to a binuclear Ni site. Both Ni ions are in a square planar coordination sphere. The Ni proximal to the [4Fe-4S] cluster is named proximal Ni (Ni$_p$) and coordinated by three Cys residues and a water ligand. In contrast, the distal Ni (Ni$_d$) is coordinated by two Cys residues and two nitrogen atoms from the protein backbone [40].

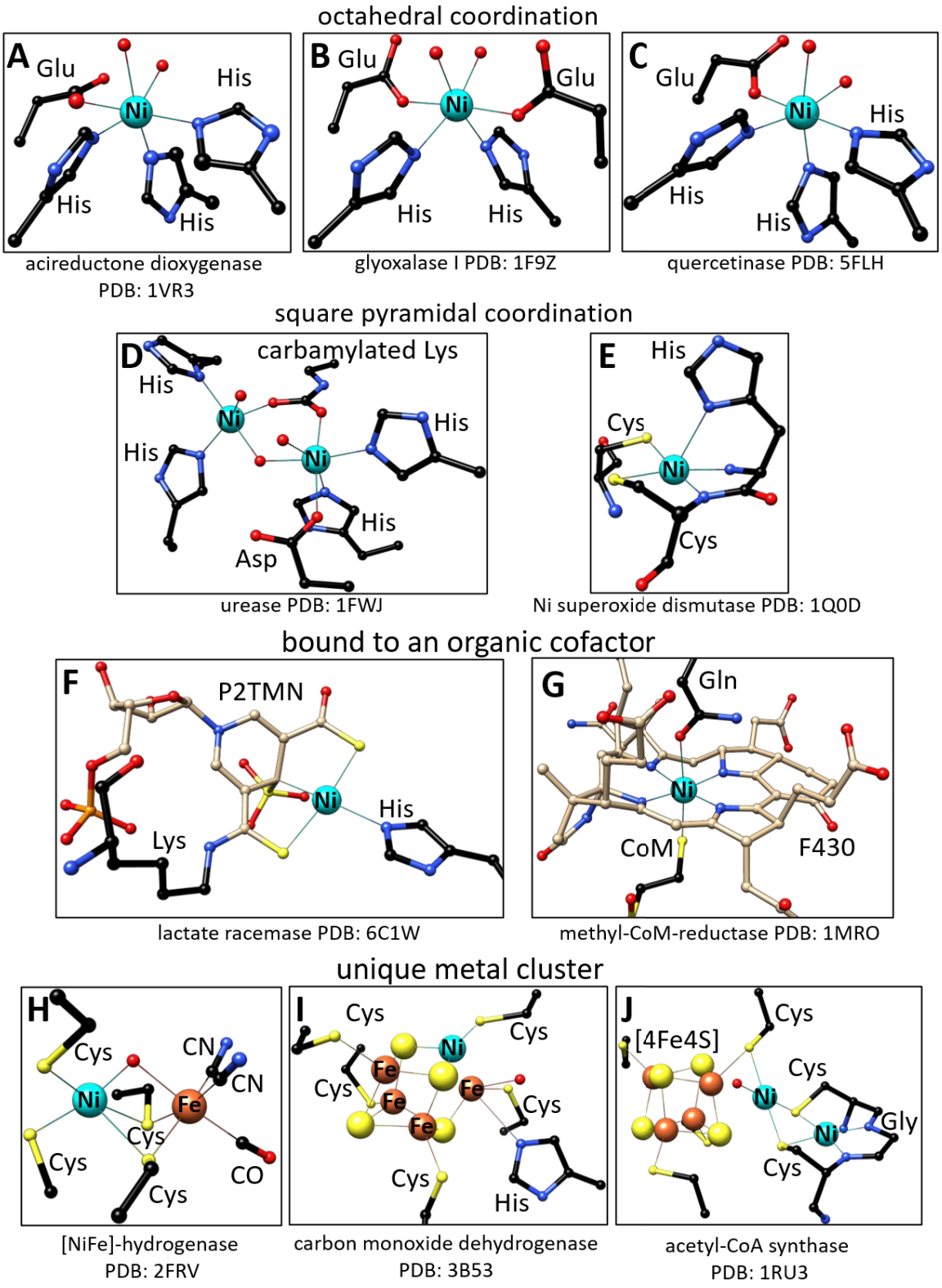

Figure 1: Schematic overview of nickel coordination in structural known nickel enzymes. The nickel ion is octahedral coordinated in the enzymes acireductone dioxygenase (A), glyoxalase I (B), quercetinase (C). A square pyramidal coordination is known for the enzymes urease (D) and Ni superoxide dismutase (E). An organic cofactor is bound to lactate racemase (F) and methyl-CoM-reductase (G). In [NiFe]-hydrogenase (H), CODH (I) and ACS (J) the nickel ion is part of a unique metal cluster. See text for detailed information. Atoms are color-coded distinctively: Fe in orange, Ni in cyan, C in black, N in blue, S in yellow, O in red, P in orange, C atoms of pyridinium-3,5-bisthiocarboxylic acid mononucleotide (P2TMN) and F430 are light brown.

Table 1: Nickel containing enzymes and their biochemical properties.

Enzyme	Biological importance	Reaction	Structural representative and redox activity
Glyoxalase I	Detoxification	Hemithioacetal ⇋ S-D-lactoylglutathione	mononuclear non-redox active
Acireductone dioxygenase	Methionine metabolism	1,2-dihydroxy-3-keto-5-methylthiopentene +O_2 ⇋ $HCOO^-$ +CO + 3-methylthiopropionate	mononuclear non-redox active
Urease	Nitrogen metabolism	$(NH_2)_2CO + H_2O$ ⇋ 2 $NH_4^+ + HCO_3^-$	mononuclear non-redox active
Nickel superoxide dismutase	Oxidative stress	$2O_2^- + 2H^+$ ⇋ $H_2O_2 + O_2$	mononuclear redox active
[NiFe]-hydrogenase	Energy metabolism	H_2 ⇋ 2 $H^+ + 2e^-$	hetero nuclear cluster redox active
ACS	Carbon metabolism	CH_3-Co(III)FeSP + CO + CoA-SH ⇋ Acetyl-CoA + Co(I)FeSP	hetero nuclear cluster redox active
CODH	Carbon metabolism	CO + H_2O ⇋ CO_2 + $2e^-$ + $2H^+$	hetero nuclear cluster redox active
Methyl-CoM reductase	Methane formation	CH_3-S-CoM + CoB-SH ⇋ CH_4 + CoM-S-S-CoB heterodisulfide	Organic cofactor redox active
Lactate racemase	Pyruvate metabolism	L-lactic acid ⇋ D-lactic acid	Organic cofactor
Quercetinase	Flavonoid degradation	Quercetin + O_2 ⇋ CO + H^+ + 2-protocatechuoylphloroglucinol carboxylic acid	mononuclear non-redox active
Glycerol-1-phosphate dehydrogenase	Phospholipid biosynthesis	*sn*-glycerol 1-phosphate + NADH ⇋ glycerone phosphate + NAD^+	not known

As shown in Table 1, nickel containing enzymes vary not only structurally, but they perform different enzymatic reactions (redox reaction, condensations and racemization) and the redox state of the Ni ion can be changed between Ni(0,+1,+2 and +3) states with a range of the potential of 1.5 V [42]. They play a crucial role in detoxification (glyoxalase I, nickel superoxide dismutase), carbon (ACS, CODH) and nitrogen (urease) metabolism and in the synthesis of important precursors (acireductone dioxygenase, lactate racemase, glycerol-1-phosphate dehydrogenase). Nevertheless, these proteins are often found to rely on additional helping proteins for nickel delivery, metallocentre assembly or for the synthesis of organic cofactors [43-45]. Genomic analysis of nickel metalloenzymes revealed that these enzymes are widely distributed among bacteria and archaea and the most common are urease and the [NiFe]-hydrogenase. Eucaryotes show nickel enzymes mostly in fungi and plants [46]. In animals, no physiologically relevant nickel dependent enzyme is known.

1.2 Autotrophic carbon fixation

Carbon is the most important element for all cells to build new biomass. Therefore, assimilation of carbon is one of the fundamental processes for all life forms on earth. There are two different types of carbon fixation: autotrophic and heterotrophic [47]. Organisms that can grow autotrophically are able to produce complex organic compounds from inorganic nutrients such as CO_2. They can be further divided into photoautotrophs and chemolithoautotrophs depending on their energy source. Photoautotrophs use light [48] and chemoautotrophic organisms can oxidize reduced inorganic compounds (chemolithotroph) or organic compounds like formate (chemoorganotroph) to provide the energy for CO_2 fixation [49]. The autotrophic carbon fixation is distributed among many prokaryotes and plants, which are able to assimilate carbon from inorganic CO_2 to build biomass. Through this assimilation, $2 \cdot 10^{11}$ t carbon is turned into organic compounds per year, which corresponds to 10 % of the CO_2 of the atmosphere. This biomass is an essential carbon source for heterotrophic organisms, which utilize organic carbon compounds for carbon fixation [50].

Table 2: Mechanisms for autotrophic carbon fixation. Table was modified from [51]

Metabolic pathway	ATP/ pyruvate	Reductant	CO_2-Fixing enzymes	Active CO_2 species	Oxygen sensitivity
Reductive pentose phosphate cycle	7	NADP(H)	RubisCO	CO_2	aerobic
Reductive citric acid cycle	2	NADP(H), Ferredoxin	2- Oxoglutarate synthase	CO_2	anaerobic, microaerobic
			Isocitrate dehydrogenase	CO_2	
			Pyruvate synthase	CO_2	
			PEP carboxylase	HCO_3^-	
3-hydroxypropionate bicycle	7	NAD(P)H	Acetyl-CoA and propionyl-CoA carboxylase	HCO_3^-	aerobic
3-hydroxypropionate-4-hydroxybutyrate cycle	9	NAD(P)H	Acetyl-CoA and propionyl-CoA carboxylase	HCO_3^-	microaerobic, anaerobic
Dicarboxylate-4-hydroxybutyrate cycle	5	NADP(H), ferredoxin	Pyruvate synthase	CO_2	anaerobic, microaerobic
			PEP carboxylase	HCO_3^-	
Reductive acetyl-CoA pathway	max. 1	NAD(P)H, ferredoxin, $F_{420}H_2$	Acetyl-CoA synthase-CO dehydrogenase	CO_2	strict anaerobic
			Formylmethanofuran dehydrogenase	CO_2	
			Pyruvate synthase	HCO_3^-	

There are six known autotrophic CO_2 fixation mechanisms: reductive pentose phosphate cycle, reductive citric acid cycle, 3-hydroxypropionate bicycle, 3-hydroxypropionate-4-hydroxybutyrate cycle, dicarboxylate-4-hydroxybutyrate cycle and the reductive acetyl-CoA pathway [52]. They all require energy and reducing agents to reduce CO_2 into a formaldehyde (Equation 1) [50].

$$CO_2 + 4[H] + n\,ATP \leftrightarrow (CH_2O) + H_2O + n\,ADP + n\,Phosphate \quad (1)$$

As shown in Table 2, the reductive acetyl-CoA pathway (also called Wood-Ljungdahl-pathway), is the most energy efficient autotrophic carbon fixation pathway, in which only one ATP is hydrolyzed to generate one molecule of pyruvate. Nevertheless, this pathway is used only by evolutionarily primitive organisms, including archaea and eubacteria [53].

1.2.1 Reductive acetyl-coenzyme A pathway (Wood-Ljungdahl-pathway)

The reductive acetyl-CoA pathway is proposed to be one of the oldest metabolic pathways used to conserve energy and to fix carbon autotrophically [54]. Because this pathway was conserved in carboxydotrophic and acetogenic bacteria, methanogenic archaea, sulfate-reducing bacteria and archaea for 3.5 billion years before the great oxygenation event [55], most of the enzymes are oxygen sensitive. Therefore, all of these organisms live in the absence of dioxygen.

For instance, *Carboxydothermus hydrogenoformans* is the most extensively studied representative of the hydrogenogenic gram-negative bacteria that utilizes CO as carbon and energy source under anaerobic chemolithoautotrophic conditions [56]. It was first isolated from a hot swamp of Kunashir Island in 1991, and is able to grow under a 100% CO atmosphere in the gas phase. The optimal growth temperature is between 70-72 °C. It oxidizes CO to CO_2 under H_2 formation in equimolar quantities and uses H_2O as electron acceptor ($CO + H_2O \rightarrow CO_2 + H_2$) [57].

C. hydrogenoformans uses the reductive acetyl-CoA pathway, which consists of two branches, the methyl (Eastern) and carbonyl (Western) branch [58] (Fig. 2). In the methyl branch, one CO_2 molecule is reduced to formate by formate dehydrogenase and transferred to tetrahydrofolate (THF) as methyl carrier. While bacteria utilize THF as acceptor for the methyl group, archaea use tetrahydromethanopterin (H_4MPT) as a methyl acceptor. Stepwise multiple reductions of THF results in formation of (6S)-5-methyltetrahydrofolate that is used to transfer the methyl group through the methyl transferase (MeTr) to the corrinoid cofactor of the corrinoid iron-sulfur protein (CoFeSP) [59].

In the carbonyl branch, one CO_2 molecule is reduced by the carbon monoxide dehydrogenase (CODH) with two electrons to a CO molecule. Finally, the methyl group of CoFeSP and the CO molecule from

CODH are transferred to the active site of the acetyl-CoA synthase (ACS) and condensed with CoA to acetyl-CoA. This pathway is used in some bacteria and archaea in the reverse direction to degrade acetate to CO_2 and THF/H_4MPT bound methyl for example in *Archaeoglobus fulgidus* [60].

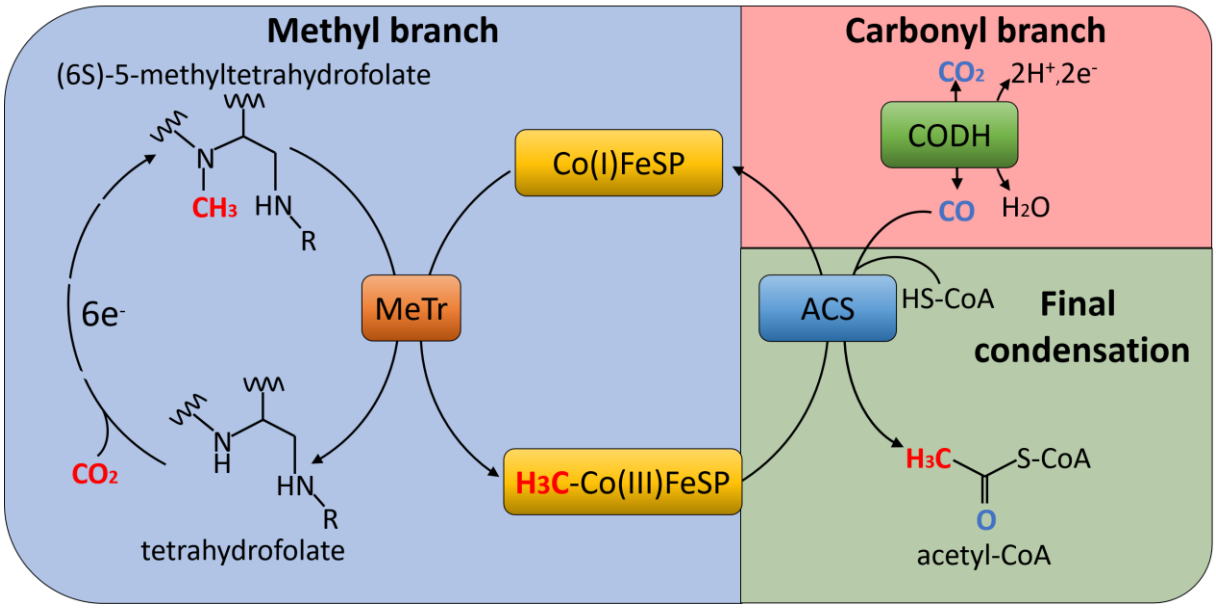

Figure 2: The reductive acetyl-CoA pathway in *C. hydrogenoformans*. The methyl group is carried by tetrahydrofolate (THF) to (6S)-5-methyltetrahydrofolate, trough to the methyltransferase (MeTr). Afterwards, the methyl group is further delivered to the corrinoid iron-sulfur protein (CoFeSP) and finally transferred to the active site of acetyl-CoA synthase (ACS). One CO_2 is reduced by the carbon monoxide dehydrogenase (CODH) to CO and delivered to ACS for the final conversion of the methyl group, CO and CoA to acetyl-CoA.

In the genome of *C. hydrogenoformans*, genes encoding for proteins for the final steps of the reductive acetyl-CoA pathway are located in one operon (Fig. 3). Although they are arranged in an operon in bacteria and archaea as well [55], the functional interaction of these enzymes is arranged in different compositions between the archaea and bacteria phyla. For instance, in methanogens and other archaea the key enzymes are arranged in one multienzyme complex of 2 MDa [61]. In contrast, in bacteria a bifunctional ACS/CODH complex of 310 kDa is arranged in a heterotetrametric complex e.g. in *Moorella thermoacetica* [62].

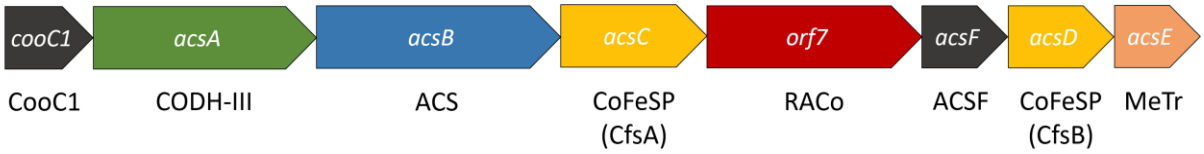

Figure 3: Gene cluster in *C. hydrogenoformans* encoding proteins for the reductive acetyl-CoA pathway. Genes encoding for proteins of the methyl branch are further downstream and not shown. The gene *cooC1* encodes a maturation protein for CODH and *acsF* encodes a maturase for ACS, in which both are responsible for nickel insertion [63-65]. *Orf7* is translated into the reductive activator of CoFeSP (RACo), which is responsible to reduce Co(II) of CoFeSP to Co(I) [66]. This figure is adapted and modified from Figure 1 of Jeoung et al. [67].

1.2.2 Acetyl-CoA synthase of *C. hydrogenoformans* (ACS_{Ch})

ACS from *C. hydrogenoformans* (ACS_{Ch}) has a calculated molecular weight of 82.2 kDa (732 amino acids) and is the central enzyme of the reductive acetyl-CoA pathway. It connects the carbonyl and methyl branch for the final condensation of CO, a methyl cation and CoA to acetyl-CoA according to Equation 2. It consists of three globular domains [62, 68], the N-terminal domain (residues 1 to 315), the middle domain (residues 316 to 500) and the C-terminal domain (residues 501 to 732) (Fig. 4A). The N-terminal domain exhibits a Rossmann-fold, while the other two domains contain α and β folds without any known structural motif. Only residues of the C-terminal domain coordinate the unique active site (cluster A) of ACS_{Ch}, which consists of a cubane-type [4Fe-4S] cluster, bridged to two nickel ions forming a [4Fe-4S]-(μ_2-SCys)-[Ni((μ_2-SCys)$_2$Gly)Ni] cluster (Fig. 4B) [40].

$$Co(III)FeSP-CH_3 + CO + CoA \rightarrow Co(I)FeSP + Acetyl-CoA \quad (2)$$

The distal nickel ion (Ni_d) is square planar coordinated by two sulfur atoms from cysteine residues and two nitrogen atoms from the protein backbone in a Cys-Gly-Cys motif. The second nickel ion is named proximal Ni (Ni_p) because of the proximity from the [4Fe-4S] cluster and has square planar coordination by three cysteine residues and a water ligand.

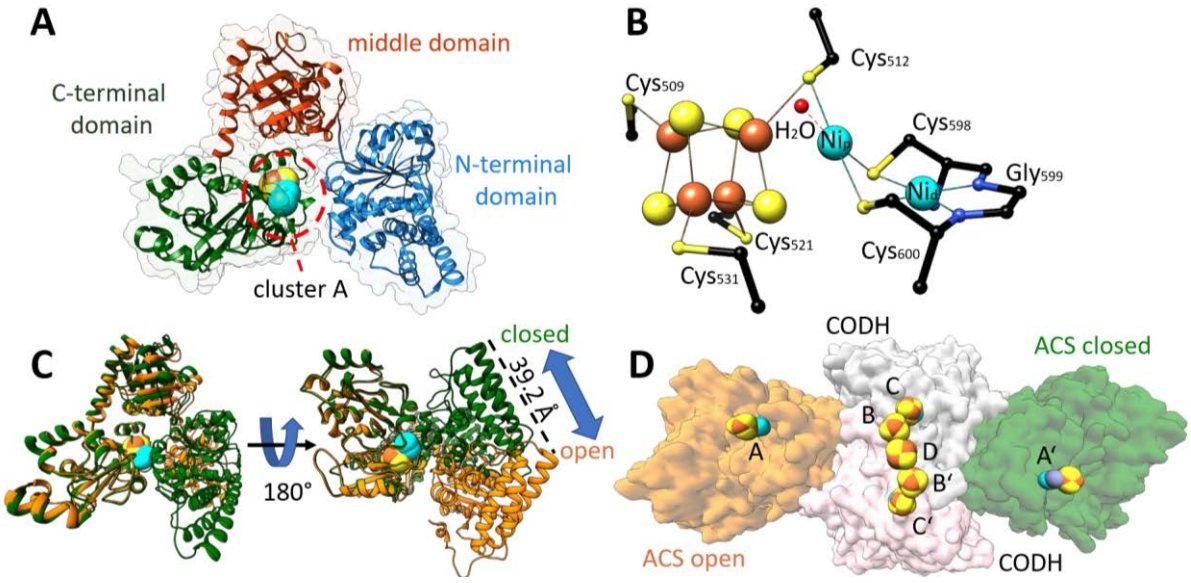

Figure 4: Structure of ACS and cluster A. A) Monomeric ACS_{Ch} from (PDB-ID: 1RU3 [40]) in the open conformation. The N-terminal domain is depicted in blue, the middle domain in orange and the C-terminal domain in green. The cluster A is depicted as spheres (Fe in orange, S in yellow and Ni in cyan). B) Cluster A of ACS_{Ch} (C in black, N in blue and O in red, other atoms has the same color code as in A). C) Superposition of the open and closed form of ACS of *M. thermoacetica* (ACS_{Mt}). The open conformation ($ACS_{Mt\text{-}open}$) is orange and the closed conformation ($ACS_{Mt\text{-}closed}$) dark green. D) Bifunctional ACS/CODH complex from *M. thermoacetica* (PDB-ID: 1OAO [62]). Subunits of CODH are depicted in grey and rose. ACS has the same color code as in C. Zn is shown as violet sphere. The cluster A of ACS_{Mt} and cluster B, C and D of CODH are depicted as spheres.

In *C. hydrogenoformans*, ACS exists as a monofunctional enzyme during growth under CO conditions [40], but it can also be isolated as a heterotetramer in complex with CODH [41]. In contrast to *M. thermoacetica*, a homoacetogenic bacteria, where ACS is always associated with CODH as the ACS/CODH bifunctional complex (Fig. 4D) [62]. In this complex, each CODH subunit is flanked by one ACS subunit and the active sites of each CODH subunit are connected *via* a tunnel to cluster A of ACS to guide CO to the active site [69]. Several crystal structures are available for the bifunctional complex (PDB-IDs: 1MJG [68], 1OAO [62], 2Z8Y [69], 3I04 [70], 6X5K [71], 6YTT [72]). The first crystal structure of the ACS/CODH (PDB-ID: 1MJG) was obtained from *M. thermoacetica*, in which the proximal position of cluster A (M_p) is occupied with a tetrahedral coordinated Cu [68]. However, another crystal structure from *M. thermoacetica* depicts the same complex with two different conformations of the ACS (ACS_{Mt}) subunits (Fig. 4C and D) [62]. One exhibits a conformation with both metal positions in the cluster A occupied by Ni ions, referred to the open conformation (ACS_{open}), because ACS is more solvent exposed compared to the previously known conformation of the Cu containing ACS. The other ACS subunit differs from the first ACS/CODH structure (PDB-ID: 1MJG) only in the composition of cluster A, where the proximal position is occupied with a tetrahedral coordinated Zn ion instead of a Cu ion. Because of the reduced solvent exposure is this conformation called the closed conformation (ACS_{closed}). The different solvent exposure is accomplished by a rearrangement of the domains, resulting through a relative repositioning of the N-terminal domain by 39.2 Å (Fig. 4C).

ACS is part of a 2 MDa ACDS complex in archaea whose structure is unknown. The ACDS complex is composed of five different subunits $(\alpha_2\varepsilon_2)_4\beta_8(\gamma\delta)_8$ [61]. The β–subunit is an ACS analogue of 53 kDa in size and lacks the N-terminal domain of the mono- and bifunctional ACS [73-75]. The CODH analogue is represented by the α and CoFeSP by the $\gamma\delta$ subunits. In addition to its different oligomeric state, the ACDS complex contains an additional archaea specific subunit (ε) which is proposed to bind FAD as electron donor for CO oxidation [76]. However, archaea lack a gene encoding for the methyl transferase (*acs*E) that is bacteria specific [55].

There was a long scientific discussion about the correct metal composition of cluster A. Some proposed a tetrahedral coordinated Cu ion as active state of ACS [68, 77], but later it was shown that Cu acts as an inactivator of the catalysis [40, 78-80]. Instead of the Cu-Ni, ACS requires a Ni-Ni centre to be fully active [40]. The inactive Zn and Cu forms of ACS are a result of metal impurities, which are caused by the labile property of the Ni_p and can be replaced by other divalent metals like Zn and Cu or removed by 1,10-phenanthroline [78, 81, 82]. Only Ni is capable to restore the activity of ACS [78].

Although different structures of ACS are available, there is no generally accepted mechanism for ACS catalysis at the cluster A. The only general agreements are that CoA binds as the last substrate in the catalytic reaction and that the oxidation state of the [4Fe-4S] cluster and the Ni_d remains in

the +2-oxidation state. The isolation of a methylated [83, 84] and acetylated [85] species of ACS which are electron paramagnetic resonance (EPR) silent are arguments for a Ni_p (II) state. Pulse-chase studies of ACS propose a random-sequential mechanism as shown in Figure 5 [86]. The redox state of the Ni_p during catalysis is discussed in the scientific community and the basis of two proposed main hypotheses of the ACS mechanism: The diamagnetic and paramagnetic mechanism [87, 88], where the Ni_p undergoes redox change during the catalysis.

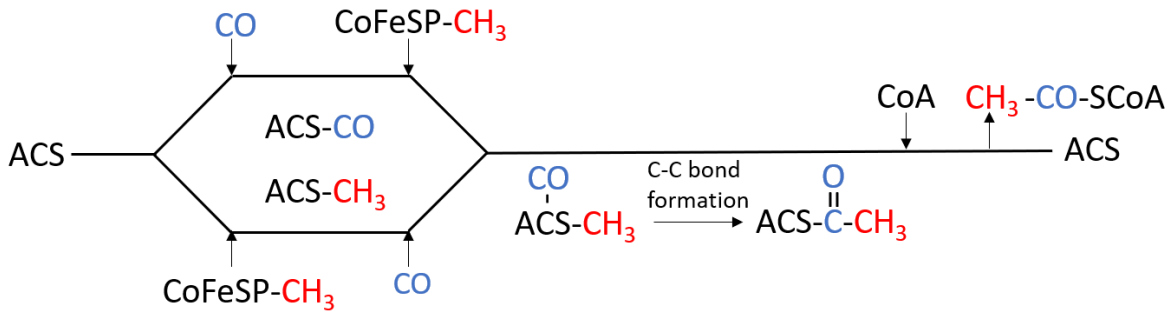

Figure 5: Proposed random sequential mechanism of ACS. The binding order of the methyl group or carbon monoxide is variable, only the CoA substrate binds in an ordered way as last.

Both mechanisms have in common that the oxidation state of the cluster A in the inactive state is as follows: $[4Fe\text{-}4S]^{2+}$-(Ni_p^{2+})-(Ni_d^{2+}) [89]. Despite being a random sequential description, both will be described in the order that CO binds first to the active site to simplify the mechanism. In the paramagnetic mechanism the binding of CO to Ni_p occurs with a simultaneously reduction of the Ni_p^{2+} to the Ni_p^{+} state [90]. This state can be tracked by infrared spectroscopy and EPR. The EPR signal for the Ni_p^{+} is called the NiFeC signal, which is the evidence that the Ni_p acts as CO binding site [73, 78, 91, 92]. The transmethylation occurs in a nucleophilic S_N2-type reaction [93-95] and results in a formation of CH_3-Ni_p^{3+}-CO state, which is expected to be highly oxidizing and unstable state and undergoes a rapid reduction to Ni_p^{2+} that is EPR inactive by an internal electron transfer whose mechanism is not known. Because of the rapid reduction, the Ni^{3+} state may have never been observed. The methylation is followed by the C-C bond formation to generate the acetyl species. A CoA-dependent thiolysis results in production of the final product and release of acetyl-CoA, which regenerates the active species (Fig. 6) [90].

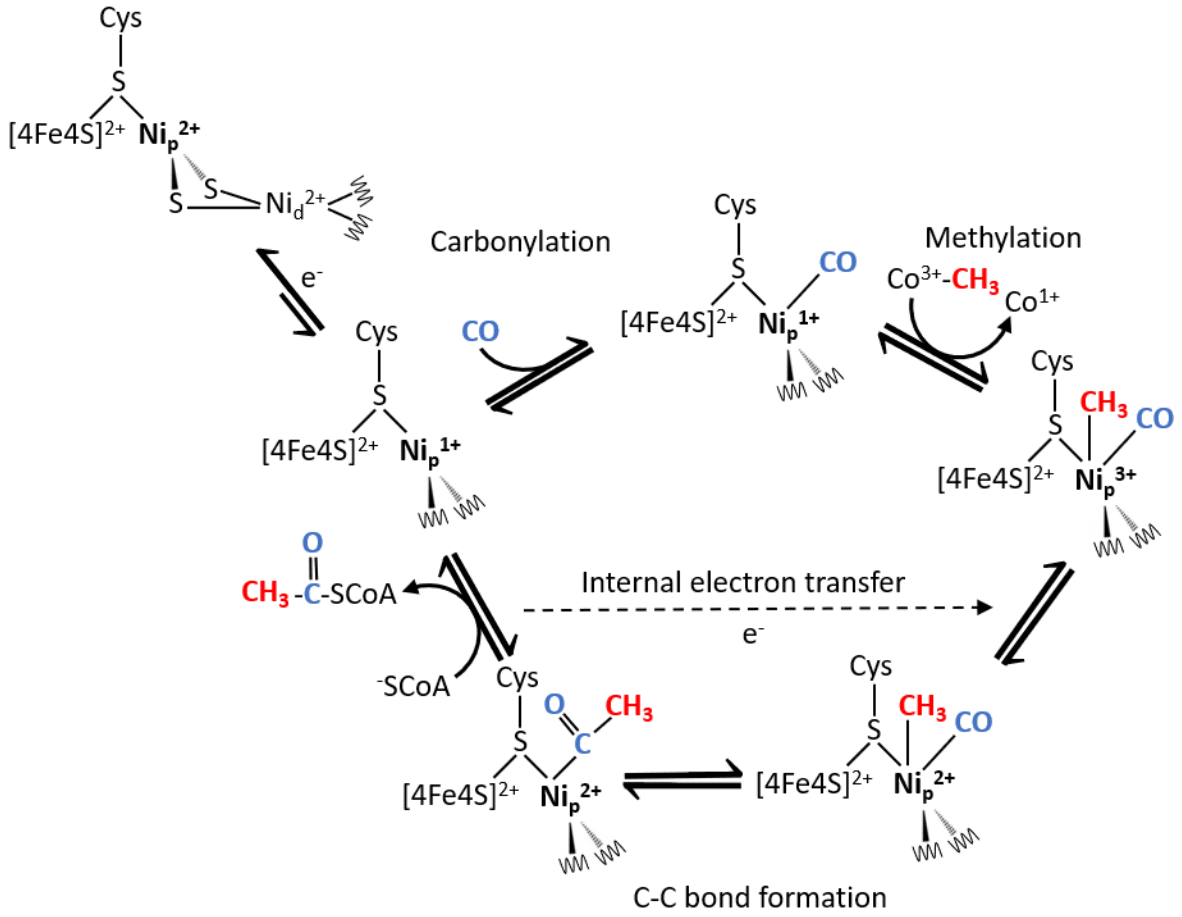

Figure 6: Paramagnetic mechanism. Although the mechanism is a random sequential mechanism, it is simplified as an ordered reaction, where CO binds first. See text for details. Figure adopted and modified from [90].

In contrast to the paramagnetic mechanism, every intermediate in the diamagnetic mechanism is EPR silent. The NiFeC species is described in this theory as an reversible CO inhibited state [96] and Ni_p cycles between the Ni_p^0 and Ni_p^{2+} state during catalysis. The reaction starts with a two-electron reduction of the Ni_p^{2+} to the Ni_p^0 state. Afterwards, one CO molecule binds to Ni_p and generates a Ni_p^0-CO species that is followed by a methyl transfer to generate a CH_3-(CO)-Ni_p^{2+} intermediate that undergoes the C-C bond formation. A subsequent attack of CoA results in the release of acetyl-CoA and regeneration of the Ni_p^0 state, which is ready for another catalytic cycle (Fig. 7).

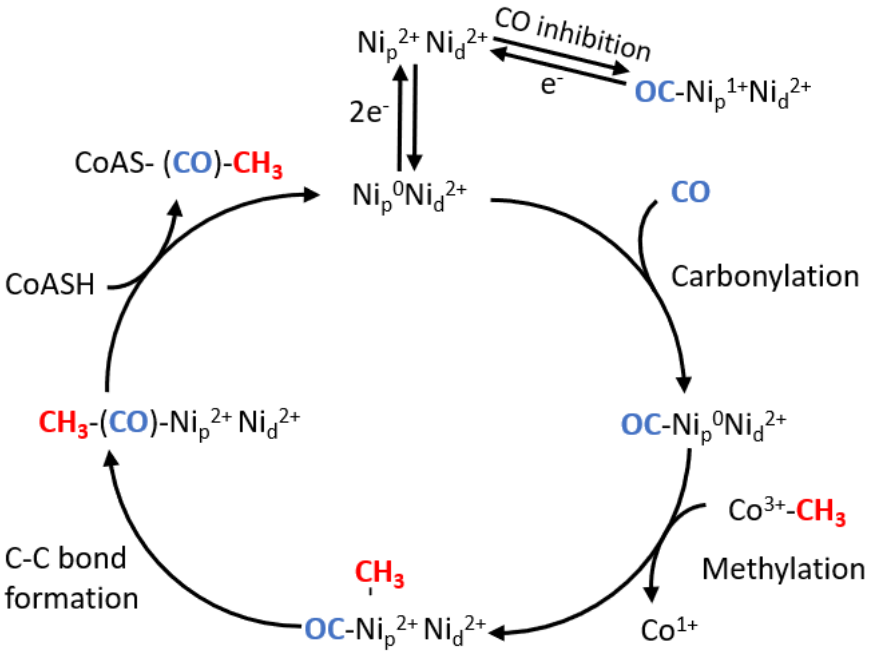

Figure 7: Diamagnetic mechanism. Although the mechanism is proposed as random sequential mechanism, it is simplified as ordered reaction, where CO binds first. See text for details. Figure adopted and modified from [97].

The ACS reaction is the biological equivalent of the industrially important Monsanto and Cativa processes. In these processes, expensive rhodium and iridium catalysts are used to synthesize acetic acid from methanol and carbon monoxide [98, 99]. In comparison, the metals used in the biological system are cheaper catalysts and more convenient for industrial processes, which is one reason why ACS is an important research subject in the biotechnological industry. However, the unclarified mechanism and its oxygen sensitivity are continuing to limit the ACS usage for industrial applications. Another challenge is the labile property of the Ni_p. Even though AcsF is known as the cluster A maturase, there are still open questions regarding the mechanism of the Ni insertion [63].

1.3 Research objective

ACS is the central enzyme of the reductive acetyl-CoA pathway and is responsible for the final reaction: the synthesis of acetyl-CoA. This reaction takes place at a unique metal cluster in ACS, catalyzing a process that is similar to the industrial Monsanto and Cativa processes, and ACS matches the requirement to be an attractive alternative catalyst for this reaction. As such, molecularly understanding of ACS mechanism is of high interest. Decades of research of ACS were carried out and provided the first insights into the protein structure and the metal cluster. Nevertheless, information regarding the reaction cycle itself is contradictory and much discussed in the scientific community.

There are large numbers of spectroscopic and biochemical data, but lacking structural data, especially, on enzyme-substrate complex, which could help us to understand the catalytic mechanism of ACS at the molecular level.

Therefore, the main objective of this thesis is to obtain new crystals structures of ACS, especially, with bound-substrate states in high-resolution to unambiguously identify a small ligand like CO. Such ligand-enzyme interaction is further confirmed by biochemical and biophysical methods, leading to a deeper understanding of the nature of the catalysis by ACS.

2 Materials and Methods

2.1 Anoxic work

The protein purification and crystallization were done under anoxic conditions in a glove box (model B, COY Laboratory) under a N_2/H_2 (95%/5%) atmosphere. The oxygen content inside the glove box was always below 10 ppm and monitored with the anaerobic monitor CAM 12 (Coy Laboratory). To remove oxygen from solutions, they were all degassed under vacuum and gas-flushed with nitrogen in a gas train with at least seven cycles and 18 min incubation for each step.

2.2 Metal free work

To avoid contamination by other divalent metals, especially Zn, all buffers and crystallization solutions were treated with 5% w/v Chelex 100 resin (Biorad) for one hour and afterwards removed by filtration. Additionally, all glassware was washed with 38% v/v HCl and subsequently rinsed with deionized water (*Milli-Q* H_2O).

2.3 Chemicals and materials

Unless otherwise noted, all chemicals were purchased from Fluka (Neu-Ulm), AppliChem (Darmstadt), Carl Roth (Karlsruhe), Merck (Darmstadt), Biorad (München) and Sigma-Aldrich (Deisenhofen) and had at least an analytical purity grade. The gases N_2 (99,99%) an N_2/H_2 (95%/5%) were ordered from Air Liquide (Berlin) and CO (99.9%) from Riessner Gase (Lichtenfels). All column materials for protein purification were from GE Healthcare.

2.3.1 Media and antibiotics

Media for cultivation of *E. coli* are shown in Table 3. Super optimal broth medium (SOB) media was purchased from Roth. All media were autoclaved for 20 min at 120 °C.

The antibiotics that were used for this work had the following concentration:

Carbenicillin (Cb), 50 µg/ml
Kanamycin (Km), 50 µg/ml
Tetracyclin (Tet), 100 µg/ml

Table 3: Composition of cultivation media.

Medium	Composition for 1 l
Lysogeny broth medium (LB)	10 g tryptone 5 g yeast extract 10 g NaCl
Terrific broth medium (TB)	12 g tryptone 24 g yeast extract 10 ml glycerol 10% phosphate buffer (0.17 M KH_2PO_4, 0.72 M K_2HPO_4)
Super optimal broth medium (SOB)	20 g tryptone 5 g yeast extract 0.96 g $MgCl_2$ 0.5 g NaCl 0.186 g KCl

2.3.2 Bacterial strains

The bacterial strain *E. Coli* M15 DZ291 [100] with the genotype (*F- Φ80ΔlacM15 thi lac- mtl- recA+*) was purchased from Qiagen and used for the cloning and expression of the gene *acsB*. The pREP4 plasmid in *E-coli* M15 carries a Km resistance and constantly expresses the lac repressor protein encoded by the *lac I*.

2.4 Genetic methods

2.4.1 Polymerase chain reaction (PCR)

PCRs were used to amplify DNA fragments from plasmids. The reaction mix and the thermo cycler setting are summarized in the following Table 4.

Table 4: PCR for cloning purposes. a) reaction mix. b) PCR thermo cycler program.

a)

Reagent	Volume [µl]
Forward primer (10 µM)	1
Reversed primer (10 µM)	1
Phusion Mastermix (2-fold)	25
Template (100-300 ng/µl)	1
milliQ-H_2O	ad 50

b)

Step	Temperature [°C]	Time [s]	Cycle number
Initial Denaturation	98	30	-
Denaturation	98	10	
Amplification	61	30	30
Elongation	72	30/kb	
Final Elongation	72	300	-
storage	4	-	-

Colony PCR

A successful transformation of *E. coli* was verified by colony PCR. Single colonies were picked from an LB-agar plate and resuspended in 20 µl *MilliQ*-H_2O. This suspension was used for PCR (Table 5).

In case of a positive clone, the leftover of the suspension was used to inoculate a 5 ml LB culture, containing the respective antibiotics.

Table 5: Colony PCR. a) reaction mix. b) PCR thermo cycler program.

a)

Reagent	Volume [µl]
Forward primer (10 µM)	0.5
Reversed primer (10 µM)	0.5
Taq Polymerase	0.5
Template (resuspended colony)	2
dNTPs (2 mM)	2.5
Reaction Buffer (10-fold) with Mg^{2+}	2.5
milliQ-H_2O	16.5

b)

Step	Temperature [°C]	Time [s]	Cycle number
Initial Denaturation	98	120	-
Denaturation	98	10	
Amplification	51	10	30
Elongation	72	60/kb	
Final Elongation	72	60/kb	-
storage	4	-	-

Site directed mutagenesis

Point mutations were introduced by using the QuickChange method [101]. The PCR product was cleaned with the GeneJET PCR Purification Kit (Thermo Scientific) and incubated with 10 u of DpnI for 1 h at 37 °C with the respective buffer. After the digestion of the template DNA, 5 µl of the reaction

mix was used for transformation of *E. coli* M15 pREP4. The PCR reaction mix and the thermo cycler settings are summarized in Table 6.

Table 6: Site directed mutagenesis (QuickChange method). a) reaction mix b) PCR thermo cycler program

Reagent	Volume [µl]
Forward primer (10 µM)	1
Reversed primer (10 µM)	1
Pfu DNA Polymerase	1
Plasmid (10-30 µg/µl)	1
dNTPs (2 mM)	5
10-fold Pfu-buffer with Mg^{2+}	5
milliQ-H_2O	36

b)

Step	Temperature [°C]	Time [s]	Cycle number
Initial Denaturation	95	30	-
Denaturation	95	30	
Amplification	55	45	18
Elongation	72	780	
Storage	4	-	-

2.4.2 Molecular cloning of *acsB*

Because the gene *acsB* encoding the ACS_{Ch} protein was already cloned into a pET28a vector (pET28a-twinst-ACS_{Ch}) [63] from the genomic DNA of *C. hydrogenoformans* [102], the gene was sub-cloned into a modified pQE30 vector (generated by B. Sc. Lena Swiatek, AG Dobbek, Humboldt Universität zu Berlin) without His-tag. Amplification of the gene was done by PCR using the Phusion DNA Polymerase. The pET28a-twinst-ACS_{Ch} was used as a template for the PCR reaction. Because the pet28a vector that contained the ACS_{Ch} gene was cloned with an N-terminal twinstrep-tag sequence including a tobacco etch virus (TEV) protease cleavage site for the purification, this sequence was amplified together with the ACS_{Ch} gene. The plasmid was kindly provided by Dr. Jae-Hun Jeoung (AG Dobbek, Humboldt Universität zu Berlin).

The PCR product was cleaned with a Nucleo Spin Gel and PCR Clean Up kit (Machery-Nagel). Furthermore, the cleaned PCR product and the cloning vector were both cleaved with the restriction Fast Digest enzymes *Bam*HI and *Pst*I for 30 min at 37 °C. An additional dephosphorylation step was taken with the vector by adding the Fast thermosensitive alkaline phosphatase (Fast AP, Thermo Scientific) enzyme to the reaction mix. After incubation, both samples were loaded on an agarose gel. The DNA fragments were isolated with the Gene JET Gel Extraction Kit (Thermo Scientific). The ligation step of the gene of ACS_{Ch} into the cloning vector was done with the T4-DNA-Ligase at 4 °C for 4 h in a

ratio of 3:1 (twinstrep-tag-ACS_{Ch} fragment to vector). All kits and enzymes were used according to the manufacturer's manual. All DNA samples were eluted from spin columns with *MilliQ*-H_2O.

Forward Primer of *acsB* (restriction site underlined):

5´-CTC ATC GGA TCC ATG GGC AGC AGC CAT C-3´

Reverse Primer of *acsB* (restriction site underlined):

5´-TAG TCC TGC AGT TAG AGT AGT GGC TCC ATG G-3´

A successful cleavage of the twinstrep-tag by using the TEV protease would form an N-terminal Gly-His brace, which could act as a possible metal binding site, such as Cu and Ni [103, 104]. To minimize the risk of an additional binding site, the histidine was mutated to an asparagine by using the QuickChange method (as described above in 2.4.1).

Forward primer *acsB* H45N:

5´-GAA AAC TTG TAT TTC CAG GGC AAT ATG AGC GAA G-3´

Reverse primer *acsB* H45N:

5´-CTT CGC TCA TAT TGC CCT GGA AAT ACA AGT TTT C-3´

2.4.3 Agarose gel electrophoresis

50x-fold Tris-acetate-ethylenediaminetetraacetic acid (EDTA) Buffer (TAE-Buffer): 242 g Tris, 57 ml glacial acetic acid, 100 ml 0.5 M EDTA, *ad* 1,000 ml H_2O

6-fold loading buffer: 0.25% (w/v) bromophenol blue / 0.25% (w/v) xylene cyanol / 30% (v/v) glycerol

The electrophoresis was performed using 0.8% (w/v) agarose gel in 1x TAE-buffer. To follow the migration of the DNA bands, 4 µl of Midori Green (Nippon Genetics Europe GmbH) was added to 60 ml of a gel. Each sample was mixed with 6x-fold loading dye. To estimate the size of the bands, one well was loaded with 3-5 µl DNA marker (Gene Ruler 1 kb DNA ladder, Fermentas). The electrophoresis was performed in an Owl^{Tm} D4 chamber at 100 V for 30 min.

2.4.4 Transformation

100 µl of chemical competent cells were thawed on ice and 1 µl plasmid (for plasmid maintenance/expression pre culture) or 10 µl of the ligation reaction mix were added. After 30 min

incubation on ice, the suspension was heat shocked for 45 s at 42 °C and again incubated on ice for 2 min. 1000 µl of prewarmed SOB medium was added and the cells were incubated at 37 °C and 140 rpm for 1 h. For a transformation of cells that were further used for expression, 50 µl of the cell suspension and in case of a transformation with a ligation product 90% and 10% of the cell suspension was transferred to different LB-Agar plates with the appropriate antibiotics and incubated over night at 37 °C.

2.4.5 Isolation of plasmid DNA:

Plasmid DNA was isolated from 5 ml bacterial culture grown in LB media with appropriate antibiotics using the Nucleo Spin Plasmid Easy Pure kit (Machery-Nagel). The culture was inoculated one day prior with a single colony from a LB-agar plate. The elution step was performed with 40 µl *MilliQ*-H_2O.

2.5 Biochemical methods

2.5.1 Expression of the gene encoding for ACS_{Ch}

For the expression of the gene encoding for ACS_{Ch}, competent *E. coli* M15 pREP4 cells were transformed with the plasmid construct containing *acsB* and the pISC plasmid [105]. One colony was used to inoculate into TB media containing the appropriate antibiotics. This culture was grown over night at 37 °C by 140 rpm. The culture flask was sealed with a butyl rubber septum to induce a transition from aerobic to anaerobic growth over time.

The next day, fresh TB medium was supplemented with 40 mM sodium fumarate, 0.5 mM cysteine, 0.1 mM $FeSO_4$, 1% glucose and the appropriate antibiotics. Afterwards, the flask was attached to a gas train and bubbled with nitrogen to generate an oxygen-free medium. After over pressurizing the overnight culture with nitrogen, both flasks were connected by a needle with two-way out through the septa and the pre-culture was released into the main culture by pressure difference to prevent oxygen contamination. The culture grew at 37 °C in a water bath under constant nitrogen flow. After the culture reached an optical density of 0.9-1.2 at 600 nm (OD_{600}), the culture was induced with 0.5 mM isopropyl β-D-1-thiogalactopyranoside (IPTG) and the temperature adjusted to 30 °C. Cells were harvested after 16 to 20 h by centrifugation at 6000 rpm for 20 min and the cell pellets frozen in liquid N_2 and stored at -80°C until use.

2.5.2 Purification of ACS_{Ch}

Frozen cells were resuspended in 5 ml buffer A (50 mM Tris/HCl pH 8.0, 100 mM NaCl, 2 mM TCEP) per gram of cells, supplemented with a small amount of DNase A, lysozyme and avidin and stirred for 1 h. The suspended cells were lysed in a rosette cell on ice by sonification (Bandelin Sonoplus HD 2070) with a KE 76 sonotrode three times for 5 min (amplitude 50%, 5 cycles). The cell lysate was centrifuged at 30,000 rpm for 45 min at 12 °C. The supernatant was loaded on a strep-tactin column, washed with buffer A containing 1 mM sodium dithionite (DT) and equilibrated with buffer A. After loading the supernatant, the column was washed with 10 column volume (CV) of buffer A. Elution was performed with 2.5 mM desthiobiotin in the same buffer. To remove the twinstrep-tag of ACS_{Ch}, the eluted protein solution was incubated with strep-tagged TEV protease in a ratio of 1:100 for 16 h and supplemented with β–mercaptoethanol to a final concentration of 10 mM.

Subsequently, the protein solution was applied to a Q-Sepharose anionic exchanger column. The column had been equilibrated before with buffer B (50 mM Tris/HCl pH 8.0, 10 mM NaCl). After the protein solution was loaded on the Q-Sepharose column, the column was washed with a mixture of 70% buffer B and 30% buffer C (50 mM Tris/HCl pH8, 500 mM NaCl) for at least 10 CV. The elution was performed with 100% buffer C. To remove uncut ACS_{Ch} from the elution fraction, a strep-tactin column was tentatively attached after the Q-Sepharose column during elution. The eluted protein fraction was reconstituted with $NiCl_2$. Reconstitution was performed by adding a 6-fold excess of $NiCl_2$ to the protein solution and incubation for 60-72 h at 45 °C. The solution was also supplemented with β-mercaptoethanol to a final concentration of 10 mM. Reconstituted ACS_{Ch} was subsequently loaded on a sephadex S200 pre-grade column (16 mm x 600 mm) for size exclusion chromatography (SEC) using buffer A without TCEP. Fractions that correspond to monomeric ACS_{Ch} were collected, concentrated, frozen and stored in liquid N_2.

2.5.3 Sodium dodecyl sulfate polyacrylamide gel electrophoresis (SDS-PAGE)

Separating-gel: 12% (w/v) acrylamide/bis-acrylamide (29:1)
375 mM Tris-HCl pH 8.8
0.1% (w/v) Sodiumdodecylsulfate (SDS)
0.08% (v/v) N,N,N´,N´-tetramethylethylendiamin (TEMED)
0.05% (w/v) Ammonium persulfate (APS)

Stacking-gel: 6% (w/v) acrylamide/bis-acrylamide (29:1)
125 mM Tris/HCl (pH 6.8)
0.1 (w/v) SDS
0.08% (v/v) TEMED
0.05% (w/v) APS

To observe the expression of ACS_{Ch} and to qualitatively analyze the individual steps of the purification procedure, the discontinuous sodium dodecyl sulfate polyacrylamide gel electrophoresis (SDS-PAGE) as described by Laemmli was used [106]. All SDS-PAGE samples were mixed with the appropriate amount of 5 x SDS buffer containing 5% β-mercaptoethanol and cooked for 5 min in a waterbath. After centrifugation of the samples at 10,000 rpm for 1 min, the samples were loaded on a 12% SDS gel to separate the proteins. The electrophoresis was performed in a Mighty Small Deluxe chamber (Serva) for 1 h at 175 mV. The PageRuler prestained marker (Thermo Scientific) was used to identify the size of the protein band.

2.5.4 UV/vis spectroscopy

UV-visible absorption spectra were recorded with an Agilent8453 spectrophotometer with photodiode array at 25°C using a Peltier temperature controller. The measurement was performed in a black-walled quartz cuvette with 1 cm pathlength.

2.5.5 Synthesis of methylcobinamide

The synthesis of methylcob(III)inamide (MeCbd) from methylcobalamin (MeCbl) was done according to the method described by Brown [107]. For synthesis, 50 mg of MeCbl was dried over P_2O_5 over 72 h and dissolved in 600 µl CF_3SO_3H and stirred for an additional 24 h. The reaction mix was poured into 100 ml of 1 M K_2HPO_4 and loaded on a column for purification. In contrast to the protocol, the purification was done with a Sep Pak C18 reversed phase column (Water Sep Vak 6cc) and the washing step was performed with 10% acetonitrile in water. After the elution step with 50% aqueous acetonitrile, the collected fraction was dried in an exicator over days until the solvent was completely evaporated. The remaining MeCbd was dissolved in *MilliQ*-H_2O and stored at -80 °C. All steps were performed in dim light.

2.5.6 Determination of the iron content of ACS_{Ch}

The iron determination of ACS_{Ch} was done by the method described by Buchanan [108]. 7.5 µl of a 25% (v/v) HCl solution was added to a protein sample of 250 µl, containing 350 µg ACS_{Ch}, and incubated at 80 °C for 10 min. After centrifugation for 10 min at 10,000g, the supernatant was mixed with 750 µl *MilliQ*-H_2O, 50 µl 10% (w/v) hydroxylamine and 250 µl of 0.1% (w/v) phenanthroline. The reaction mix

was incubated for 30 min at room temperature and the absorption of the sample measured at 512 nm. To calculate the amount of iron from the absorption value, a standard was prepared using iron ammonium sulfate ranging from 0-20 nmol.

2.5.7 Determination of protein concentration

Protein concentration for calculating amount of ACS_{Ch} for proper use of TEV protease and amount of $NiCl_2$ for reconstitution was performed by Bradford method [109]. Bovine serum albumin (BSA) was used to generate a standard curve. The protein concentration of the final purification product of ACS_{Ch} was performed by UV/vis spectroscopy. ACS_{Ch} was denatured with 6 M guanidinium chloride, 50 mM Tris/HCl pH 1 and the absorption measured at 280 nm and the concentration calculated with the theoretically extinction value of ACS_{Ch} ($\varepsilon_{280\,nm}$ = 92,710 $M^{-1}\,cm^{-1}$) according to ProtParam [110].

2.5.8 Measurement of ACS_{Ch} activity (acetyl-CoA formation)

The activity of ACS_{Ch} was determined based on a method described by Grahame [111, 112]. Formation of acetyl-CoA from CoA, MeCbd and CO was followed by the conversion of methylcob(III)inamide (MeCbd) to cob(I)inamide (Cbd). The conversion was observed by measuring the spectral changes at 387 nm (increase) and 462 nm (decrease). A typical reaction mix contained 2 µM ACS_{Ch} in 100 mM HEPES pH 7.2, 300 µM freshly prepared Ti(III)citrate, 50 µM MeCbd, 10% (v/v) CO saturated 100 mM HEPES pH 7.2 and 200 µM CoA in a screw caped cuvette with silicon septum. After mixing all components except the CO saturated buffer and CoA, the cap was closed and the CO saturated buffer added with a gastight syringe. This reaction mix was incubated for 5 min at room temperature and the reaction was started by adding CoA to the cuvette. The experiment was performed in dim light. Finally, the reaction rates were calculated using the difference extinction coefficients from MeCbd and Cbd at 387 nm ($\Delta\varepsilon_{387\,nm\,(MeCbd\text{-}Cbd)}$ = -17410 $M^{-1}\,cm^{-1}$) [113].

2.5.9 Isothermal titration calorimetry (ITC)

All ITC measurements were performed with a MicroCal VP-ITC system in a glovebox (LABstar pro, MBraun) under anoxic conditions by nitrogen circulation at 25 °C in 50 mM Tris/HCl buffer pH 8, 100 mM NaCl and all solutions were degassed immediately right before the titration except for CO gassed solutions. For the CoA binding, ACS_{Ch} was present in the 1.4 ml reaction cell with a

concentration of 20 µM and stepwise injected with Coenzyme A (800 µM). The CoA concentration was determined by using the extinction coefficient ($\varepsilon_{259\ nm}$ = 16.8 $mM^{-1}cm^{-1}$) [114].

For the CO binding experiment, 40 µM ACS_{Ch} with 1 mM Ti(III)citrate was present in the reaction cell and CO gassed buffer (920-930 µM) was injected. After filling the injection syringe, remaining CO gassed buffer was added to a 1 mM DT containing hemoglobin solution in a gastight cuvette to measure CO concentration. The absorption difference at 431 nm before and after adding the CO gassed buffer was used to calculate the amount of carboxyhemoglobin with the extinction coefficient ($\Delta\varepsilon_{431}$ = 61.9 $mM^{-1}cm^{-1}$). This extinction coefficient was calculated from the extinction coefficient for reduced hemoglobin (ε_{431} = 140 $mM^{-1}\ cm^{-1}$) [115] and the measured extinction coefficient for carboxyhemoglobin (ε_{431} = 78.05 $mM^{-1}cm^{-1}$).

The interval between the injections was 300 s in all experiments and the reaction cell stirred with 307 rpm. Baseline calculations were performed using NITPIC [116] and the data were further analyzed and fitted using a one-binding site model with Origin 7.0 software [117]. The experimental data of the CO-titration showed an apparent deviation using all data points (Chi^2 = 1.1 * 10^4) and were fitted without the first three data points (Chi^2 = 5.4 x 10^3).

2.6 Protein crystallization

Protein crystallization experiments were performed with the sitting drop vapor diffusion technique at 18 °C. The drops were dispensed with the OryxNano crystallization robot (Douglas Instruments) in 96-well plates. The drop size was in the range of 1-1.4 µl with a 1:1 ratio of protein and reservoir solution for screening. Crystals were cryoprotected by soaking the crystals with reservoir solution containing 15% 2,3-R,R-butandiol and flash frozen in liquid nitrogen. All crystallization drops contained 16.5 mg/ml ACS_{Ch} in 50 mM Tris/HCl pH 8 and 100 mM NaCl before mixing with the respective reservoir solution. The different crystallization conditions are summarized in Table 7.

Table 7: Composition of crystallization conditions for crystallization of ACS_{Ch}.

Crystal	Buffer	Salt	Precipitant	Additive
$ACS_{Ch\text{-}closed}$:Ni	-	0.1 M Lithium nitrate tribasic tetrahydrate	16% w/v PEG 3350	5 mM Ti(III)citrate
$ACS_{Ch\text{-}closed}$:Zn	70 mM Bis-Tris-Propane pH 7.6	30 mM Citric acid	24% w/v PEG 3350	5 mM Ti(III)citrate
$ACS_{Ch\text{-}closed}$:Ni-CO	-	0.1 M Sodium malonate pH 6	20% w/v PEG 3350	5 mM Ti(III)citrate
$ACS_{Ch\text{-}open}$:Ni-CoA	150 mM MES pH 6.0	2 M Ammonium sulfate	5% v/v PEG 300	5 mM CoA trilithium salt

2.7 Data collection and processing

Diffraction images were recorded at the synchrotron radiation source BESSY II (Helmholtz Zentrum Berlin) [118]. The diffraction data were collected at 100 K at the beamlines of 14.1 and 14.2. All measurements were performed at a wavelength of 0.9184 Å, unless otherwise noted. An optimal data collection strategy was chosen by using the program iMOSFLM [119]. Data processing and scaling was performed using XDSAPP GUI [120] that uses XDS [121, 122] and the STARANISO server [123]. To analyze the metal content in a crystal, an X-ray fluorescent (XRF) spectra of the sample was recorded and analyzed by XFEPlot [124]. For recording anomalous scattering data, an energy scan for the respective metal was recorded and the corresponding energy was adjusted.

2.8 Structure determination and refinements

Molecular structures were determined using PHENIX [125]. The ACS_{Ch} structures were solved by using molecular replacement and the model of the monomeric ACS from *C. hydrogenoformans* (PDB-ID:1RU3 [40]). To build the whole model for $ACS_{Ch\text{-}closed}$ crystals of the space group $P2_12_12_1$, each of the three domains of ACS_{Ch} were searched as an individual model without the linker region between the domains in PHASER [126] to build a first new model. These solutions were afterwards combined and the domains connected in COOT [127] to build a second model with the complete monomeric ACS_{Ch}, which was further refined by using PHENIX refine [128] and COOT [127]. This model was used for molecular replacement of new datasets afterwards.

2.9 Graphic representation

Depiction of model structures were done with the program UCSF Chimera [129]. The sigma level of different maps that were compared were contoured according to the sigma comparison tool [130].

3 Results

3.1 Expression and purification of ACS_{Ch}

The ACS_{Ch} gene was cloned into the pQE30 derived vector, which contains an N-terminal twinstrep-tag with a TEV protease cutting site to improve the purification. ACS_{Ch} was expressed as described in the material and methods section (2.5.1). As shown in Figure 8, ACS_{Ch} is already overexpressed after two hours of induction. However, cells were harvested after 16-20 h for more biomass. The yield of wet paste cells was around 6-8 g of cells per liter of TB medium. This is a 3-4-fold increase compared to the previously used system in *E. coli* BL21(DE3) with a pET28a expression vector, which gave yields of only 2 g wet cell paste per liter of TB media [131]. Not only did the cell mass increase with the pQE30 expression system, the expression band of ACS_{Ch} became also more prominent compared to the *E. coli* housekeeping proteins (Fig. 8).

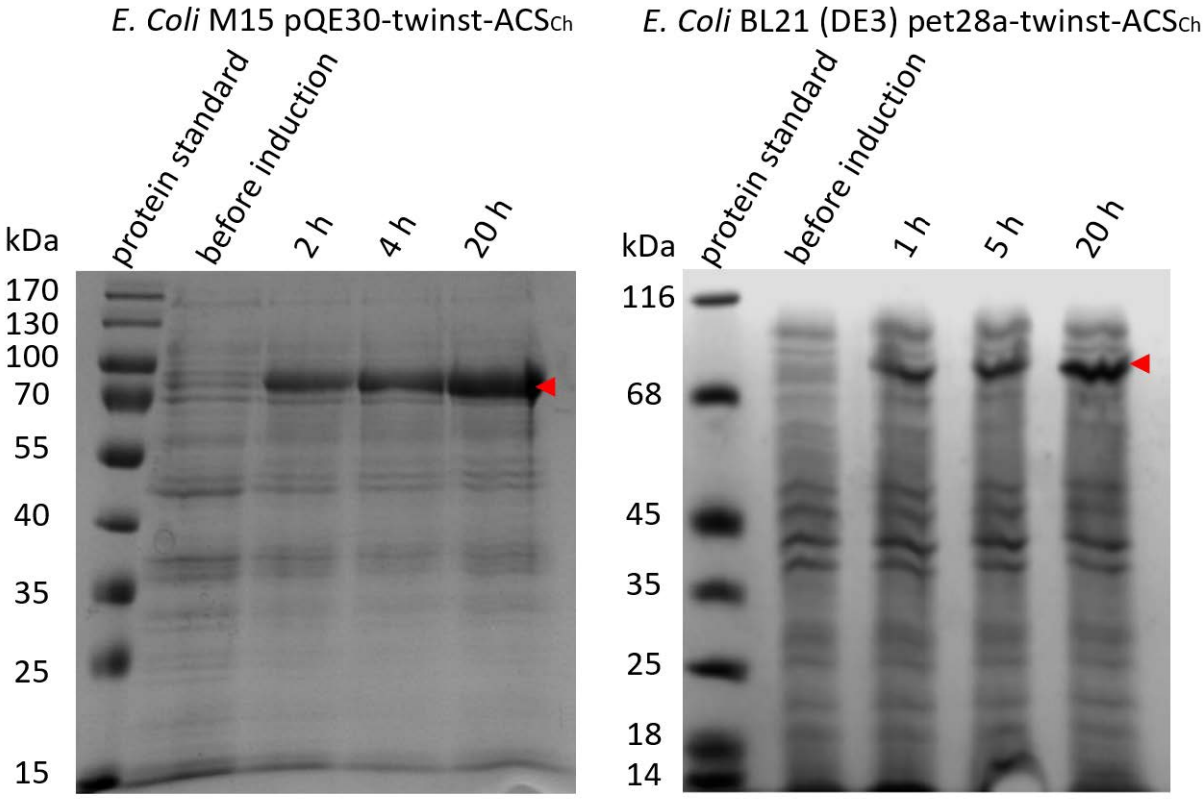

Figure 8: Comparison of heterologous expression of ACS_{Ch} with different vectors. The 12% (w/v) SDS-Gels shows samples before and after induction with IPTG. All samples were normalized to an OD_{600} of 0.5. The expected size of ACS_{Ch} is 82.2 kDa (red arrow). The left gel shows the expression after 2h, 4 h and 20 h after induction in *E. coli* M15 with the modified pQE30 vector. A strong corresponding band is already detectable after 2 h induction. The right gel shows the previously used expression protocol in *E. coli* BL21 (DE3) with a pET28a vector after 1 h, 5 h and 20 h after induction [128]. There is also an overexpression of ACS_{Ch} detectable after 1 h after induction.

ACS_{Ch} was purified in three chromatographic steps: an affinity chromatography using the twinstrep-tag, anionic exchange chromatography with Q-sepharose to remove a main impurity by using a gradient and a size exclusion chromatography (SEC) to isolate different oligomeric states and excess of Ni after reconstitution as a polishing step (Fig. 9A and B). Only monomeric ACS_{Ch} was collected from the SEC and used for all further experiments. ACS_{Ch} was concentrated to 20-25 mg/ml before freezing. The progress of purification is shown in Figure 9B. The cells of one 5 l culture were used for a standard purification, which results in a yield of 40-60 mg of ACS_{Ch}. This corresponds to 1.5-2 mg ACS_{Ch} per g of cells.

To exclude interferences of the twinstrep-tag for the activity and crystallization behavior of ACS_{Ch}, the tag was removed by the TEV protease after the first step of purification, as the proximal metal site (M_p) at cluster A is very labile and can be easily replaced by other metals (especially zinc) which would result in the production of inactive ACS [78]. Therefore, ACS_{Ch} was chemically reconstituted with $NiCl_2$ immediately after the anion column and the excess nickel was removed by SEC. Iron of as-reconstituted ACS_{Ch} was always present in a 4-fold higher molar concentration than mol of ACS_{Ch} protein matching the presence of [4Fe-4S] cluster per ACS molecule.

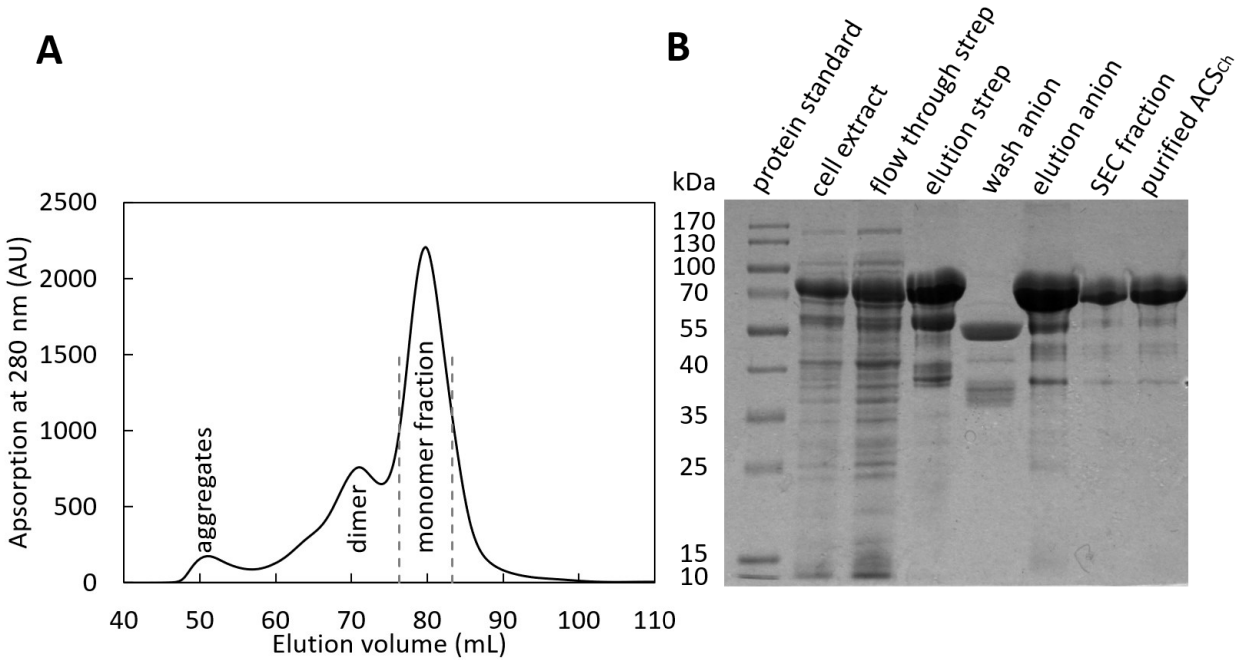

Figure 9: ACS_{Ch} purification. A) Size exclusion chromatography of reconstituted ACS_{Ch}. Monomeric ACS_{Ch} elutes after 76 ml, was collected and concentrated. B) 12% (w/v) SDS-PAGE gel shows enrichment and increase of purity of ACS_{Ch} by purification steps.

3.2 UV/vis spectroscopy of ACS_{Ch}

The UV/vis absorption spectra of ACS_{Ch} before and after reconstitution are shown in Figure 10. Both show the typical protein maxima at 280 nm followed by a broad shoulder at 410 nm, a characteristic feature for proteins containing an oxidized [4Fe-4S] cluster [132]. After reconstitution, ACS_{Ch} shows an additional shoulder at 340 nm, whereas the untreated sample has a small shoulder at around 320 nm. This spectral change is most likely associated with the occupation of the cluster A with nickel. A spectral change during nickel titration was also reported for the homolog ACS from *Methanosarcina thermophila*, which showed one sharp maxima from 330-340 nm and a small broad maximum in the range from 400-700 nm after calculating a difference spectrum by Ni-reconstituted minus Ni-free samples [78]. These changes can be explained due to ligand-to-metal charge transfer from the nickel binding to S-Cys ligands. This result was also found for ACS_{Ch} with a sharp maximum at 334 nm and two broad maxima 400-500 nm and 500-660 nm in the difference spectra of ACS_{Ch} before and after reconstitution.

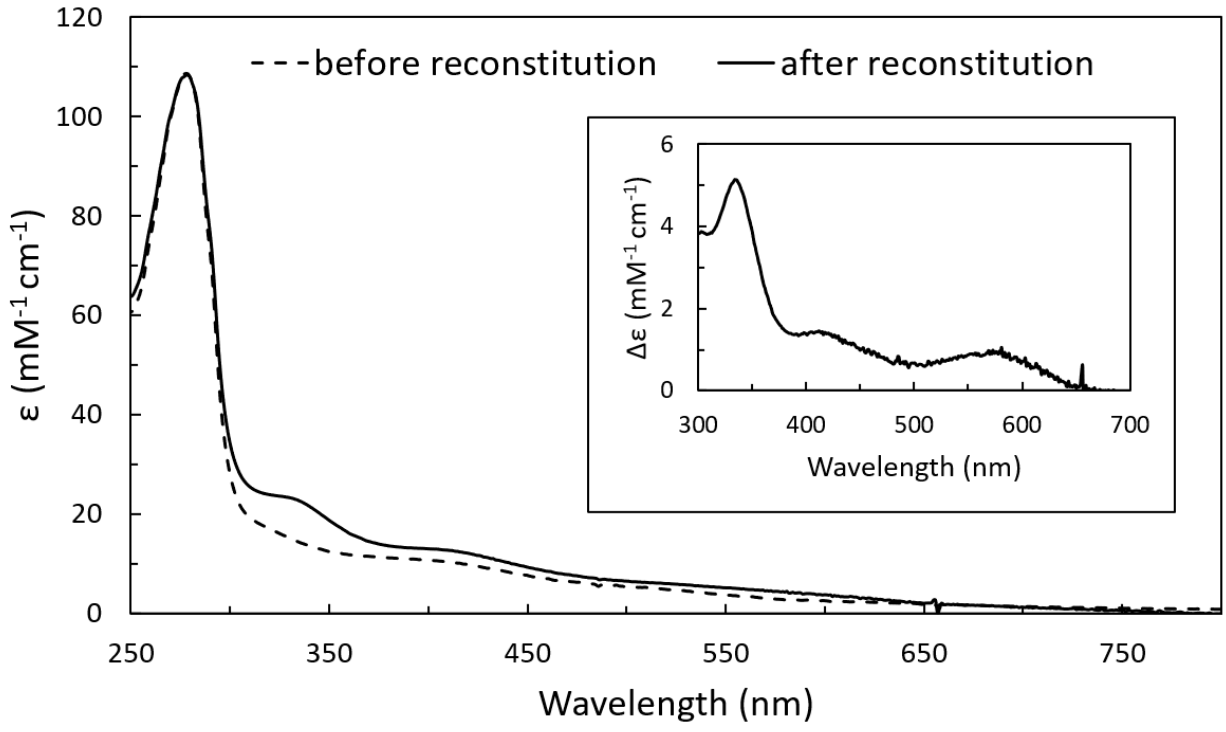

Figure 10: UV/vis spectra of ACS_{Ch}. Before reconstitution in dashed and after reconstitution in solid lines. The small shoulder at 410 nm corresponds to the [4Fe-4S] cluster. After reconstitution an additional shoulder is visible at 340 nm. In contrast, the untreated sample shows only a small shoulder at around 320 nm. The inset shows the difference spectrum of reconstituted ACS_{Ch} minus non-reconstituted ACS_{Ch}.

3.3 Activity of ACS_{Ch}

The activity of ACS_{Ch} was measured to verify an intact and active cluster A. This was done according to Grahame et al. [111, 112]. In this assay methylcob(III)inamide (MeCbd) is used as methyl group donor. MeCbd was chosen because of the base-off coordination of the methyl group, which is also present in the natural methyl group donor CoFeSP [133] and is more reactive compared to the base-on coordination as, for instance, in methylcobalamin (MeCbl) [134]. The reaction can be followed by the conversion of CH_3-Co(III)binamide to Co(I)binamide (Cbd), which results in a spectral change at 387 nm (increase) and 462 nm (decrease). Figure 11 shows the spectral changes after adding CoA to the reaction mixture over the time course.

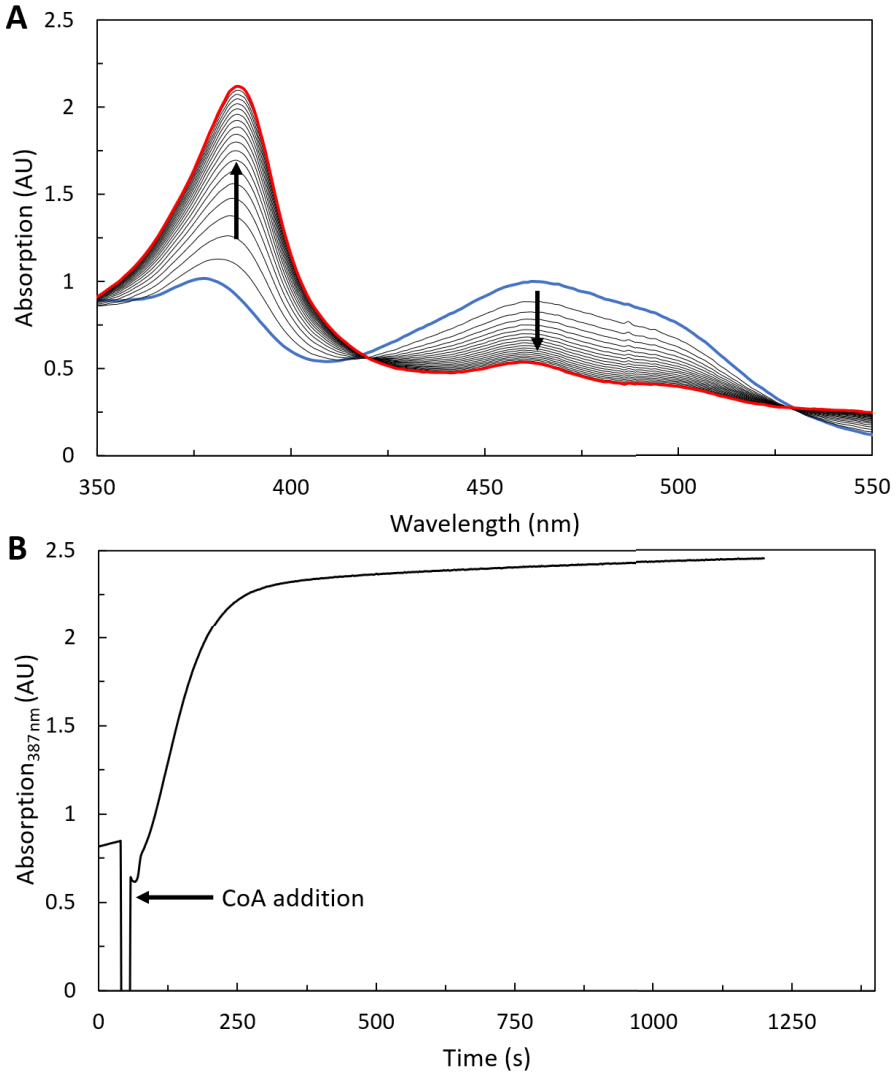

Figure 11: Activity assay of ACS_{Ch}. A) Start spectra is indicated as blue and last spectra as red line. B) Time course of the absorbance at 387 nm. The reaction mix contained 10% (v/v) CO-saturated 100 mM HEPES buffer pH 7.2, 300 µM Ti(III)citrate, 50 µM MeCbd, 2 µM ACS_{Ch} and 200 µM CoA in 100 mM HEPES pH 7.2 buffer at room temperature. The reaction was started with CoA and spectra recorded over 1200 s.

Following the increase of the absorption at 387 nm and by using the difference extinction coefficient of MeCbd and Cbd ($\Delta\varepsilon_{387\ nm\ (MeCbd\text{-}Cbd)}$ = 17.41 $mM^{-1}\ cm^{-1}$ [113]), a specific activity of 0.075 $\frac{\mu mol}{\min * mg_{ACSCh}}$ (turnover number of 6.2 min^{-1}) was calculated. These values are in the same range as reported for the isolated ACS from *M. thermophila* with a turnover rate of 4.61 min^{-1} [111].

3.4 Structural and biochemical analysis of $ACS_{Ch\text{-}closed}$

3.4.1 Crystallization of $ACS_{Ch\text{-}closed}$ and structure determination

ACS_{Ch} crystals appeared in several conditions of the PEG-ION Screen (Hampton) containing reagents with carboxylic groups as citrate, malonate, acetate or tartrate. Crystal color ranged from light brown to dark brown and had a longish hexagonal morphology (Fig. 12). The most promising crystallization conditions according to the diffraction of the crystals were optimized. The conditions contained citrate and malonate. In addition, adding Ti(III)citrate as additive to the crystallization conditions increased the diffraction quality of the crystals resulting in crystals which diffracted to 1.8-2.1 Å as shown in Figure 12. The crystals belong to the orthorhombic space group $P2_12_12_1$ with a cell constant of a = 70.0 Å, b = 99.8 Å, c = 238.5 Å and $\alpha = \beta = \gamma = 90°$, which differs from the known unit cell of the monofunctional $ACS_{Ch\text{-}open}$ (PDB-ID: 1RU3, a = b = 200.3 Å, c = 169.4 Å, $\alpha = \beta = 90°$, $\gamma = 120°$) with the space group of $H3_2$ and crystal packing. Solving the structure by molecular replacement with the PDB model of 1RU3 led to no results, but searching for each of the three domains (N-terminal, C-terminal and middle domain) separately without the flexible linker region between the domains led to a solution. These solutions were combined in one PDB and the missing amino acids between the domains filled into the remaining electron density map ($2F_o\text{-}F_c$) yielding a new model with two ACS_{Ch} molecules in the asymmetric unit. Both ACS_{Ch} molecules are in the same conformational state and are superimposable with an rmsd of 0.6 Å for Cα atoms. One of the molecules is shown in Figure 13A. This new crystallized conformation of ACS_{Ch} is called $ACS_{Ch\text{-}closed}$.

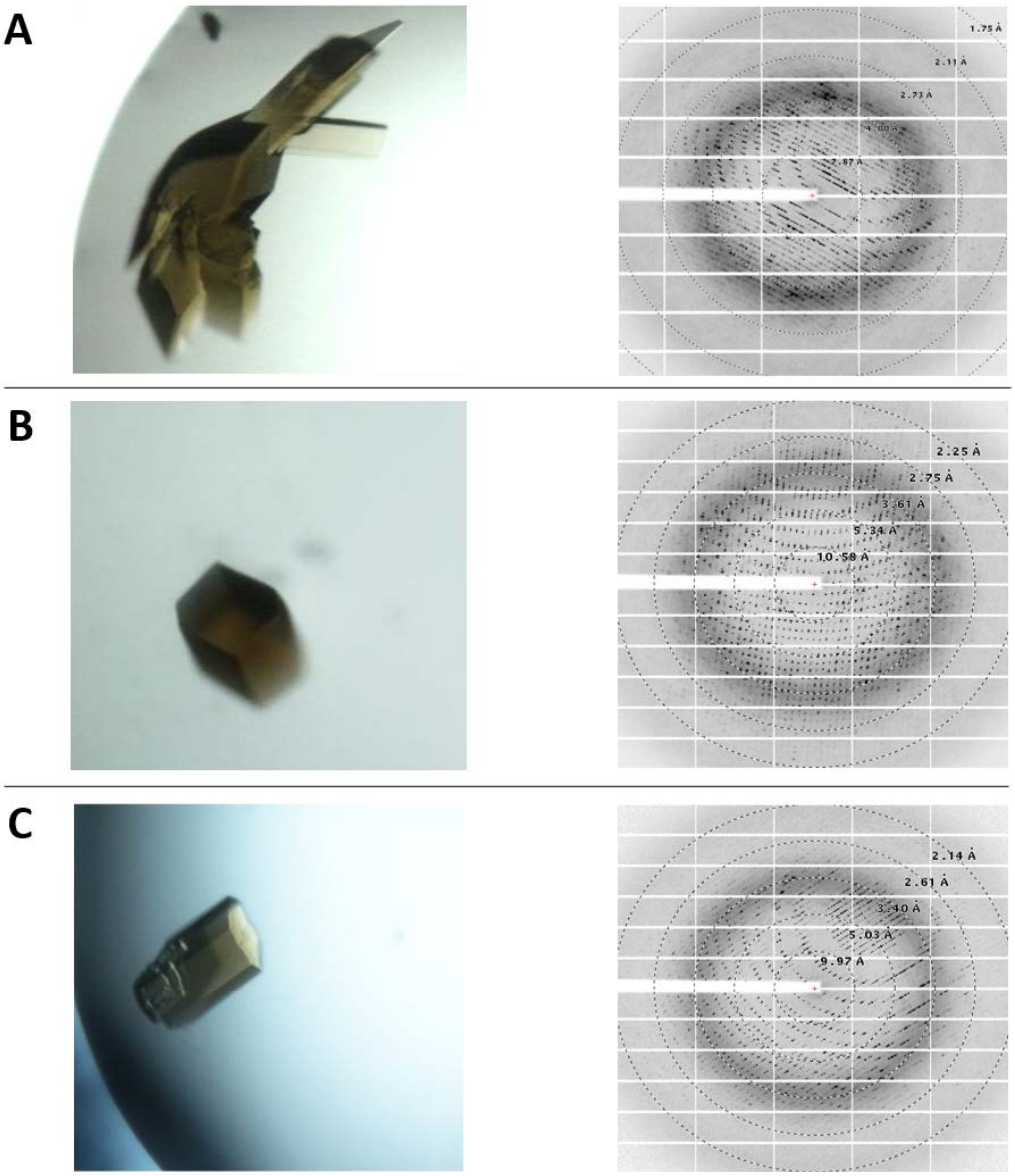

Figure 12: Representative crystals (left panel) and diffraction (right panel) of $ACS_{Ch\text{-}closed}$ crystals. All crystallization conditions started with 8.3 mg/ml ACS_{Ch}. A) Formulation: 0.1 M Lithium nitrate tribasic tetrahydrate, 16% w/v PEG 3350 B) Formulation: 30 mM citric acid, 70 mM Bis-Tris-Propane pH7.6, 24% w/v PEG 3350 C) Formulation: 0.1 M sodium malonate pH 6, 20% w/v PEG 3350.

3.4.2 $ACS_{Ch\text{-}closed}$ structure and metal identification of cluster A

Since the M_p site of the cluster A is very labile, X-ray fluorescence (XRF) spectra of all crystals were measured to identify possible contaminations by Cu or Zn, which might have been introduced during purification or from crystallization chemicals (Fig. S1A). The spectra indicate Ti, Fe, Ni and Zn as the most abundant metals in the sample. Fe and Ni are part of the cluster A and Ti is present in Ti(III)citrate used as the crystallization additive. Cu was never detected and high Zn signals have been present in crystals, which were grown in high citrate conditions and have been crystallized from manufacturer

stock solutions (1 M BTP, 1 M Citric acid, Fig. 12B). The anomalous scattering contribution of these crystals at the Ni high energy edge (8.33 keV) showed only the distal metal (M_d) site occupied with a nickel ion and additional data collection at the Zn high energy edge (9.66 keV) confirmed a Zn ion at the M_p position of cluster A (Fig. 13C and D). Crystals which were grown with self-prepared metal free solutions showed minor Zn level in the XRF spectra (Fig. S1B and C) and data collection at the high Ni-K-edge confirmed nickel ions at the M_p and M_d site of the cluster A (Fig. 13B). The presence of the [4Fe-4S] cluster was additionally checked with data collected at the high energy site of the Fe-K-edge and was never found to be damaged (Fig. S2).

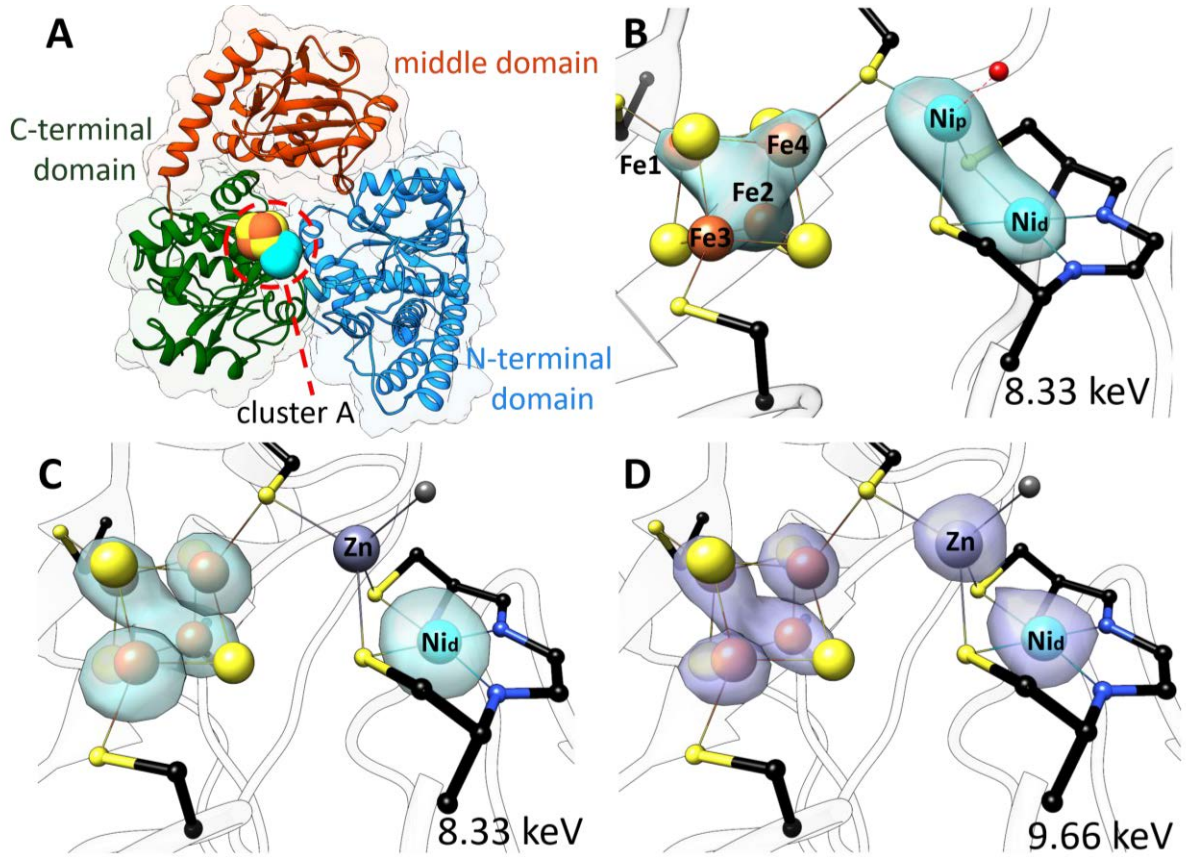

Figure 13: Crystal structure of $ACS_{Ch\text{-}closed}$ with the space group of $P2_12_12_1$. A) Ribbon representation of $ACS_{Ch\text{-}closed}$ with surface outline. B) Ni anomalous map at high Ni-K-edge (8.33 keV) from crystals grown with the metal-free optimization screens is shown in cyan surface at contour level 7.0 σ. C) Ni anomalous map of a crystal at high Ni-K-edge (8.33 keV) from the commercial stock solutions and citrate conditions is shown in cyan surface at contour level of 7.0 σ. D) Zn anomalous map of the same crystal as in C at high Zn-K-edge (9.66 keV) contoured at 5.0 σ (violet surface) confirms Zn ion at the M_p position of the cluster A. The K-absorption edge energy for Fe is 7.11 keV, for Ni 8.33 keV and for Zn 9.66 keV [135-137]. Same color code as in Figure 4. An unknown ligand on the Zn atom is depicted as grey sphere.

The $ACS_{Ch\text{-}closed}$ molecules in the crystal lattice have several inter-domain interactions of hydrophobic, hydrogen-bonding and salt bridges (Fig. 14). The three domains are in contact with each other by 6-16 residues (Tab. 8 and Tab. S2). In comparison, the previously published monofunctional $ACS_{Ch\text{-}open}$ (PDB-ID: 1RU3) exhibits inter-domain contacts with only 3-7 residues per domain without any observed

inter-domain contacts between the N-terminal domain and the middle domain (Tab. 8 and Tab. S2). This indicates a different arrangement of the N-terminal domain, which would explain why the molecular replacement with the complete 1RU3 model could not find a valid solution. The individual domain structure of the three domains of $ACS_{Ch\text{-}closed}$ shows no change in comparison to $ACS_{Ch\text{-}open}$. Superposition of $ACS_{Ch\text{-}closed}$ with the previously published $ACS_{Mt\text{-}closed}$ structure exhibits an rmsd of 1.03 Å, suggesting that the overall conformation of $ACS_{Ch\text{-}closed}$ is almost equivalent to $ACS_{Mt\text{-}closed}$.

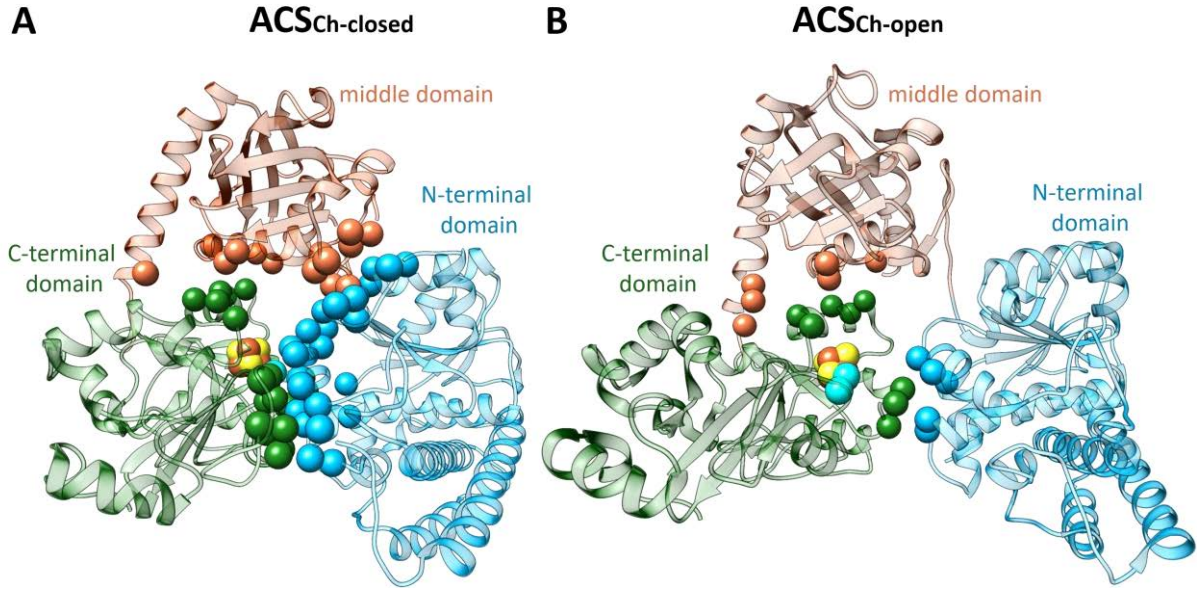

Figure 14: Interdomain contacts of $ACS_{Ch\text{-}closed}$ and $ACS_{Ch\text{-}open}$ (PDB-ID: 1RU3). Same color code as in Figure 4. Residues that are involved in interdomain contact are highlighted in spheres colored in their respective domain color. See Table S2 for more information.

Table 8: Number of residues that are involved as interdomain contacts between domains of $ACS_{Ch\text{-}closed}$ and $ACS_{Ch\text{-}open}$. A detailed list of the residues involved is shown in Table S2.

ACS_{Ch} domains	N-terminal domain – C-terminal domain residues	N-terminal domain – middle domain residues	C-terminal domain – middle domain residues
$ACS_{Ch\text{-}closed}$	16 – 14	11-9	6-6
$ACS_{Ch\text{-}open}$	5-3	-	5-7

In addition to the re-arrangement of the domains, $ACS_{Ch\text{-}closed}$ structure also shows local changes in the C-terminal domain, especially at cluster A. Ni_p is coordinated by three Cys residues and one water ligand and in a square planar coordination as in the $ACS_{Ch\text{-}open}$ structure (PDB-ID:1RU3), whereas Ni_p in $ACS_{Ch\text{-}closed}$ shows a distorted tetrahedral coordination geometry with same ligands as in the $ACS_{Ch\text{-}open}$ (Fig. 13B). The Ni_d stays in the square planar coordination geometry coordinated by the Cys-Gly-Cys motif. Since the distal and proximal position of cluster A is occupied with Ni ions in a different

conformation, this $ACS_{Ch\text{-}closed}$ structure depicts a potentially active state that was not seen before for the monofunctional ACS_{Ch}.

3.4.3 Molecular tunnel and observation of CO ligand binding

The differences in the interdomain contacts of the N-terminal domain to the middle domain and C-terminal domain between open and closed ACS_{Ch} structures also lead to change of surface accessible area ($ACS_{Ch\text{-}open}$ = 30928.7 $Å^2$, $ACS_{Ch\text{-}closed}$ = 28885.7 $Å^2$ calculated with PDBe PISA v1.52 [138]), which result in more exposure to the solvent and higher accessibility to cluster A from the solvent in $ACS_{Ch\text{-}open}$. The rearrangement of domains in $ACS_{Ch\text{-}closed}$ is most likely accompanied by a hinge movement at the N-terminal domain of 43.9 Å, resulting in a more compact structure as shown with more interdomain contacts and a reduced surface accessible area. $ACS_{Mt\text{-}closed}$ shows a tunnel connecting cluster A and cluster C of the ACS/CODH complex for CO delivery [69] and assumes that the compact and related structure of $ACS_{Ch\text{-}closed}$ could also harbor a molecular tunnel for CO delivery. Calculations of putative tunnels by the MOLEonline web server [139] revealed a tunnel that ranges from the proximal position of the cluster A through the N-terminal domain. This tunnel would allow CO molecules to enter $ACS_{Ch\text{-}closed}$, thus CO binds at the Ni_p of cluster A (Fig. 15A).

A superposition of $ACS_{Ch\text{-}closed}$ to the $ACS_{Ch\text{-}open}$ structure (PDB-ID: 1RU3) shows a gate for the CO tunnel that is controlled by the movement of Phe_{515} as a gate keeper, located at the end of the tunnel close to the Ni_P site (Fig. 15B). In the $ACS_{Ch\text{-}open}$ structure, conformation of the Phe_{515} residue closes the tunnel, which would hinder CO delivery from the tunnel to the Ni_p (Fig. 15B). In contrast, the Phe_{515} in the $ACS_{Ch\text{-}closed}$ is flipped outward to the cluster A (121°), which opens the tunnel and consequently allows CO to enter and to bind at the Ni_p.

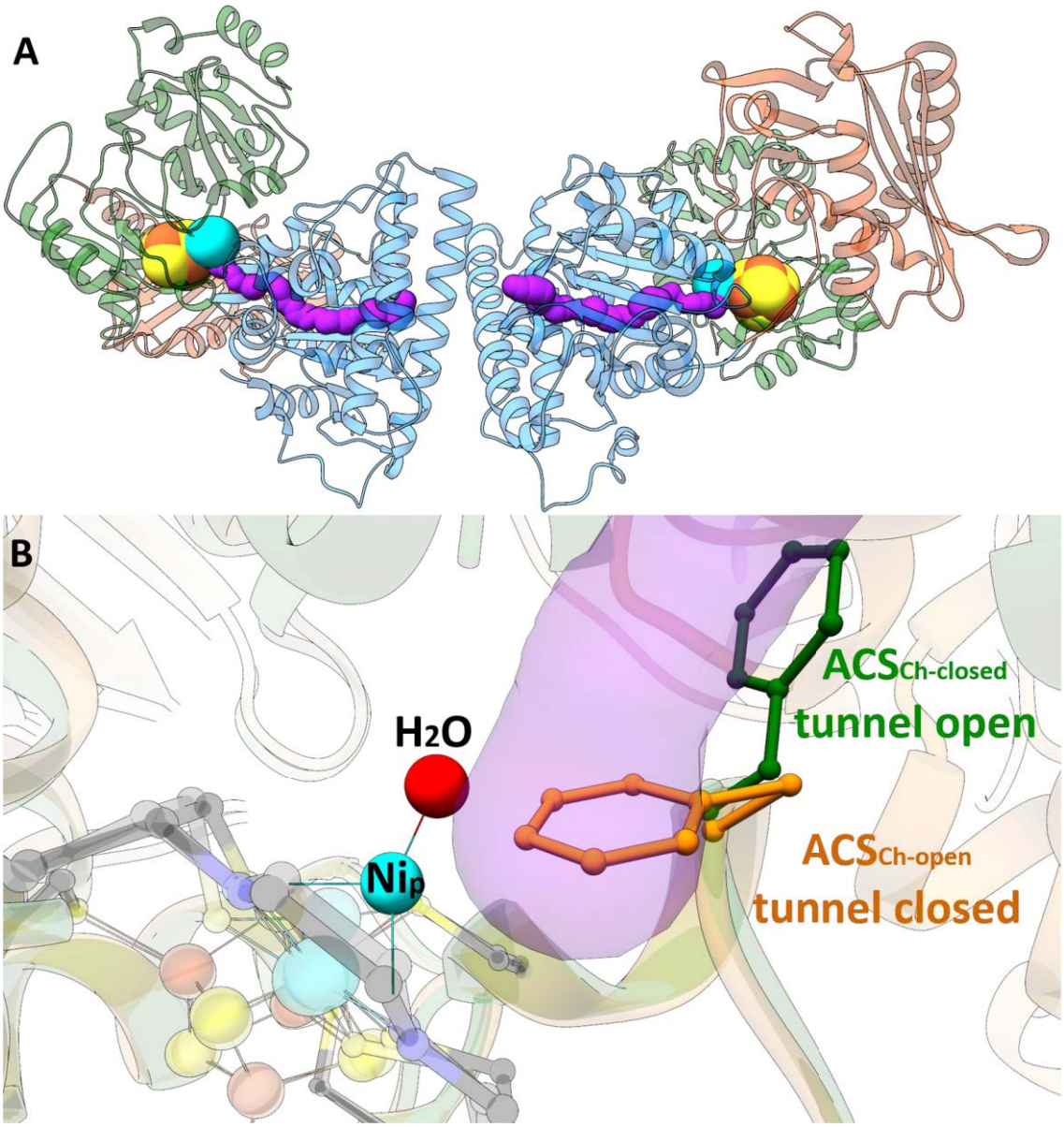

Figure 15: Molecular tunnel in $ACS_{Ch\text{-}closed}$. A) Calculated tunnel shows channels for both molecules in the asymmetric unit. Same color code as in Figure 4A. The tunnel is shown as magenta surface and starts at the N-terminal domain and ends at the Ni_p site of the cluster A. Tunnel calculations were done with the MOLEonline web server tool [139]. B) Superposition of the previously reported $ACS_{Ch\text{-}open}$ crystal structure (PDB-ID: 1RU3) with the crystallized $ACS_{Ch\text{-}closed}$ conformation. Same color code as in Figure 4. The end of the tunnel is shown as magenta surface.

$ACS_{Ch\text{-}closed}$ crystals were treated with CO in the presence of Ti(III)citrate as reducing agent to generate a CO-bound state of ACS_{Ch}. A crystal diffracted to a resolution of 2.0 Å (Fig. 12C) with unchanged cell constants (Tab. S1). Strong anomalous scattering contribution from Ni identified both nickel ions at the proximal and distal sites of cluster A (Fig. S3). As in the absence of CO, the Ni_p shows a tetrahedral geometry, while Ni_d shows unchanged square-planar coordination (Fig. 16). Both the CO-treated and the untreated crystals shows a positive density in the F_o-F_c map above the Ni_p (Fig. 16A and B). The refinement of the model into this electron density is discussed in the following paragraph.

The density can be completely satisfied with a coordinated water ligand without any residual electron density of the F_o-F_c map above 0.28 $e^-/Å^3$ in the untreated protein structure (Fig. 16C). In contrast to unchanged Ni_d site upon CO-gassing, the positive electron density above the Ni_p in the CO-treated crystal cannot be explained by a monoatomic water model (Fig. S4A). Therefore, modeling of the density with CO as a possible ligand clearly explain the observed electron density without leaving any (Fig. 16D) or a very small remaining positive electron density (Fig. S4D) in the F_o-F_c map after refinement depending on the $ACS_{Ch\text{-}closed}$ molecule in the asymmetric unit. Furthermore, modeling of the water molecule at the position of either carbon or oxygen of CO also results in remaining positive electron density, which supports the presence of a diatomic ligand at the Ni_p site (Fig. S4B and C).

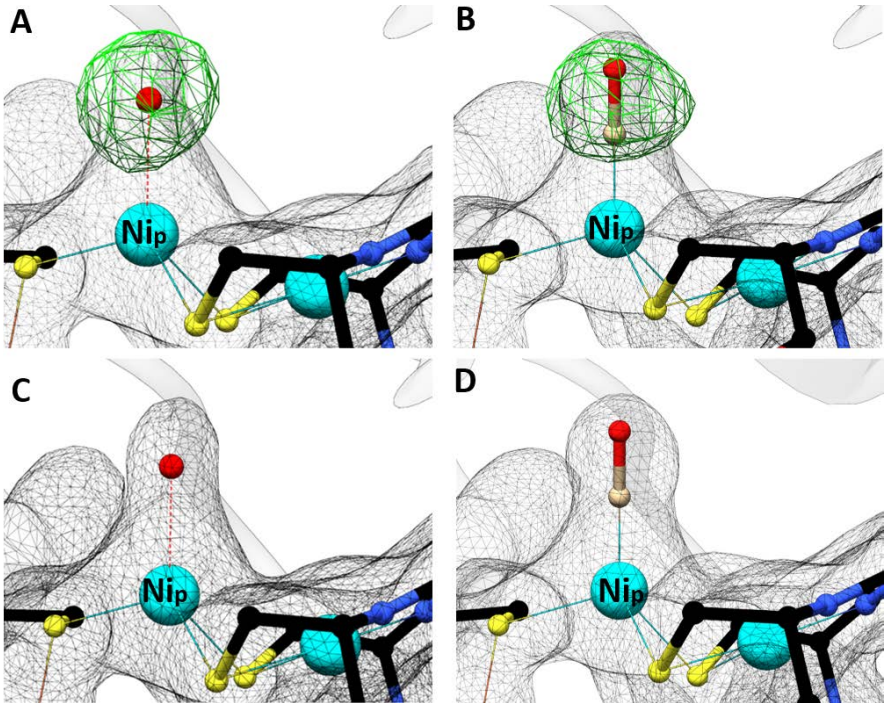

Figure 16: Electron density maps around the Ni_p ligand from CO treated and untreated crystals. A) A composite F_o-F_c omit electron density at the Ni_p of untreated crystal. B) A composite F_o-F_c omit electron density at the Ni_p of CO-treated crystal. C) The untreated $ACS_{Ch\text{-}closed}$ crystal with water as ligand. D) The CO treated $ACS_{Ch\text{-}closed}$ crystal with CO as ligand. Atoms are color-coded as in Figure 4, except carbon atom of CO (light brown). 2F_o-F_c map is shown as black mesh contoured at 1.0 σ and F_o-F_c map is shown as green mesh at 3.0 σ. The 2F_o-F_c maps were adjusted according to the maps comparison tool of the phenix suite, with the untreated structure as reference.

3.4.4 Hydrophobic CO-binding patch

As represented in Figure 15B, the binding of the CO ligand is restricted mostly by the position of Phe_{515} that allows CO to interact with Ni_p from the molecular tunnel in catalysis as in the untreated crystals of the $ACS_{Ch\text{-}closed}$ structures. The environment around the CO bound Ni_p site depicts additional residues from the N-terminal domain (Gly_{148}, Ile_{149}, Val_{152}, Phe_{232}) building a hydrophobic patch around the CO

molecule (Fig. 17). This arrangement with the surrounding residues functions to prevent CO release from the active site to the solvent as indicated by the van der Waals radii of the surrounding residues. The only natural substrate of ACS that could pass through the tunnel is CO, as CoA is too large to pass through the tunnel and the methyl moiety is derived directly from CoFeSP.

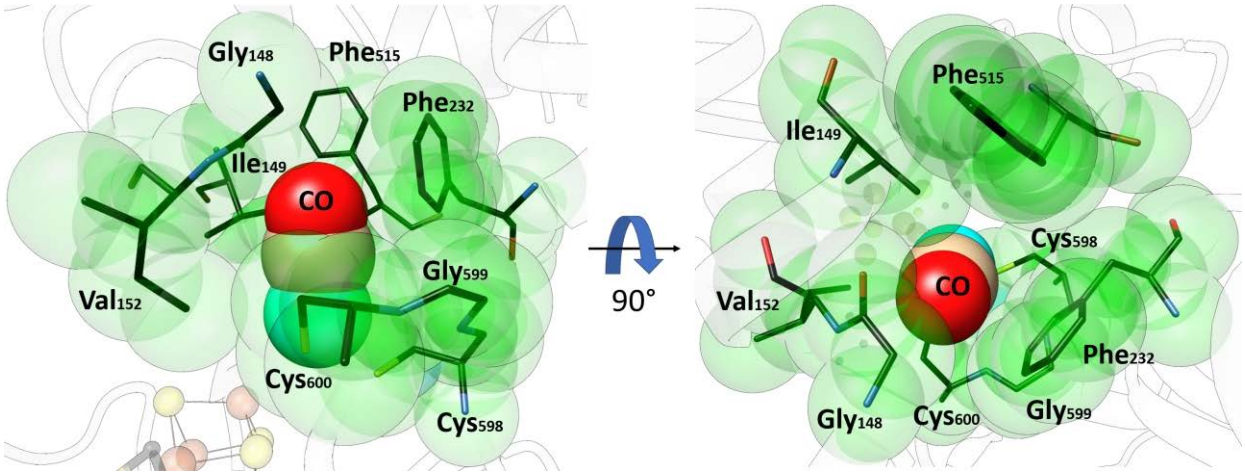

Figure 17: Binding pocket of the CO ligand in $ACS_{Ch\text{-}closed}$. The hydrophobic residues prevent CO leakage to the solvent. Van der Waals radii of the surrounding residues are shown as green spheres. Same color code as in Figure 16.

3.4.5 CO-binding on ACS_{Ch} in solution

To investigate the binding of CO at the cluster A in solution, ITC experiments were performed under anoxic reducing conditions (Fig. 18). The thermogram implies an exothermic interaction of CO with cluster A, which is enthalpically driven by favorable enthalpy change and can be described with a one-site binding model. The fit yields a K_D value of 9.4 µM for CO and a binding stoichiometry of 0.7 CO/ACS_{Ch}. This K_D is in the same order of magnitude as reported for *M. thermoacetica* [140]. Since the ITC experiment with CO yielded a stoichiometry of 0.7 CO/ACS_{Ch}, not all ACS_{Ch} molecules are able to bind CO under this condition.

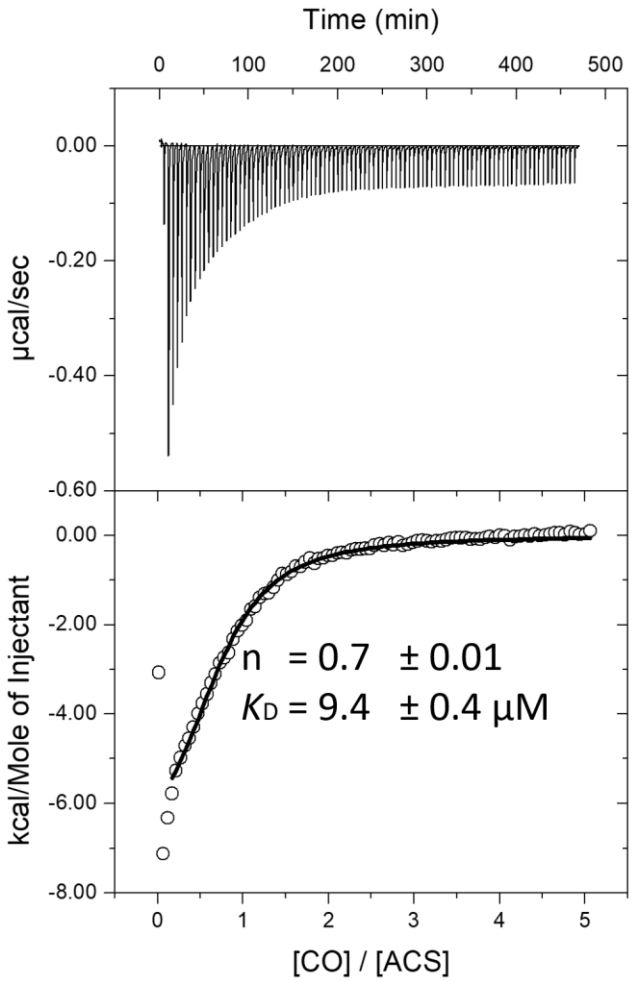

Figure 18: ITC of ACS_{Ch} with CO. The raw thermogram of the heat change by injection is shown in the upper panel, while the lower panel shows the integrated data (open circles) with the fit by one-binding site model (black line) and is normalized to the ratio of CO and ACS_{Ch} (0.04 mM) concentration. n indicates number of binding sites.

3.5 Structural and biochemical analysis of $ACS_{Ch\text{-}open}$

3.5.1 Crystallization of $ACS_{Ch\text{-}open}$ with CoA co-crystallized

ACS_{Ch} was crystallized in conditions containing MES, ammonium sulfate and CoA acting as an additive (Fig. 19; Materials and methods 2.6). The best crystal diffracted to a resolution of 2.3 Å. The crystals were of the trigonal space group $H3_2$ with the cell constants a = 199.3 Å, b= 199.3 Å, c = 168.2 Å, $\alpha = \beta = 90\ \gamma = 120°$ (Tab. S1). This space group and the unit cell parameters are almost identical to the previously reported $ACS_{Ch\text{-}open}$ conformation of *C. hydrogenoformans* (PDB-ID: 1RU3) and molecular replacement with the 1RU3.pdb as a search model for phasing information resulted in a correct solution. As the reported structure, one ACS_{Ch} molecule is found in the asymmetric unit and depicts ACS_{Ch} in the open conformation ($ACS_{Ch\text{-}open}$). XRF spectra of $ACS_{Ch\text{-}open}$ crystals were recorded to

determine the metal composition in the crystal (Fig. S1D). In contrast to $ACS_{Ch\text{-}closed}$ (Fig. S1B), only Ni and Fe are present without Ti or any trace amounts of Zn. Thus, $ACS_{Ch\text{-}open}$ crystallized without any contaminants and shows an intact cluster A, which is additionally proven by anomalous scattering data at the Ni K-edge (Fig. S5). The arrangement of Ni_d is equal to the $ACS_{Ch\text{-}closed}$ structure with a square planar coordination sphere, but Ni_p is also coordinated in a square planar coordination geometry, ligated by three Cys sulfurs and a fourth unknown ligand. Because these crystals were grown in a co-crystallization experiment with CoA and the prediction that $ACS_{Ch\text{-}open}$ is the potential state for CoA binding, the density was searched for the presence of a CoA ligand.

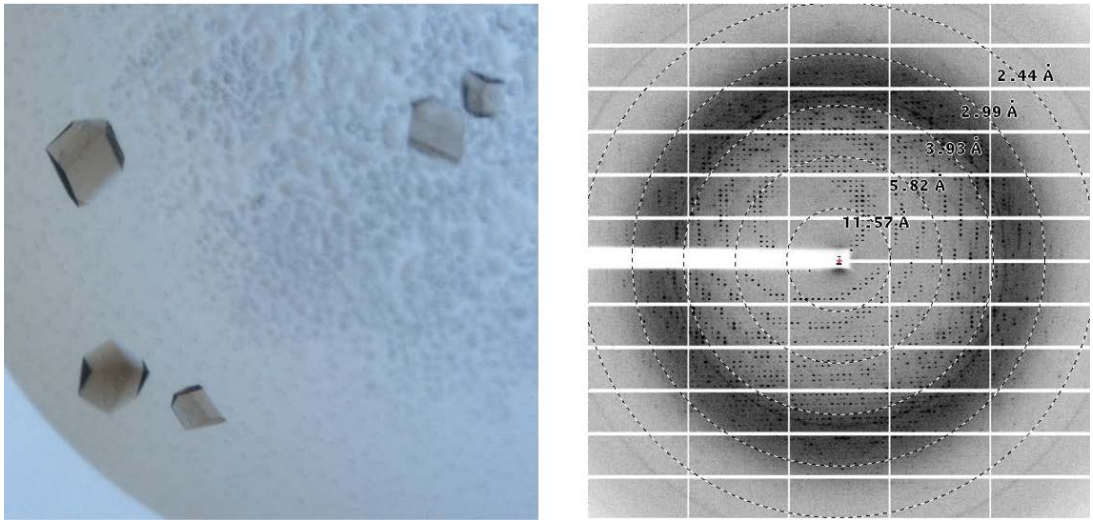

Figure 19: Co-crystallization of $ACS_{Ch\text{-}open}$. Left: Crystal from initial screening (Pi-minimal D5). Right: A representative diffraction image. Crystallization condition started with 8.3 mg/ml ACS_{Ch}. Formulation: 150 mM MES pH 6.0, 2 M ammonium sulfate, 5% v/v PEG 300 and 5 mM CoA trilithium salt.

3.5.2 CoA ligand modeling

In the crystal structure of CoA co-crystallized $ACS_{Ch\text{-}open}$ a strong positive electron density from the F_o-F_c map at the Ni_p as the fourth ligand was observed, where a water ligand was occupied in the $ACS_{Ch\text{-}open}$ structure (PDB-ID: 1RU3). However, the density in the CoA co-crystallized structure cannot be described by a water ligand (Fig. S6A). Additional positive electron density peaks are further visible around cluster A, indicating a presence of a larger and longer ligand than water (Fig. S7A).

Since the acetyl group has to be transferred to the thiol group of CoA for acetyl-CoA synthesis, the cysteine and pantothenate moiety of CoA were used as a starting model for CoA as ligand, where the sulfur atom covalently binds at Ni_p (Fig. S7B). This refinement results in observation of additional positive density around the pantothenate part of the CoA molecule. This was used as guidance for model building of CoA. Adding of the diphosphate group and the ribose of the adenosine part of CoA

resulted in appearance of additional density as well (Fig. S7C and D). Finally, modeling the missing part of CoA (adenine) into the remaining density led to no further additional densities (Fig. S7E). The final model satisfies the electron density of the F_o-F_c map with occupancy of 65%.

Only some main features are shown in the 2F_o-F_c map (contoured at 1.0 σ), as two phosphate groups, the cysteine group, parts of the adenosine ring and the pantothenate group, inferring that CoA is very flexible in this state which is further supported by the high average b-factor of the molecule (91.8 Å^3) (Fig. 20A). Most of the missing features appear in the 2F_o-F_c map contoured at 0.5 σ. However, components from the crystallization condition can be excluded, since modeling of MES or sulfate results in the appearance of negative electron density and does not fit into the shape of the electron density and interacting environment at the cluster A (Fig. S6B and C).

To identify the atom bound to the Ni_p, anomalous scattering data for sulfur were recorded at 6.50 keV, which shows that the sulfur atom of CoA is buried inside the bulky S-anomalous electron density and argues for the presence of a sulfur atom (thiol group) of CoA at the Ni_p (Fig. S8). Although the resolution for anomalous data of this dataset is only 4.3 Å with a SignAno (mean anomalous difference in units of its estimated standard deviation, (|F(+)-F(-)|/Sigma) and F(+), F(-) are structure factor estimates obtained from the merged intensity observations in each parity class [122]) value of 1.01, anomalous map was calculated using resolution at 6.5 Å. It has to be noted that at this resolution there is contribution of S-anomalous from sulfur atoms of the [4Fe-4S] cluster and cysteine sulfurs coordinating Ni atoms. Therefore, it is difficult to distinguish cluster sulfur and CoA sulfur atoms.

The 2F_o-F_c map calculated after modeling of CoA does not show all features of CoA, most likely due to its high flexibility. This could result in loss of a clear map due to bulk solvent contribution or the strong signal appearing from the heavy metals present in the cluster A, which could obscure weak signals from the flexible CoA ligand. For that reason a feature-enhanced map (FEM) was calculated, producing a map that possesses a reduced level of noise, model bias and scales weak and strong features to the same level [141]. The resulting FEM map shows all main features of the CoA ligand at the same-scaled contour level in comparison to the 2F_o-F_c map (Fig. 20B).

A second approach to enhance the quality of the electron density map was done by calculation of a polder map [142]. Since this tool excludes bulk solvent contributions to the electron density map, weak and flexible features like ligands and protein loops are enhanced using this map tool. Comparison of the omit and polder maps (Fig. S9B) with the 2F_o-F_c map (Fig. S9A) shows enhanced signals for the already present parts of CoA in the omit map and additional features in the polder map. The calculated correlation coefficient (cc) of the map with ligand and real F_{obs} data (cc_{m1m3} = 0.82 and peak cc_{m1m3} = 0.76) are higher than for the map without ligand and real F_{obs} data

(cc_{m2m3} = 0.54 and peak cc_{m2m3} = 0.47) or the maps with and without the CoA ligand (cc_{m1m2} = 0.46 and peak cc_{m1m2} = 0.40), in which m1 corresponds to calculated F_{obs} with the ligand and m2 to calculated F_{obs} without ligand and m3 to real F_{obs} data. According to these values, it is most likely that the electron density of the polder map corresponds to model feature and not to bulk solvent, which again supports the presence of CoA in the crystal structure.

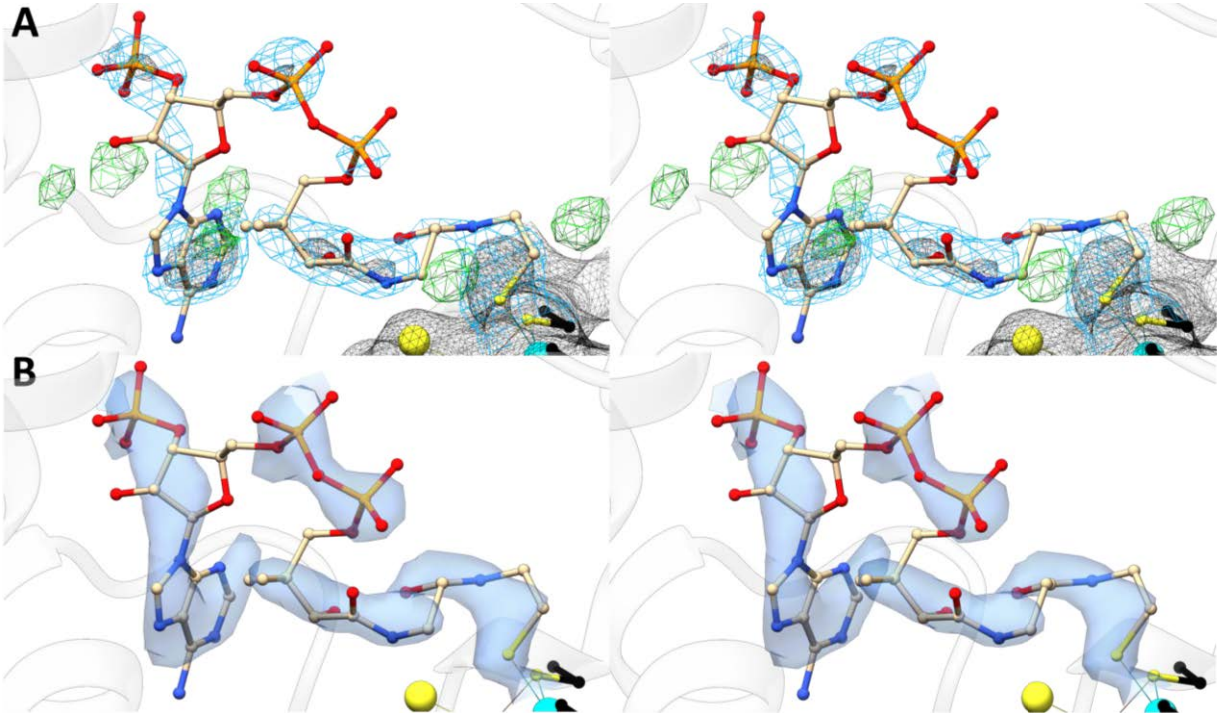

Figure 20: Stereo view of different maps for CoA. A) $2F_o$-F_c map in black mesh (contoured at 1.0 σ), in light blue mesh (contoured at 0.5 σ) and F_o-F_c map in green mesh (contoured at 3.0 σ) after full refinement with complete CoA molecule. B) Calculated FEM for the CoA model in A. FEM in dark blue surface are contoured at 1.0 σ. The FEM map was adjusted according to the maps comparison tool of the phenix suite [130], with the $2F_o$-F_c map contoured at 1.0 σ as reference. Atoms are color-coded as in Figure 4, except carbon atom of CoA (light brown) and P in orange.

The surrounding environment of the CoA ligand shows that the adenosine phosphate part of the molecule is coordinated by residues from the middle domain and the C-terminal domain (Arg_{408}, Arg_{409}, Asp_{538} and Asn_{551}) (Fig. 21 and Fig. 22). The adenine ring builds one hydrogen bond to the oxygen atom in the backbone of Asp_{538} and is further interacting by positively charged interaction with Arg_{408}. Furthermore, the 3-phosphogroup interacts with Arg_{409} by electrostatic attraction. These few stabilizing interactions explain the flexible behavior of the CoA ligand in the structure. These parts, the adenine and the 3-phosphogroup, of the CoA are the most visible ones in the calculated maps due to the interaction with the protein, except for the cysteine sulfur that is covalently bound to Ni_p.

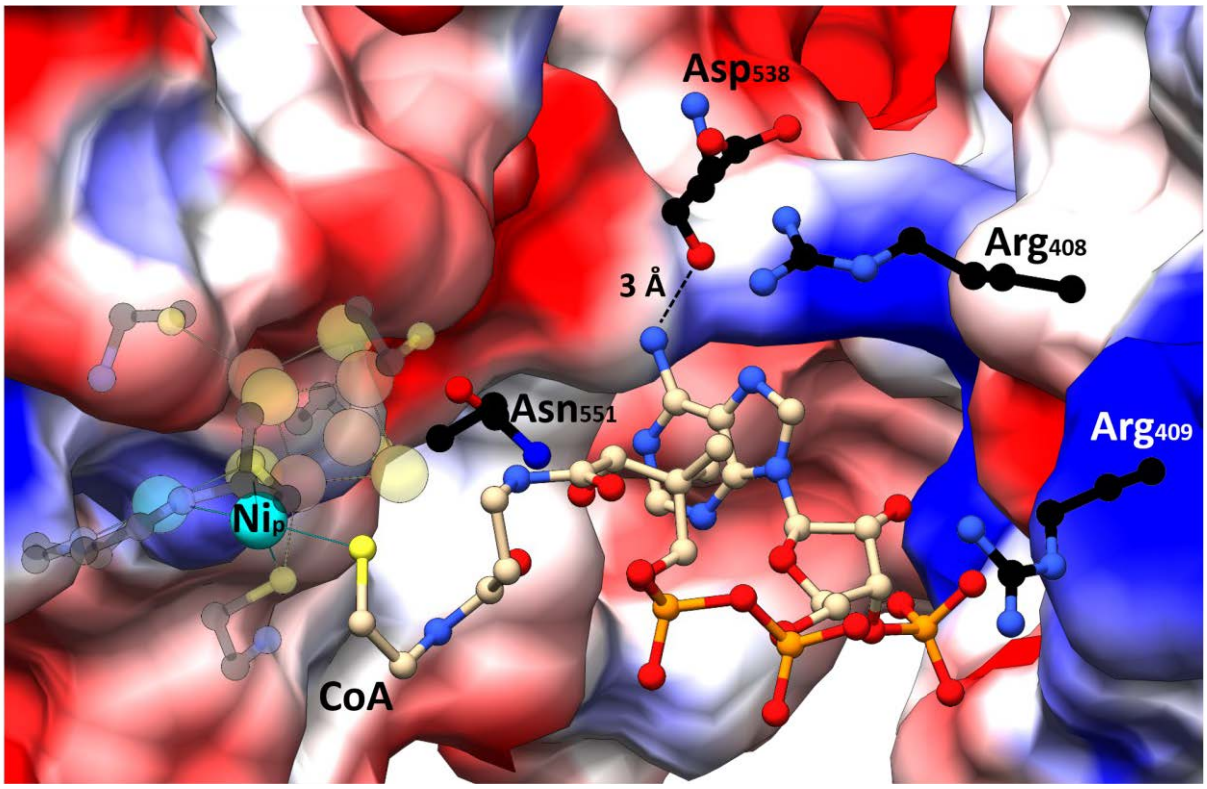

Figure 21: Electrostatic map and coordination environment around the CoA ligand. CoA binds with its sulfur atom at Ni_p. The adenine ring of CoA interacts by a hydrogen bond (black dashed line) with Asp_{538}. Additional stabilization is driven by salt bridge between the 3-phosphogroup and Arg_{409}. Models are color-coded as in Figure 20. Blue surface corresponds to positively, white to neutral and red to negatively charged regions of the protein. Electrostatic calculations were done using the PDB2PQR and APBS web server[143, 144].

A view of the van der Waals radii of the CoA molecule and the $ACS_{Ch\text{-}open}$ surface shows the binding pocket for CoA. The CoA model does not show any clashes of the molecule with the $ACS_{Ch\text{-}open}$ surface (Fig. 22). The adenine moiety of CoA is embedded in the binding pocket, where the phosphate groups are directed to the solvent site, which is a common feature of CoA binding proteins [145]. As CoA binding proteins catalyze a wide range of reactions, they also differ in the topology of CoA binding, for instance, involving a TIM barrel motif in methylmalonyl-coenzyme A mutase and a Rossman fold in succinyl-CoA synthase [146, 147].

Since the middle domain of ACS_{Ch} in the $H3_2$ space group did not contribute to the crystal packing and the solvent content of these crystal is quite high with 69%, the electron density of the middle domain is weaklier defined in contrast to the other domains. This contributes additionally to the flexibility of CoA in the crystal because of the coordination of CoA by residues of the middle domain and CoA may

exist in different conformations (Fig. S10), except for the cysteine moiety of CoA which binds to Ni_p.

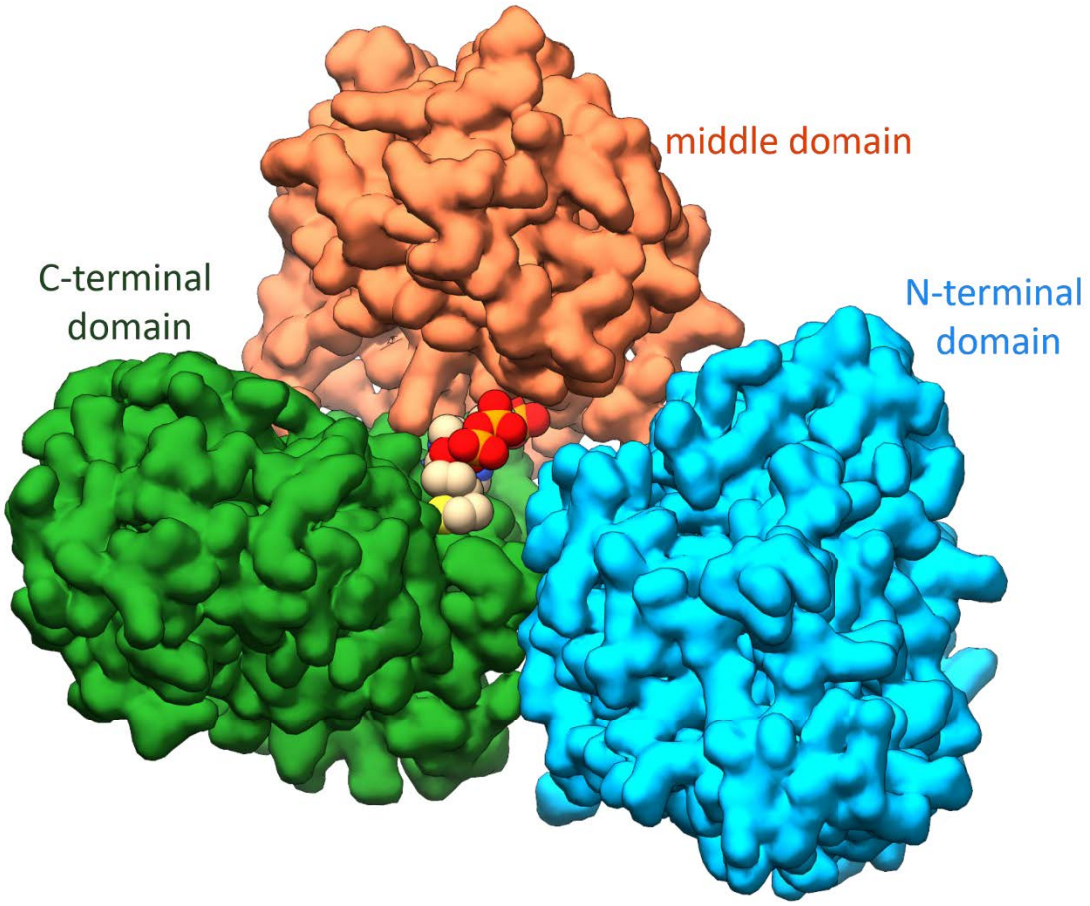

Figure 22: Van der Waals radii of the CoA molecule. The CoA molecule fits well into the $ACS_{Ch\text{-}open}$ binding pocket between the C-terminal domain and middle domain without clashing with the protein surface. The adenine ring is embedded into the protein, whereas the phosphate groups are directed to the solvent site. Same color code as in Figure 15. The domains are colored as in Figure 4A.

3.5.3 CoA-binding to ACS_{Ch} in solution

To understand the interaction of CoA with ACS_{Ch} in more detail, ITC experiments were performed, as for CO binding before, to determine the affinity and stoichiometry of the CoA binding. The CoA titration was performed under anoxic conditions without reducing agents because the crystallization condition did not contain reducing agents. In contrast to CO-binding, CoA-binding is endothermic and entropically driven. The data can be fitted very well with a one-binding site model (Fig. 23).

The model fit gave a K_D value of 3.1 µM and a stoichiometry of 0.8 for CoA binding. This affinity is in agreement with the ACS/CODH complex from *M. thermoacetica* (K_D = 10 µM), which can be increased in the presence of titanium citrate (K_D = 36 µM) [148]. Furthermore, CoA was found to act as competitive inhibitor in the CO/acetyl-CoA exchange reaction with a K_i of 7 µM [149, 150]. Nonetheless these values are all for the ACS/CODH complex at higher temperatures (50-55 °C) and lower

pH (5.0-6.0), which have to be taken into account for direct comparison of these values. Binding of [3'-^{32}P]-CoA showed even two binding sites of CoA for the ACS/CODH complex. The first K_D value of 52 µM is 17-fold higher than the calculated K_D value of the ITC experiment, but still in the same dimension. The second binding site has an K_D of 2.5 mM [151], which is not indicated in the ITC data of this work that is monophasic (Fig. 23). Nevertheless, a second binding site in ACS_{Ch} for CoA with a high K_D cannot be excluded.

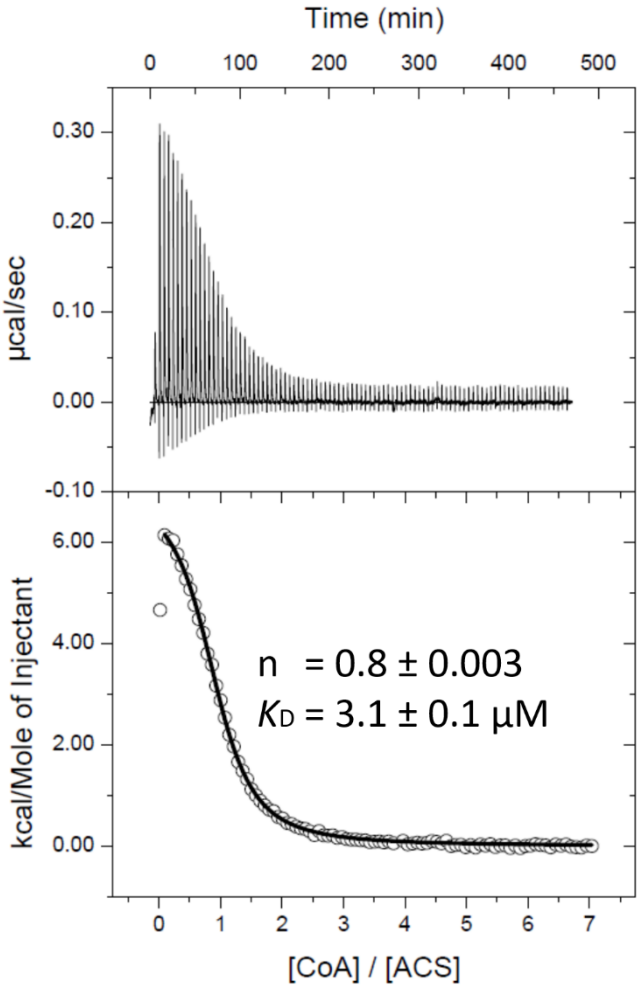

Figure 23: ITC experiment of ACS_{Ch} with CoA. The raw data are shown in the upper panel. The lower panel shows the heat change for each injection (open circle), normalized to the ratio of CoA and ACS_{Ch} concentration and fitted to a one-site model (black solid line). n indicates the number of binding sites.

3.6 Comparison of cluster A coordination

All ACS_{Ch} crystals determined in this work show different states of the monofunctional ACS_{Ch} and are compared to investigate changes at the catalytic site (Fig. 24A-E). The main structural variation is as mentioned above the coordination sphere of the Ni_p position. Although the previously reported structure of the monofunctional $ACS_{Ch\text{-}open}$ (PDB-ID: 1RU3) and $ACS_{Ch\text{-}open}$:CoA has the Ni_p position in a

square planar coordination sphere, the as-isolated, CO treated and Zn bound $P2_12_12_1$ crystals show the $ACS_{Ch\text{-}closed}$ state where the M_p position is always coordinated by three conserved Cys residues and a different type fourth ligand in a distorted tetrahedral fashion. Previous crystal structures of the ACS/CODH complex from *M. thermoacetica* with Zn and Cu at the M_p position also show an ACS_{closed} conformation [62, 68].

The switch of the Ni_p ion from square planar to distorted tetrahedral is accompanied by an elongation of the bond length of Ni_p and Ni_d to the S^γ atoms of Cys_{598} and Cys_{600} by 0.1-0.2 Å while a shortening of the Ni_d-Ni_p distance by 0.2 Å was observed (Fig. 24). The bond length between the Ni_p and the bridging sulfur of Cys_{512} is not changed from the $ACS_{Ch\text{-}open}$ to the $ACS_{Ch\text{-}closed}$ state of untreated but increased by 0.2 Å in the CO treated $ACS_{Ch\text{-}closed}$ crystal. In the CO-bound $ACS_{Ch\text{-}closed}$, the distance to the ligand is shortened to 1.8 Å and the bond angle of Ni_p-C-O is 177° (Fig. 24A-D and Tab. 9).

EXAFS studies of ACS_{Mt} under CO treatment [152] show a change in the Ni-Ni distance from 2.96-2.78 Å that goes hand in hand with an elongation of the Ni-S distance from 2.18 Å into two different types of Ni-S distances of 2.22 Å and 2.33 Å. In comparison, the CO-bound structure depicts a Ni-Ni distance of 2.8 Å, Ni_p-S distances of 2.4 Å and Ni_d-S distance of 2.2-2.3 Å (Fig. 23D). These values are close to the values of CO bound ACS_{Mt} in the EXAFS studies. Furthermore, the values of $ACS_{Ch\text{-}open}$ and $ACS_{Ch\text{-}open}$:CoA with a Ni-Ni distance of 3.0 Å and 2.9 Å are consistent with the determined values of the EXAFS studies without CO treatment [152]. This indicates that these changes are driven by the conformational switch of ACS_{open} to ACS_{closed}, which is associated with the change of the Ni_p coordination sphere from the square planar coordination to the distorted tetrahedral coordination.

Table 9: Measured bond angles of the cluster A from *C. hydrogenoformans* structures.

Bond angles (°)	$ACS_{Ch\text{-}open}$:Ni	$ACS_{Ch\text{-}closed}$:Ni	$ACS_{Ch\text{-}open}$:CoA	$ACS_{Ch\text{-}closed}$:CO	$ACS_{Ch\text{-}closed}$:Zn_p
Ni_p-C-O	-	-	-	178.1	-
N_{600}-Ni_d-N_{599}	85.6	81.1	83.8	86.4	84.3
N_{599}-Ni_d-S_{598}	106.6	105.1	102.9	97.1	98.9
S_{598}-Ni_d-S_{600}	82.4	85.5	93.0	87.4	85.5
S_{600}-Ni_d-N_{600}	85.4	88.4	80.4	89.1	91.3
Ni_d-S_{600}-M_p	88.2	71.5	75.0	75.3	75.4
Ni_d-S_{598}-M_p	84.3	73.4	78.9	74.9	75.0
S_{600}-M_p-S_{598}	76.4	83.3	91.1	79.4	78.3
S_{598}-M_p-S_{512}	107.4	93.6	102.5	104.3	106.5
S_{512}-M_p-S_{600}	174.3	114.9	166.5	116.2	121.2
L-Ni_p-S_{600}	94.5	102.8	81.1	102.1	-
L-Ni_p-S_{512}	81.0	116.1	85.5	111.2	-
L-$Ni_p$$S_{598}$	167.2	142.1	166.6	138.6	-

All values are mean values from the two ACS_{Ch} copies inside the ASU, except for the $ACS_{Ch\text{-}open}$ and $ACS_{Ch\text{-}open}$:CoA structure.

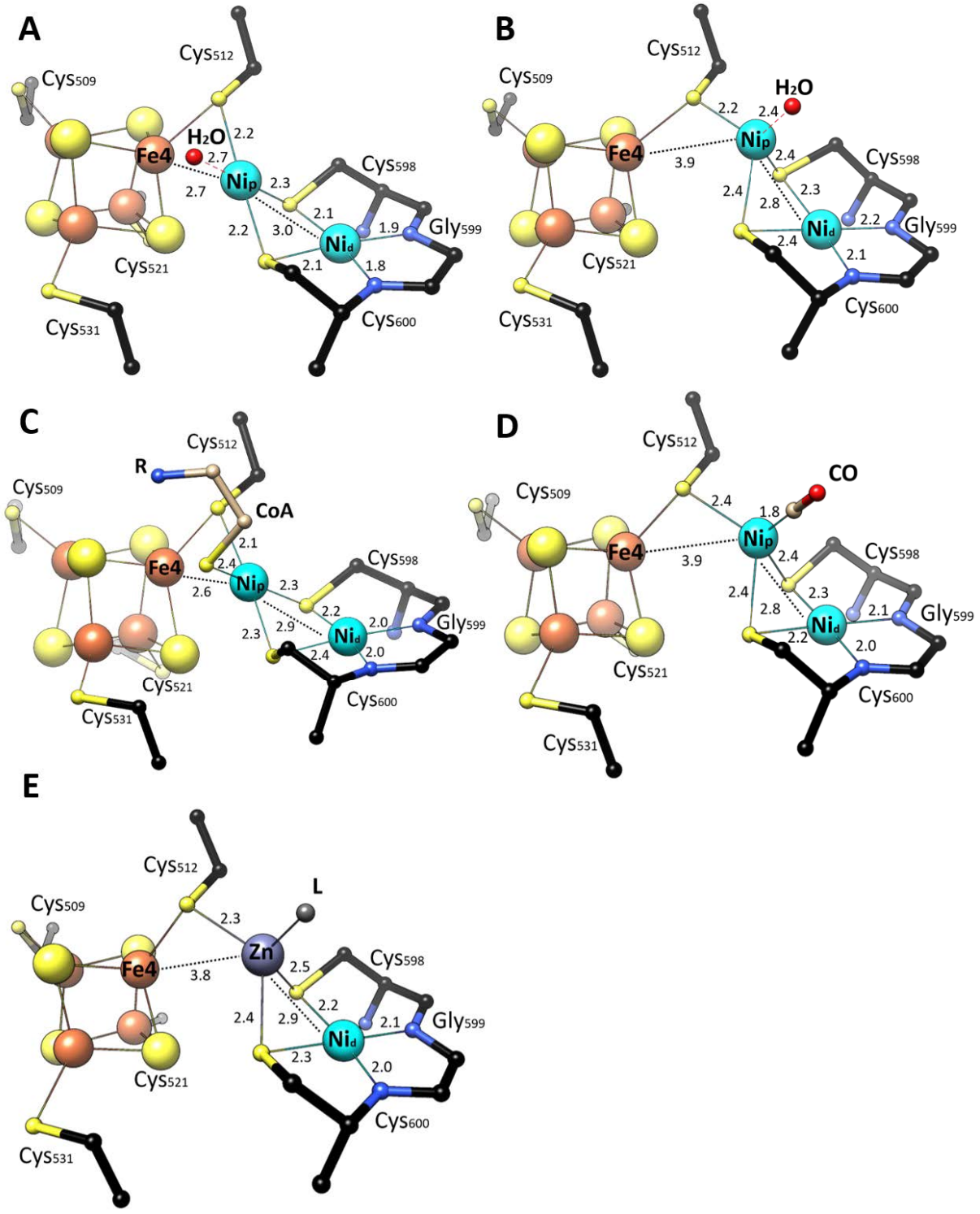

Figure 24: Comparison of cluster A from different ACS_{Ch} crystals. A) $ACS_{Ch\text{-}open}$ PDB-ID: 1RU3. B) $ACS_{Ch\text{-}closed}$. C) CoA-bound in $ACS_{Ch\text{-}closed}$. D) CO-bound in $ACS_{Ch\text{-}open}$ E) $ACS_{Ch\text{-}closed}$ with Zn at the proximal position of the cluster A. The cluster A structures are represented in ball-and-stick model. Same color code as in Figure 13. Bond lengths are given in Å and mean values from the two $ACS_{Ch\text{-}closed}$ copies inside the ASU, except for the $ACS_{Ch\text{-}open}$ and $ACS_{Ch\text{-}open}$:CoA structure.

4 Discussion

4.1 $ACS_{Ch\text{-}closed}$ and $ACS_{Ch\text{-}open}$ conformational states

The crystallographic and biochemical methods used in this work provide basic structural insights regarding how ACS interacts with CO and CoA. The monofunctional ACS of *C. hydrogenoformans* can acquire at least two different conformational states. These states were also known from the ACS/CODH complex, but not for the monofunctional ACS_{Ch}. The observed and determined crystal structures with different ligands in this study (CO and CoA) support the importance of two conformational states, $ACS_{Ch\text{-}open}$ and $ACS_{Ch\text{-}closed}$, of the monofunctional ACS_{Ch}.

In the closed conformation of ACS_{Ch}, a gas channel exists which can guide CO molecules through the N-terminal domain and ends at cluster A, directly above the Ni_p site. Such a channel exists in the bifunctional ACS/CODH complex of *M. thermoacetica* showing ACS_{Mt} in the closed conformation [69] and connects cluster C and cluster A. Both the calculated tunnel of ACS_{Ch} in the closed conformation and the tunnel section of the $ACS_{Mt\text{-}closed}$ are superimposable suggesting that a molecular tunnel leading to cluster A is conserved in ACS.

A recently published crystal structure of the ACS/CODH complex from *Clostridium autoethanogenum* shows a different arrangement of the complex [72]. The complex consists of two ACS and CODH molecules as in *M. thermoacetica* but only one ACS monomer is in contact with one CODH monomer and not in contact with both CODH molecules. This complex formation results in a different channel arrangement connecting the cluster C and cluster A. Additional channels indicating separate delivery possibilities of CO, which could serve to channel CO from the solvent directly to cluster A, depending on the CO concentration. This could act as another system for ACS regulation depending on CO concentration.

The Phe_{515}, acting as a gate keeper at the end of the tunnel, is moved away in the closed conformation from Ni_p to allow CO binding. This Phe residue is highly conserved among all ACS proteins and kinetic analysis of the ACDS β-subunit of *M. thermophila* indicates, that the Phe sidechain controls CO binding at ACS [153]. This gating mechanism controlled by the conformation of ACS_{Ch} is the same as the reported channel system of the ACS/CODH complex, in which the gating mechanism is physiologically used to control the flux of CO from the active site of CO_2 reduction of cluster C to cluster A [69, 154]. These results imply that $ACS_{Ch\text{-}closed}$ obtained in this study is equivalent with the reported closed conformation of ACS from *M. thermoacetica* bifunctional complex, in which cluster A and cluster C are connected via the gas channel and leads to the assumption that $ACS_{Ch\text{-}closed}$ is ready to bind CO.

Treatment of the $ACS_{Ch\text{-}closed}$ crystal with CO led to a change of the fourth ligand coordinating the Ni_p, which can be modeled with CO (Fig. 16D). However, at a resolution of 2.0 Å, CO cannot be modelled without any doubt, because the individual atoms are not visible and one cannot inevitably prove a CO molecule using observed electron density. For that, a high-resolution structure would be necessary, where a clear diatomic ligand would be visible by separate electronic maxima for the carbon and oxygen atom of CO. Moreover, in the CO model, a small positive electron density remains in one of the two $ACS_{ch\text{-}closed}$ molecules of the asymmetric unit that cannot be described by the CO molecule alone. This could be explained by the possibility of a mixture of $ACS_{Ch\text{-}closed}$ molecules, which have CO or water as the fourth coordinated ligand of Ni_p (Fig. S4D). Nevertheless, the untreated (d_{min} = 2.1 Å) and CO-treated crystal (d_{min} = 2.0 Å) were solved at nearly the same resolution, which allow comparison of their structures.

Several additional hydrophobic residues of the N-terminal domain surround the CO molecule in a binding pocket to hinder CO leakage (Fig. 17). The cluster A in the closed conformation is buried in the protein interior, preventing access of large molecules such as CoA. By a rearrangement of the domains $ACS_{Ch\text{-}closed}$ can attain the open conformation and increases the solvent exposure of ACS_{Ch}, which interrupts the gas channel and the moving of Phe_{515} prevents remaining CO in the tunnel to bind at the Ni_p.

The resulting $ACS_{Ch\text{-}open}$ has significantly fewer interdomain contacts, especially of the middle and C-terminal domains to the N-terminal domain. Additionally, the hydrophobic CO pocket is disrupted and cluster A itself is less buried inside the protein, which increases the availability of cluster A for a larger molecule to approach from the solvent. The crystal structure of $ACS_{Ch\text{-}open}$:CoA showed that CoA binds at the Ni_p with its thiol group and is further stabilized by residues of the middle and C-terminal domains (Fig. 21), in contrast to the CO-coordinating environment that involves residues from the C- and N-terminal domain (Fig. 17). This additional space could be crucial for CoA binding, since the space available in $ACS_{Ch\text{-}closed}$ would not be sufficient to coordinate CoA in the same fashion as in the open conformation (Fig. S11). This is also supported by CoA dialysis studies, which showed that CoA is not able to bind to CO-bound ACS [148]. The open conformation of ACS could also be responsible for binding of acetyl-CoA to start the reverse reaction or for acetyl-CoA release after product formation.

A recent negative-stain cryo EM structure indicates further structural variance of ACS_{Mt} in the ACS/CODH complex, with further domain movements of the middle and C-terminal domains, resulting in an even more solvent exposed cluster A [155]. Their docking simulations suggest that these additional conformations could be of relevance for the methyl group transfer from CoFeSP, since the open and closed conformations are not accessible for CoFeSP to interact with the Ni_p of cluster A. However, there is no apparent structural data for this simulation. The observed conformation in the

negative-stain could also be of relevance for the cluster A maturation, since an additional protein (AcsF) can insert up to two nickel ions at the expense of ATP into the cluster A [63] or interaction with currently unknown cofactors or other proteins, responsible for cluster A reduction, for instance.

4.2 CO- and CoA-binding on ACS_{Ch}

The binding of CO in the ITC experiment of this study results in a K_D value (9.4 µM) comparable with previously reported values for the ACS/CODH complex from *M. thermoacetica*. CO-titration of the ACS/CODH complex showed a K_D of 3 µM by EPR for CO binding, which could be reduced to 0.3 µM by CO_2 titration [140]. In comparison, CO-titration of the ACS_{Mt} without the CODH subunit developed an EPR signal with a K_D of 30 µM [156]. This led to the assumption that the complex is more efficient for channeling CO molecules through the tunnel to the active site, especially under CO_2 reducing conditions.

Another EPR experiment performed with the β-subunit of ACDS from *M. thermophila* exhibits a lower affinity for CO (K_D = 0.65 mM) [153]. This results most likely due to the missing N-terminal domain, which is not conserved in the ACS from archaea. As this is the domain which harbors the tunnel region of the enzyme for CO delivery in bacteria. Additionally, the K_D of the ACDS β-subunit was decreased by exchanging Phe_{195} to Ala (K_D = 0.12 mM), which corresponds to Phe_{515} in ACS_{Ch} that shields the Ni_p in $ACS_{Ch\text{-}open}$ [153]. These findings underline the importance of the CO channel in ACS and the Phe_{515} residue for the mechanism and substrate engagement.

The model fit of the ITC experiment corresponds to a stoichiometry of 0.7 CO/ACS indicating a mixture of ACS_{Ch}:CO and ACS_{Ch} states. This is in line with a mixture of CO bound and water coordinated to Ni_p at cluster A in the crystal structure (Fig. S4D). In the ACS/CODH complex of *M. thermoacetica* CO can act as a competitive inhibitor for ACS in the methyl transfer reaction (K_i = 180 µM) and as a noncompetitive inhibitor in the CoA/Acetyl-CoA exchange reaction (K_i = 0.4 mM) [96, 151, 157]. Therefore, it cannot be ruled out that the CO treated $ACS_{Ch\text{-}closed}$ structure (Fig. 16D) reflects an inhibited state of the enzyme.

The obtained K_D from the ITC experiment in this work is closer to K_D values of reported active ACS [140, 156]. Additionally, the ITC and crystallization of ACS_{Ch} were done in the absence of other substrates that could drive ACS into an inhibited state, like in the methyl transfer reaction [96]. These observations could argue that the CO binding measured in this ITC corresponds to a catalytically competent state. Previous studies have proposed that ACS can distinguish whether CO has approached from the tunnel or solvent site, and that a second CO molecule bound to Ni_p generates an inhibited

state of ACS [157, 158]. The binding of a second CO molecule to the Ni_p site cannot be observed by the ITC data under the experimental conditions. Thus, it appears that a second CO binding would have a high K_D value or did not bind to the Ni_p site.

CO and the methyl moiety bind at the Ni_p site during catalysis reacting to an acetylated intermediate at Ni_p, which transfer to CoA to form an acetyl-CoA. Therefore, CoA may bind also to the Ni_p site. Previous EPR studies showed, that CoA binding alters the NiFeC signal and CoA binds most likely directly or in close proximity of the cluster A [150, 159]. Since, for CoA binding, there is no common binding motif in proteins known, it is difficult to predict which residues are involved in CoA binding and coordination.

Nevertheless, the binding coordination in the $ACS_{Ch\text{-}open}$ structures resembles the CoA coordination in the citrate synthase of the pig heart [160]. In citrate synthase, the CoA molecule is tightly packed between the two domains of the citrate synthase and has a 180° turn at the pyrophosphate. This bending is also present in the $ACS_{Ch\text{-}open}$ CoA bound state and CoA is situated between the middle and C-terminal domain of $ACS_{Ch\text{-}open}$. Interestingly, citrate synthase has also two different conformational states, named open and closed, according to the different solvent access, driven by 18° rotation of one domain. In contrast to ACS_{Ch}, the closed conformation of the citrate synthase is involved in CoA binding and synthesis, while the open conformation is responsible for product release. The catalytic mechanism of ACS is not completely understood, but in the closed conformation, ACS would not allow CoA to bind in the same fashion as in the open conformation, due to the limited space around cluster A and the clash of the cysteine part of CoA with Ile_{149} and Val_{152} of the CO binding cavern (Fig. S11). Indicating that the two conformations might represent intermediates in the reaction cycle.

CoA interacts with two Arg residues (Arg_{408} and Arg_{409}) by electrostatic forces (Fig. 21). Arg_{408} and Arg_{409} are also conserved in the ACS/CODH complex of *M. thermoacetica,* where chemical modifications of Arg residues with phenylglyoxal resulted in inactivation of the acetyl-CoA synthesis [161]. This inhibition was prevented by incubation of CoA before the chemical modification [161], which might reveal the important function of the conserved two Arg residues for CoA binding. As mentioned above for acetyl-CoA synthesis, CoA is expected to bind as the last substrate and leads to the assumption that the CoA bound state is potentially an inhibited state of ACS_{Ch}. This inhibited state could block Ni_p for methylation through CoFeSP or acetyl-CoA binding for the reverse reaction and hinders the conformational switch to $ACS_{Ch\text{-}closed}$. Furthermore, the space above Ni_p in $ACS_{Ch\text{-}closed}$ is not sufficient for CoA and would require a precedent dissociation of CoA for CO or CH_3-CoFeSP binding. The place for acyl group transfer is the Ni_p site, as it was shown for synthesized Ni centers thioester formation at a Ni site, carrying an acyl group [162]. This indicates a similar coordination of CoA at Ni_p for formation of acetyl-CoA and maybe also for the acetyl-CoA binding in the reverse reaction.

It cannot be clearly answered whether the CO or CoA bound state are of catalytical relevance by the structure alone. On the one hand, CO binding which produces the mentioned NiFeC signal appears at catalytic competent ratios [152, 163]. On the other hand, CO treatment can also lead to an inhibited state, when it binds as first substrate to ACS [151, 153, 158] because of a lower nucleophilicity of Ni^{+} for the methylation reaction.

CoA acts as a competitive inhibitor in the CO/acetyl-CoA exchange reaction, most likely through the competition between acetyl-CoA and CoA for the same catalytic site of ACS_{open}. But CoA binding is insufficient to inhibit already carbonylated ACS, as carbonylation requires ACS_{closed}, which might not be accessible for the CoA bound state. However, CoA binding can alter the NiFeC signal if it is incubated as first substrate and changes the NiFeC signal [150, 159] to a NiFeC signal designated as type II. ACS that shows the signal type II does not perform the carbonyl exchange with [1-^{14}C]-Acetyl-CoA, as it was shown with $ACS_{Ch}\Delta N$ (N-terminal domain deletion) and the ACDS β–subunit of *M. thermophila* [75]. Because both variants are lacking the N-terminal domain and cannot obtain the closed conformation, CO can only attack from the solvent site [75]. This situation is comparable with CoA binding first at ACS_{open} and hinders conformational change to ACS_{closed}. It supports the idea that ACS has a mechanism to distinguish between CO approaching from the tunnel or solvent site and with that controlling if CO acts as an inhibitor or substrate [149]. This mechanism could be the coordination of M_p.

4.3 Role of Ni_p in the mechanism of ACS

Crystal structures that contain Zn and Cu at the M_p position always show ACS in the closed conformation as the Zn bound structure of ACS_{Ch} in this work [62, 68]. Despite the fact that these metal-contaminated ACS variants are not active, and from a biological point of view not relevant, their chemistry hints at a clue for the trigger of the conformational change between the ACS_{open} and ACS_{closed} state. Cu and Zn are both d^{10} transition metals, which favor a tetrahedral geometry and were never found in ACS_{open} states, give rise to the question: Is the closed state triggered by the tetrahedral geometry of the M_p or vice versa? In contrast to Zn^{2+} and Cu^{+}, Ni^{2+} has a $3d^8$ electron configuration, able to adopt a square planar and a tetrahedral coordination [164]. This unique flexibility among biologically available transition metals could explain the one or the other of Ni_p as only cofactor which results in an active enzyme. This is accomplished through the minor energy difference between tetrahedral and square-planar coordination and is known for several four-coordinated Ni^{2+} complexes in solution [165]. These Ni complexes can surpass this small energy barrier, existing in an equilibrium of tetrahedral and square-planar coordination[166, 167].

The inability to obtain a square planar coordination leads to the inability to change into the open conformation and hinders to interact with the required substrate for catalysis, which emphasizes the evolutionary importance of Ni as transition metal and the uselessness of d^{10} metals like Cu^{1+} or Zn^{2+}. Both coordination, the square-planar and tetrahedral coordination are maintained after CO and CoA binding for the respective structures reported in this study.

The distances of Ni_p-Ni_d and Ni_p-Fe are the best markers to see structural changes in cluster A and with that the conformational switch in ACS. The Ni_p-Ni_d distance shortens from 3.0 to 2.8 Å from the square planar to the tetrahedral coordination and the Ni_p-Fe distance extends from 2.7 Å in the square planar to 3.9 Å in the tetrahedral coordination (Fig. 24). EXAFS studies on ACS_{Ch} have also reported a shortening of the Ni-Ni distance during CO treatment from 2.96 to 2.78 Å, most likely through the conformational switch from the open to the closed conformation, induced by CO binding [152]. IR spectroscopy experiments with ACS_{Ch} identified a specific band at 1994.7 cm^{-1} under CO treatment, most likely corresponding to a linearly bound CO at Ni [163], as in the CO treated crystal structure (ACS_{closed}:CO Fig. 16D) [163]. In contrast, Ni_d stays in all structures in the square planar coordination. Previous X-ray absorption near edge spectroscopy (XANES), extended X-ray absorption fine structure (EXAFS), EPR and density functional theory (DFT) calculation have already proposed a mixture of a tetrahedrally and square planar coordinated Ni ion upon CO binding: the distorted tetrahedral coordination of Ni_p and the square planar coordination of Ni_d [90, 152, 168, 169].

Nevertheless, the answer to questions about what triggers such conformational changes remain elusive. Based on EXAFS studies [152], neither oxidation nor reduction condition changed the coordination environment of the cluster A (ACS_{open}). However, under reducing conditions with simultaneous CO treatment, the coordination sphere of the cluster A (ACS_{closed}) changed, which indicates a transition of ACS_{open} to ACS_{closed}. Thus, CO binding could be essential for the conformational change, but the untreated ACS crystal that has both positions occupied with nickel ions and a water ligand in the coordination sphere of the distorted tetrahedral Ni_p argue against a conformational change from $ACS_{Ch\text{-}open}$ to $ACS_{Ch\text{-}closed}$ through CO binding. An additional argument that CO binding could not induce the $ACS_{Ch\text{-}closed}$ state is the molecular tunnel that delivers the CO molecule to the Ni_p site. Since this tunnel is blocked in the $ACS_{Ch\text{-}open}$ state, CO cannot bind to the Ni_p at this site which is protected by the Phe_{515} residue to induce the tetrahedral geometry and the $ACS_{Ch\text{-}closed}$ state. Additionally, the monofunctional ACS_{Ch} is able to adopt the closed state without CODH, which rules out the possibility that this state is induced by CODH. There is most likely another trigger that is responsible for the ACS_{open} and ACS_{closed} conformational switch, accompanied by a change of the coordination sphere of Ni_p.

The oxidation state of the Ni_p for the untreated ACS_{closed} and ACS_{open} is most likely the Ni^{2+} state, even under crystallization with titanium citrate as reducing agent, because Ni^{2+} is difficult to reduce without CO stabilizing Ni^{+} that is produced according to the NiFeC signal during CO binding [152]. Additionally, Ti(III)citrate should not be stable enough as reducing agent during crystallization experiments that last several days. It should be noted here that determination of the exact oxidation states for the Ni_p in all structures of this work are not possible using only crystal structures.

In conclusion, the monofunctional ACS_{Ch} attains at least two conformations that could be relevant for catalysis and faces the problem of interacting with three different substrates in a reaction cycle, leading to product formation. Substrates or intermediate states can also act as inhibitors, making it difficult to describe the nature of the random sequential mechanism of ACS. The catalysis is most likely accomplished by ACS interacting with a specific substrate in a certain conformation at the Ni_p site. It can be assumed that ACS exists in solution at equilibrium of the open conformation with a square-planar and the closed conformation with a distorted tetrahedral coordinated Ni_p. Depending on specific conditions, substrate/product concentration or interaction with certain proteins, such as CoFeSP, this equilibrium is shifted towards the required direction. Likely, the crystallization conditions in this work could have acted as a selector to drive ACS_{Ch} into a certain conformation during crystallogenesis.

5 Outlook

The results of this work are the first substrate bound structures of ACS, which are lacking in the field of ACS research. There are recently published approaches to attempting to fill these gaps by negative-stain cryo EM and crystallography of carbonylated ACS of the ACS/CODH complex from *M. thermoacetica* [71, 155]. The resolution of the CO bound ACS/CODH complex has a resolution of 2.47 Å, making it even harder to unambiguously define the ligand as CO without any CO free structure for comparison.

Nevertheless, the generation of CO-soaked crystals in this work does not unambiguously show the carbonylated ACS state. However, the soaking approach can be used for further IR experiments on crystals to support these results with the specific CO stretch signal that should be observable as in ACS in solution. Since proteins in crystals are less flexible due to the crystal packing, a switch from the open to the closed conformation and vice versa can be excluded to happen in the crystal.

In this work, crystallization conditions are defined, generating crystals containing only the open or closed conformation of ACS_{Ch}. These crystals could be used for spectroscopy measuring only one conformation, making it possible to assign experimental data to one specific conformational state. The mentioned IR approach at differently treated crystals could be further used to investigate a possible binding of CO to ACS_{open}.

This work provided further insights into the binding site of CoA. Since the crystal alone does not show all features of the ligand, further improvements of the co-crystallization experiments with higher CoA concentration could lead to a higher occupancy in the crystal, resulting in a better map and giving more insights into the coordination of CoA. Additionally, mutation studies of Arg_{408} and Arg_{409} with negatively charged amino acids, such as glutamate or aspartate, could be combined with the established ITC experiment to investigate the importance of these residues for CoA binding.

In addition to the interaction of ACS with different ligands, one of the most important topics that should be focused on in future studies is the trigger that induces the open or closed conformation of ACS, as this is most likely one of the fundamental mechanisms leading to the understanding of the catalytic cycle. As there are contradictory results in the literature and discussion about the catalytic cycle, especially about the nature of Ni^{+}-CO as described in the dia- and paramagnetic mechanism. Gaining an understanding of the conditions leading to a certain conformation could result in a reinterpretation of previous results and clarify the fundamental problems of the proposed mechanisms.

Appendix

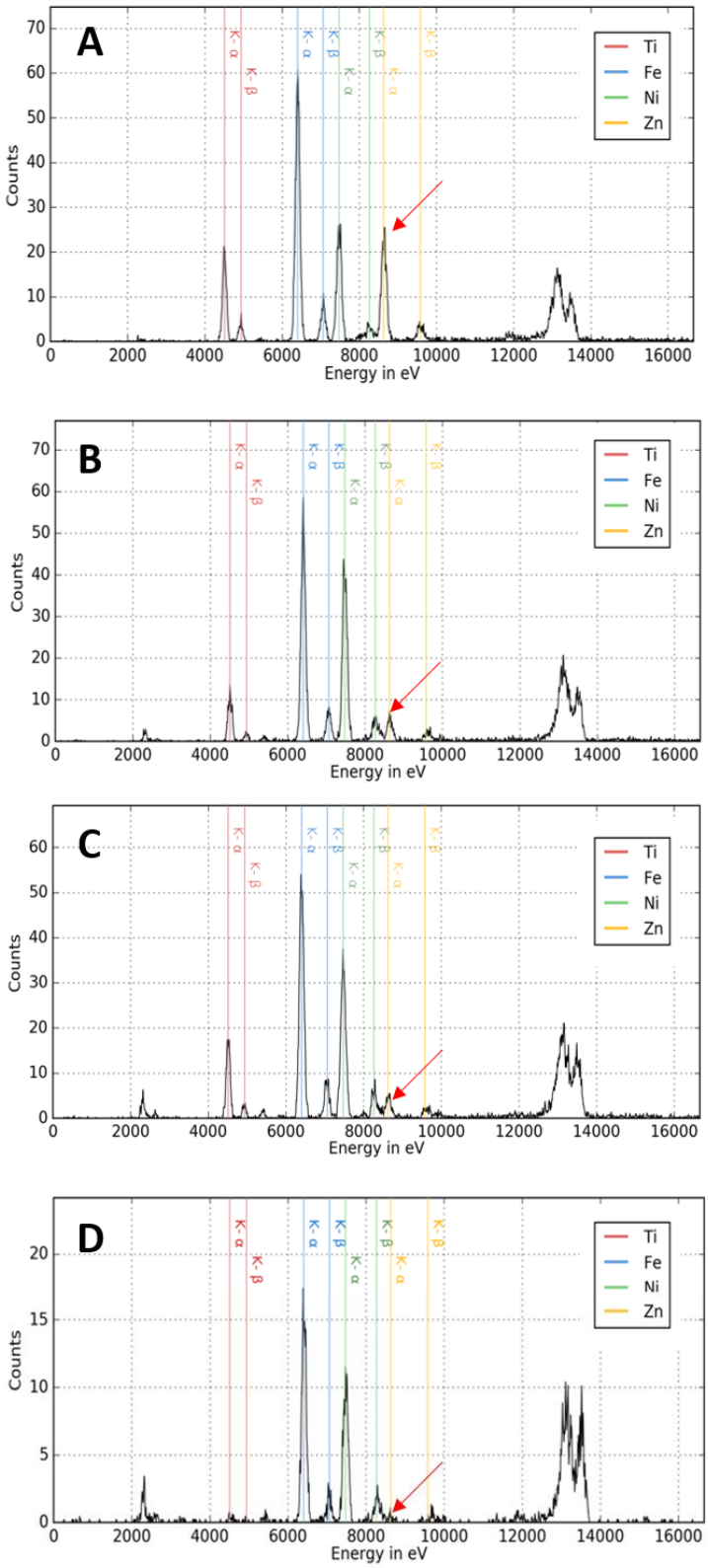

Figure 25: XRF spectra of ACS_{Ch} crystals. A) Crystal with Zn at the proximal position. B) Untreated crystal with Ni at the proximal position C) CO treated crystal D) Co-crystallization of ACS and CoA. The red arrow marks the x-ray transition of the K-α corresponding to Zn.

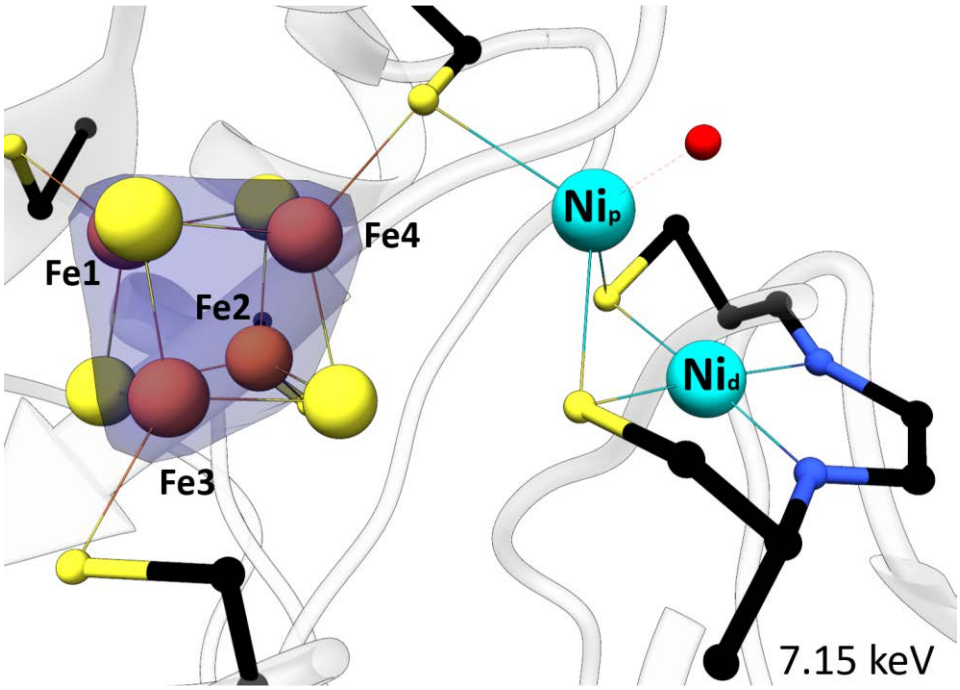

Figure 26: Anomalous map to identify the [4Fe-4S] cluster at cluster A. Ball-and-stick presentation of the cluster A. An anomalous difference map is shown as dark blue surface for data collected at 7.15 keV (contoured at 4.0 σ). The K-absorption edge energy for Fe is 7.11 keV [135-137]. Same color code as in Figure 4.

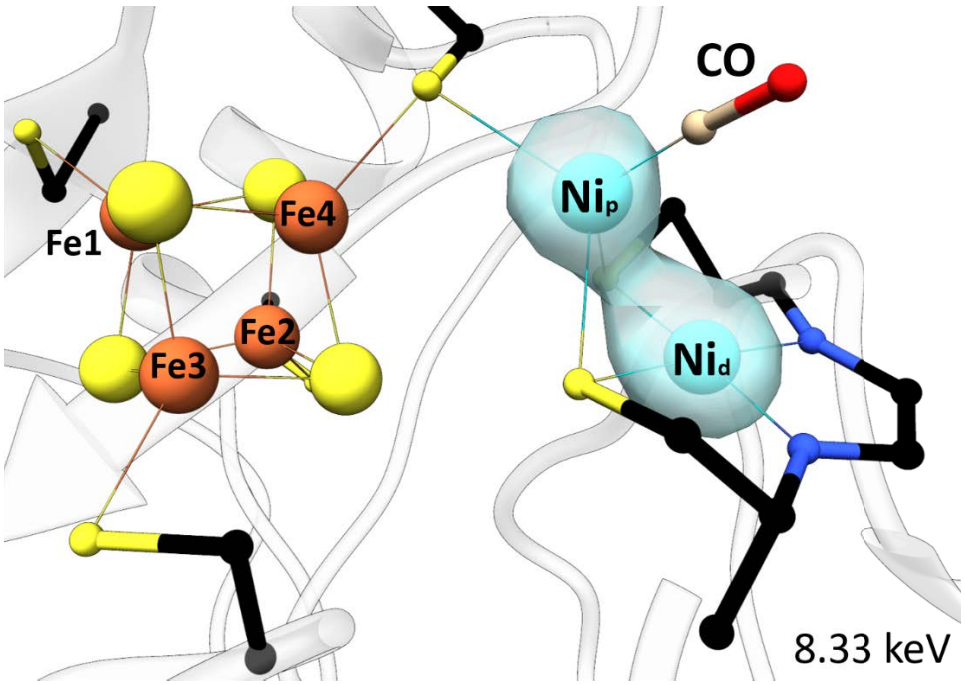

Figure 27: Anomalous map to identify the Ni_p and Ni_d at cluster A of ACS_{Ch}: CO. Ball-and-stick presentation of the cluster A. An anomalous difference map is shown as cyan surface for data collected at 8.33 keV (contoured at 7.0 σ). The K-absorption edge energy for Ni is 8.33 keV [135-137]. Same color code as in Figure 16.

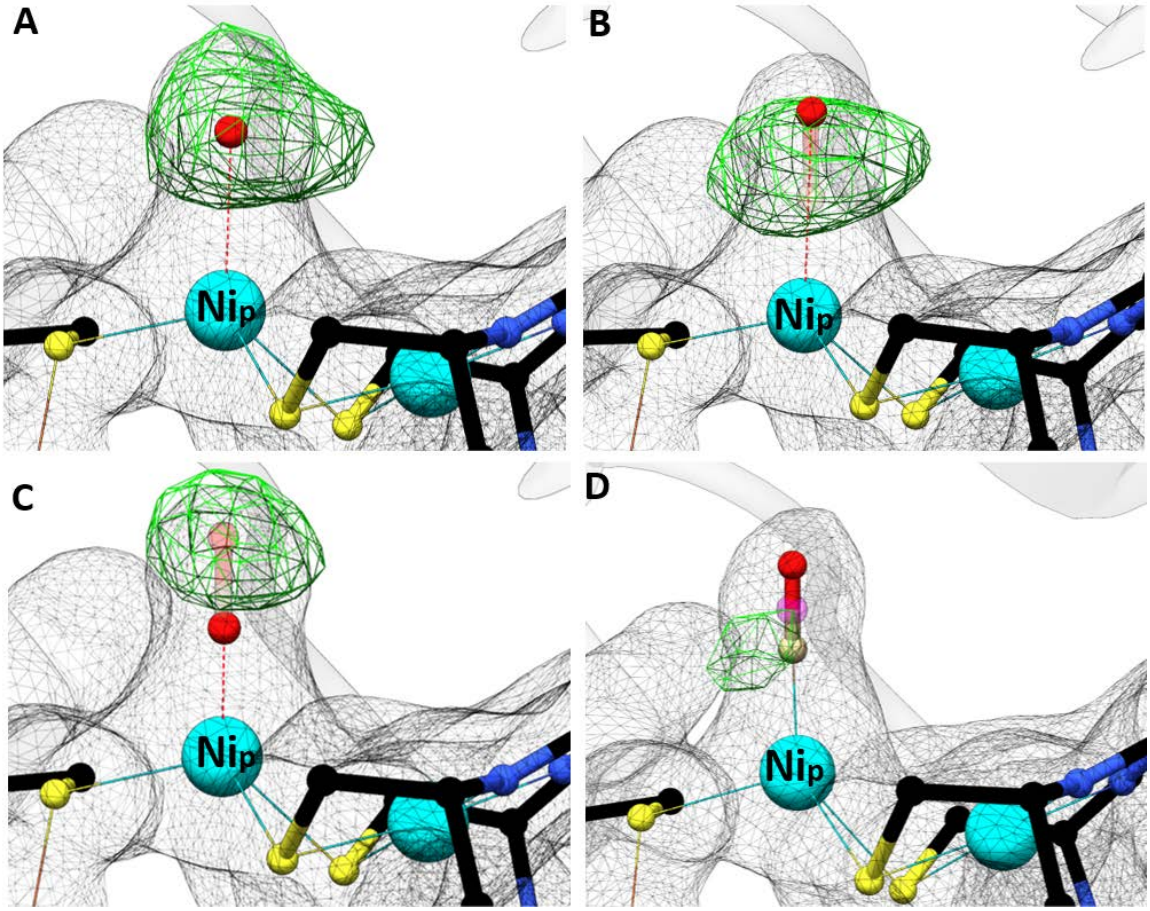

Figure 28: Refinements with different molecules to the observed positive electron density in Figure 16B are shown: Refinement with a water without any restraints (A), water at the oxygen position of CO (B) and water at the carbon position of CO (C). Superposition of $ACS_{Ch\text{-}closed}$ CO bound with $ACS_{Ch\text{-}closed}$ untreated structure of chain B (D). Atoms are color-coded as in Figure 16, except oxygen ligand of the superposition of CO-treated and untreated refinement (magenta). $2F_o$-F_c map is shown as black mesh contoured at 1.0 σ and F_o-F_c map is shown as green mesh at 3.0 σ. The maps were adjusted according to the maps comparison tool of the phenix suite, with the untreated structure as reference.

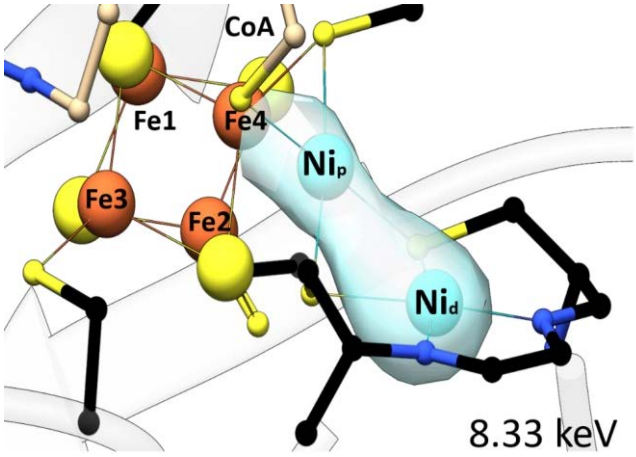

Figure 29: Anomalous map to identify the Ni_p and Ni_d at cluster A of ACS_{Ch}: CoA. Ball-and-stick presentation of the cluster A. An anomalous difference map is shown as cyan surface for data collected at 8.33 keV (contoured at 5.0 σ). The K-absorption edge energy for Ni is 8.33 keV [135-137]. Same color code as in Figure 20.

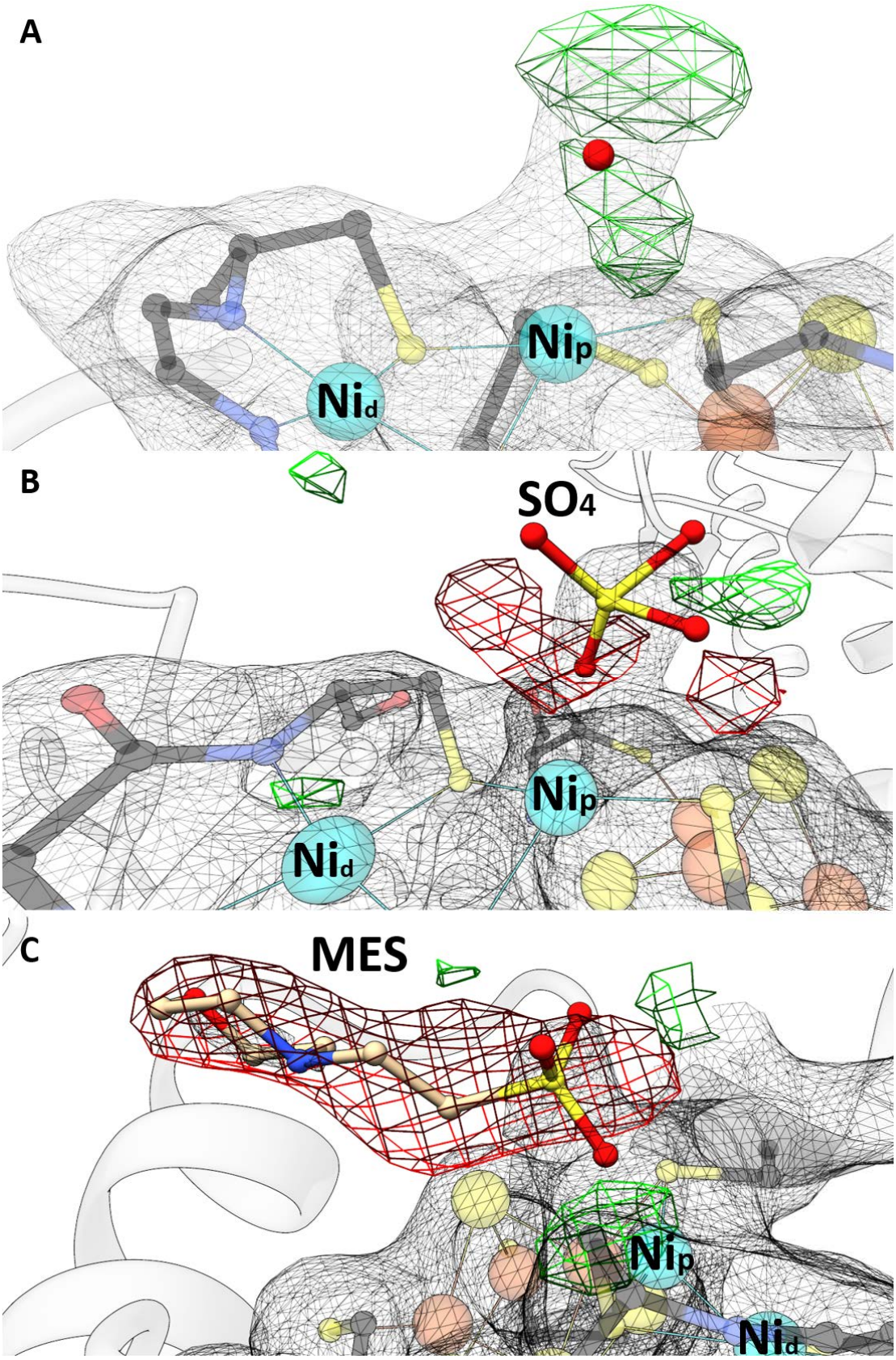

Figure 306: Alternative ligand refinement of $ACS_{Ch\text{-}open}$ A) Water as ligand instead of CoA result in remaining positive electron density at Ni_p. B) SO_4 as ligand instead of CoA. C) MES as ligand instead of CoA. Models of B and C result in appearing of negative electron density. $2F_o$-F_c is shown as black mesh (contoured at 1.0 σ) +/- F_o-F_c is shown as green and red mesh (contoured at +/- 3.0 σ). Same color code as in Figure 19, except carbon atom of MES (light brown).

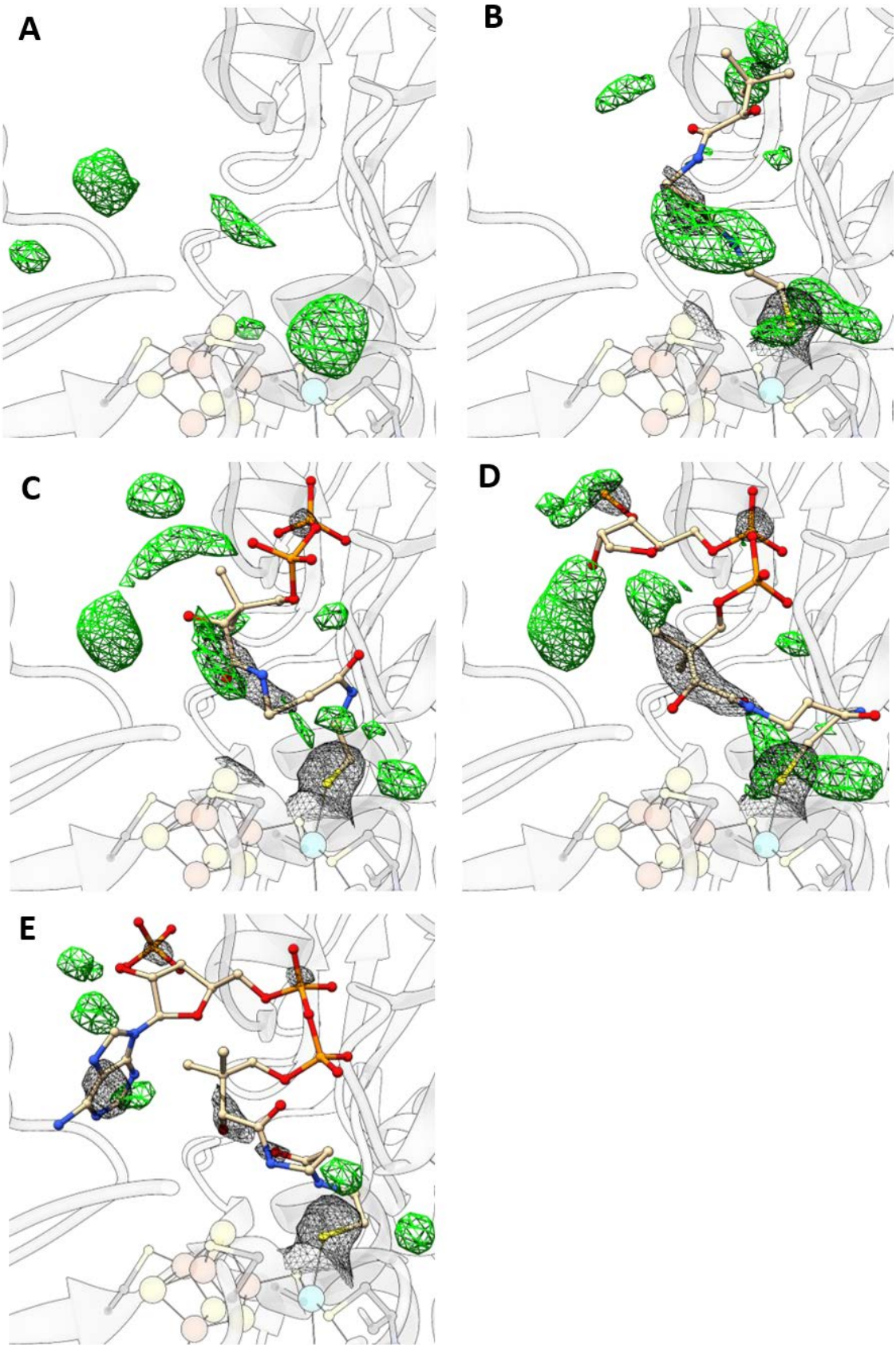

Figure 317: Stepwise CoA modelling as fourth ligand of Ni_p. CoA binds with its sulfur atom at Ni_p. The progress from no ligand (A) to fully modelled CoA (E) is shown. Each modelling step results in new positive electron density appearing in the F_o-F_c map and guides further building steps. $2F_o$-F_c map is shown as black mesh contoured at 1.0 σ and F_o-F_c map is shown as green mesh contoured at +/-3.0 σ. Color is coded as in Figure 16, except P in orange and carbon atoms of CoA in light brown.

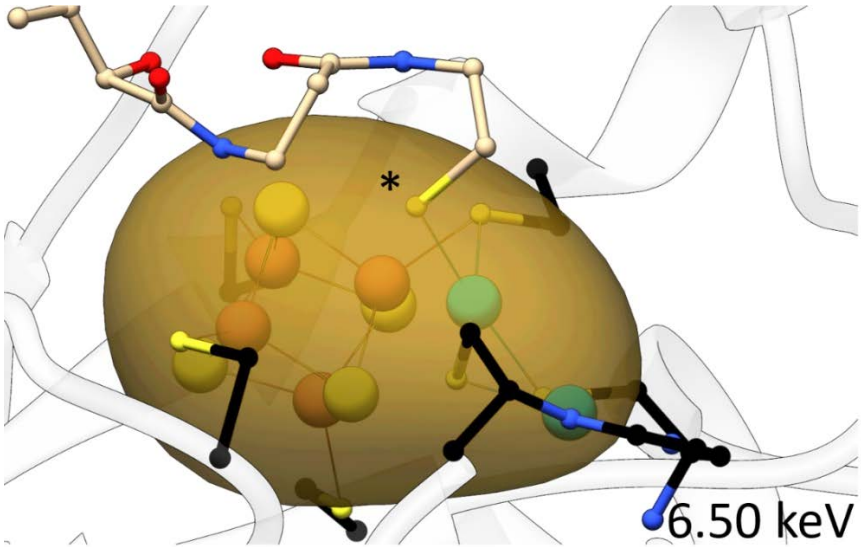

Figure 32: Anomalous data for S at cluster A with CoA bound. The CoA sulfur is inside the bulk density of the anomalous difference map. Stick presentation of cluster A. The anomalous difference map (contoured at 3.0 σ) for the S-K-edge is shown as golden surface and the data has been collected at 6.50 keV. Same color code as in Figure 20.

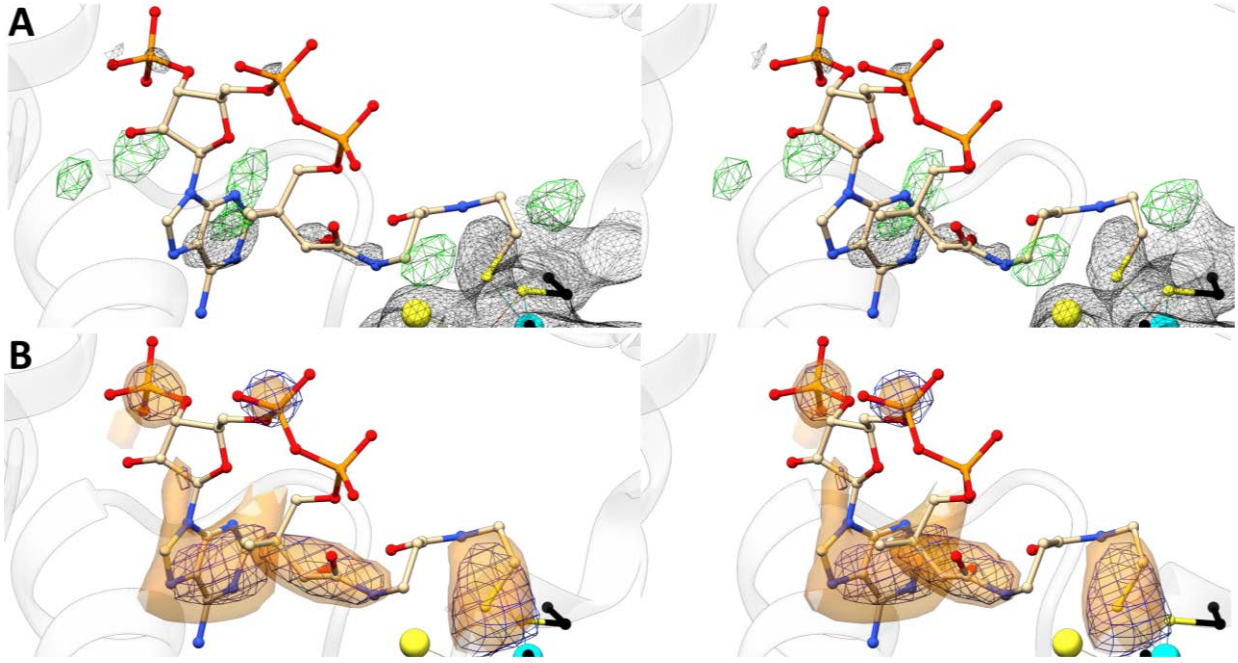

Figure 33: Stereo view of different maps for CoA. A) $2F_o$-F_c map in black mesh (contoured at 1.0 σ) and F_o-F_c map in green mesh (contoured at 3.0 σ) after full refinement with complete CoA molecule. B) Calculated polder and omit map of the model in A. Omit map in dark blue mesh and the polder in orange surface are contoured at 3.0 σ. Models are color-coded as in Figure 20.

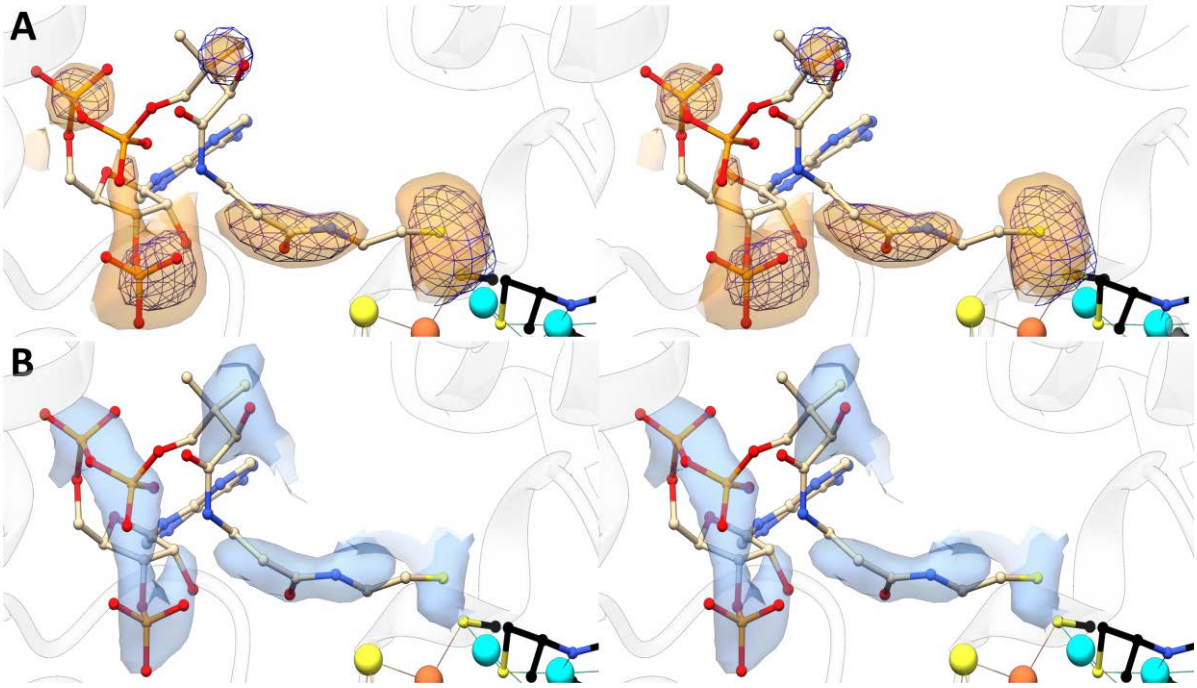

Figure 34: Stereo view of different maps for alternative CoA conformation. A) Calculated polder and omit map of the CoA model. Omit map in dark blue mesh and the polder map in orange surface are contoured at 3.0 σ. B) Calculated FEM for the CoA model in A. FEM in dark blue surface are contoured at 1.0 σ. The FEM map was adjusted according to the maps comparison tool of the phenix suite [130], with the $2F_o$-F_c map contoured at 1.0 σ as reference. Models are color-coded as in Figure 20.

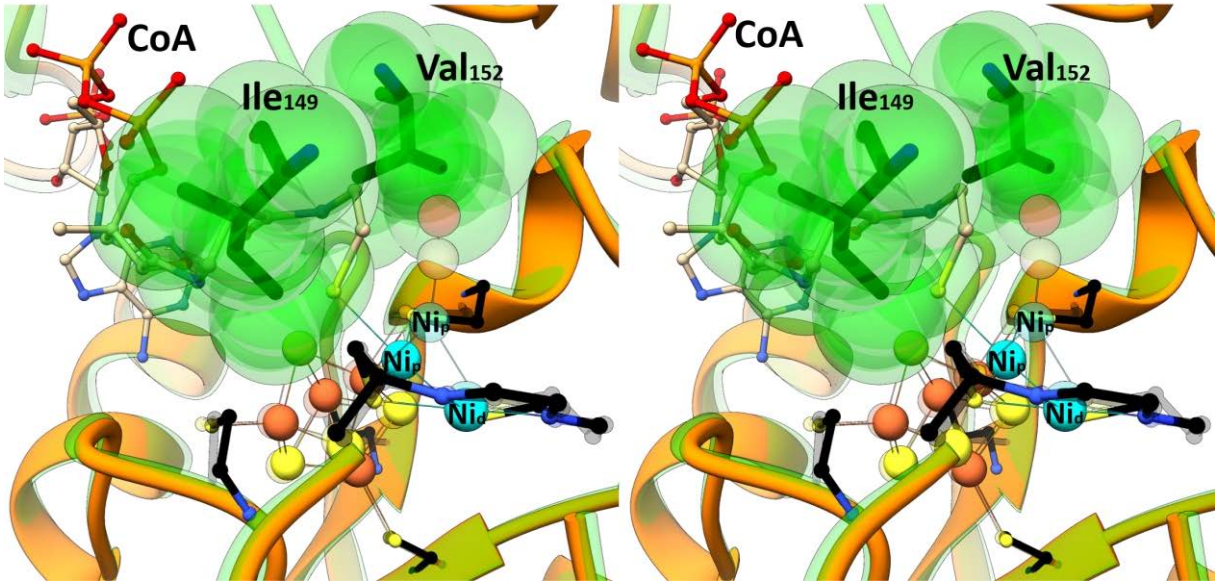

Figure 35: Stereo view of the clash of the CoA bound $ACS_{Ch\text{-}open}$ crystal structure with the CO bound $ACS_{Ch\text{-}closed}$ structure. Same color code as in Figure 14 except that carbon from CO and CoA is shown in light brown. Van der Waals radii of $ACS_{Ch\text{-}closed}$ Ile_{149} and Val_{152} are shown as spheres. The arrangement of Ile_{149} and Val_{152} in the closed conformation would hinder a binding of CoA at the Ni_p in this conformation.

Table 10: Statistics on diffraction data and structure refinement.

Dataset	ACSCh:Zn	ACSCh:Ni	ACSCh:CO	ACSCh:CoA
PDB-Id	7NZ5	7NYP	7NYS	7O0D
Wavelength (Å)	0.9184	0.9184	0.9184	0.9184
Resolution range (Å)	46.19 - 1.90 (1.95 - 1.90)	46.43 - 2.10 (2.16 - 2.10)	48.56 - 2.00 (2.05 – 2.00)	48.88 - 2.30 (2.36 - 2.30)
Space group	$P2_12_12_1$	$P2_12_12_1$	$P2_12_12_1$	$H3_2$
Unit cell a b c (Å) α β γ (°)	69.246 98.811 238.875 90 90 90	69.95 99.478 238.289 90 90 90	70.276 99.233 238.584 90 90 90	199.344, 199.344, 168.268 90, 90, 120
Total reflections	254264 (17961)	189853 (18360)	221837 (15491)	112968 (7592)
Unique reflections	127825 (9008)	96729 (9478)	112519 (7917)	56520 (3807)
Completeness (%)	98.5 (98.3)	98.8 (97.7)	99.2 (99.4)	99.5 (95.3)
Mean I/sigma(I)	9.4 (1.1)	8.6 (1.1)	9.1 (1.0)	22.4 (1.3)
Wilson B-factor	19.93	38.11	33.21	78.81
R-meas	4.4 (63.8)	5.6 (84.9)	6.7 (88.9)	3.8 (83.3)
R-pim	4.4 (45.1)	3.9 (84.9)	4.8 (62.9)	2.7 (58.9)
CC1/2	99.9 (83.9)	99.9 (58.5)	99.9 (57.4)	1.00 (61.3)
Reflections used in refinement	114271 (3298)	80231 (2079)	95920 (1940)	51734 (1823)
Reflections used for R-free	1897 (55)	1887 (49)	1927 (40)	1960 (71)
R-work	0.1933 (0.260)	0.1985 (0.2549)	0.1842 (0.2472)	0.1964 (0.2703)
R-free	0.2239 (0.376)	0.2435 (0.3923)	0.2214 (0.2873)	0.2218 (0.3462)
Number of non-hydrogen atoms	13228	12620	13255	6262
macromolecules	11532	11532	11525	5766
ligands	20	20	24	15
solvent	798	1068	1706	481
Protein residues	1676	1458	1463	728
RMS bonds distances	0.011	0.008	0.008	0.004
RMS bond angles	1.224	1.243	0.977	0.794
Ramachandran favored (%)	97.94	97.73	97.80	96.42
Ramachandran allowed (%)	1.78	1.99	1.92	3.03
Ramachandran outliers (%)	0.28	0.28	0.28	0.55
Rotamer outliers (%)	0.41	0.25	0.16	0.82
Clashscore	8.83	7.81	7.01	5.36
Average B-factor	26.01	38.11	33.21	77.87
macromolecules	24.85	37.60	32.12	79.32
ligands	51.84	80.26	65.10	66.68

Table 11: List of residues which are involved in interdomain contacts of ACS_{Ch} for each domain. Residues written in red are involved in the $ACS_{Ch\text{-}closed}$ conformation, blue in $ACS_{Ch\text{-}open}$ conformation and green in both conformations.

N-Domain	C-Domain	Middle Domain
Arg_{250}	Ser_{514} Phe_{515} Pro_{517}	
Val_{152}	Ser_{514} Phe_{515}	
Tyr_{246}	Phe_{515}	
Arg_{145}	Gly_{599} Ala_{635} Phe_{631}	
Pro_{142}	Ser_{632} Arg_{619}	
Phe_{232}	Gly_{599} Ala_{516} Phe_{515} Cys_{598} Cys_{600} Ser_{514} Pro_{517}	
Asp_{141}	Ser_{632}	
Ala 62	Ser_{632} Thr_{633}	
Gln_{146}	Arg_{619}	
Ile_{149}	Cys_{600}	
Met_{231}	Gly_{640}	
Asp_{60}	Ser_{632}	
Met_{151}	Phe_{515}	
Trp_{154}	Ser_{514}	
Gly_{233}	Phe_{515}	
Tyr_{63}	Gly_{636}	
Asp_{153}	Ser_{514}	
Gly_{233}	Pro_{517}	
Ile_{149}	Phe_{515}	
Lys_{150}		Glu_{332} Tyr_{416}
Asp_{177}		Asn_{326}
Tyr_{207}		Ala_{330}
Gly_{181}		Phe_{327} Asn_{326}
Lys_{202}		Glu_{418} Glu_{334}
Thr_{155}		Tyr_{416} Pro_{329}
Gly_{183}		Pro_{329}
Tyr_{207}		Ala_{330}
Ile_{208}		Ala_{330} Pro_{329}
Asp_{206}		Ala_{330}
Lys_{182}		Ile_{316}
	Glu_{544}	Gln_{399} Phe_{402}
	Ala_{533}	Arg_{408}
	Asp_{538}	Arg_{408}
	Ile_{545}	Ser_{461} Ile_{462} Phe_{402}
	Ala_{541}	Val_{405} Phe_{402}
	Leu_{537}	Leu_{495} Leu_{498} Arg_{494}

Literature

[1] H. Sun, Z.-F. Chai, *Annual Reports Section "A" (Inorganic Chemistry)* **2010**, *106*, 20.

[2] M. Stillman, *Angewandte Chemie International Edition* **2007**, *46*, 8741-8742.

[3] C. Andreini, I. Bertini, G. Cavallaro, G. L. Holliday, J. M. Thornton, *JBIC Journal of Biological Inorganic Chemistry* **2008**, *13*, 1205-1218.

[4] R. Ge, H. Sun, *Accounts of Chemical Research* **2007**, *40*, 267-274.

[5] N. D. Chasteen, *Met Ions Biol Syst* **1998**, *35*, 479-514.

[6] A. R. Muok, Y. Deng, V. M. Gumerov, J. E. Chong, J. R. DeRosa, K. Kurniyati, R. E. Coleman, K. M. Lancaster, C. Li, I. B. Zhulin, B. R. Crane, *Proc Natl Acad Sci U S A* **2019**, *116*, 14955-14960.

[7] L. Casalot, *Trends in Microbiology* **2001**, *9*, 228-237.

[8] R. A. Pufahl, *Science* **1997**, *278*, 853-856.

[9] H. K. Song, S. B. Mulrooney, R. Huber, R. P. Hausinger, *J Biol Chem* **2001**, *276*, 49359-49364.

[10] S. C. Andrews, A. K. Robinson, F. Rodríguez-Quiñones, *FEMS Microbiology Reviews* **2003**, *27*, 215-237.

[11] N. S. Dosanjh, S. L. Michel, *Curr Opin Chem Biol* **2006**, *10*, 123-130.

[12] A. L. Sommer, C. B. Lipman, *Plant Physiology* **1926**, *1*, 231-249.

[13] J. McHargue, *American Journal of Physiology-Legacy Content* **1926**, *77*, 245-255.

[14] R. Bartha, E. Ordal, *Journal of bacteriology* **1965**, *89*, 1015-1019.

[15] R. P. Hausinger, *JBIC Journal of Biological Inorganic Chemistry* **1997**, *2*, 279-286.

[16] R. Watt, P. Ludden, *Cellular and Molecular Life Sciences CMLS* **1999**, *56*, 604-625.

[17] T. Eitinger, M. A. Mandrand-Berthelot, *Archives of Microbiology* **2000**, *173*, 1-9.

[18] A. M. Appel, J. E. Bercaw, A. B. Bocarsly, H. Dobbek, D. L. DuBois, M. Dupuis, J. G. Ferry, E. Fujita, R. Hille, P. J. A. Kenis, C. A. Kerfeld, R. H. Morris, C. H. F. Peden, A. R. Portis, S. W. Ragsdale, T. B. Rauchfuss, J. N. H. Reek, L. C. Seefeldt, R. K. Thauer, G. L. Waldrop, *Chemical Reviews* **2013**, *113*, 6621-6658.

[19] L. Macomber, R. P. Hausinger, *Metallomics* **2011**, *3*, 1153.

[20] S. L. Clugston, J. F. Barnard, R. Kinach, D. Miedema, R. Ruman, E. Daub, J. F. Honek, *Biochemistry* **1998**, *37*, 8754-8763.

[21] Y. Dai, P. C. Wensink, R. H. Abeles, *J Biol Chem* **1999**, *274*, 1193-1195.

[22] E. L. Carter, N. Flugga, J. L. Boer, S. B. Mulrooney, R. P. Hausinger, *Metallomics* **2009**, *1*, 207-221.

[23] H. D. Youn, E. J. Kim, J. H. Roe, Y. C. Hah, S. O. Kang, *Biochem J* **1996**, *318 (Pt 3)*, 889-896.

[24] P. M. Vignais, B. Billoud, *Chem Rev* **2007**, *107*, 4206-4272.

[25] E. Oelgeschläger, M. Rother, *Archives of Microbiology* **2008**, *190*, 257-269.

[26] S. W. Ragsdale, *J Inorg Biochem* **2007**, *101*, 1657-1666.

[27] B. Jaun, R. K. Thauer, *Nickel and its surprising impact in nature* **2007**, *2*, 323-356.

[28] B. Desguin, P. Goffin, E. Viaene, M. Kleerebezem, V. Martin-Diaconescu, M. J. Maroney, J.-P. Declercq, P. Soumillion, P. Hols, *Nature communications* **2014**, *5*, 1-12.

[29] H. Merkens, R. Kappl, R. P. Jakob, F. X. Schmid, S. Fetzner, *Biochemistry* **2008**, *47*, 12185-12196.

[30] H. Guldan, R. Sterner, P. Babinger, *Biochemistry* **2008**, *47*, 7376-7384.

[31] Q. Xu, R. Schwarzenbacher, S. S. Krishna, D. McMullan, S. Agarwalla, K. Quijano, P. Abdubek, E. Ambing, H. Axelrod, T. Biorac, J. M. Canaves, H. J. Chiu, M. A. Elsliger, C. Grittini, S. K. Grzechnik, M. DiDonato, J. Hale, E. Hampton, G. W. Han, J. Haugen, M. Hornsby, L. Jaroszewski, H. E. Klock, M. W. Knuth, E. Koesema, A. Kreusch, P. Kuhn, M. D. Miller, K. Moy, E. Nigoghossian, J. Paulsen, R. Reyes, C. Rife, G. Spraggon, R. C. Stevens, H. van den Bedem, J. Velasquez, A. White, G. Wolf, K. O. Hodgson, J. Wooley, A. M. Deacon, A. Godzik, S. A. Lesley, I. A. Wilson, *Proteins* **2006**, *64*, 808-813.

[32] J. H. Jeoung, D. Nianios, S. Fetzner, H. Dobbek, *Angew Chem Int Ed Engl* **2016**, *55*, 3281-3284.

[33] M. M. He, S. L. Clugston, J. F. Honek, B. W. Matthews, *Biochemistry* **2000**, *39*, 8719-8727.

[34] M. A. Pearson, L. O. Michel, R. P. Hausinger, P. A. Karplus, *Biochemistry* **1997**, *36*, 8164-8172.

[35] J. Wuerges, J. W. Lee, Y. I. Yim, H. S. Yim, S. O. Kang, K. Djinovic Carugo, *Proc Natl Acad Sci U S A* **2004**, *101*, 8569-8574.

[36] J. L. Boer, S. B. Mulrooney, R. P. Hausinger, *Archives of Biochemistry and Biophysics* **2014**, *544*, 142-152.

[37] J. A. Rankin, R. C. Mauban, M. Fellner, B. Desguin, J. McCracken, J. Hu, S. A. Varganov, R. P. Hausinger, *Biochemistry* **2018**, *57*, 3244-3251.

[38] U. Ermler, W. Grabarse, S. Shima, M. Goubeaud, R. K. Thauer, *Science* **1997**, *278*, 1457-1462.

[39] A. Volbeda, E. Garcin, C. Piras, A. L. de Lacey, V. M. Fernandez, E. C. Hatchikian, M. Frey, J. C. Fontecilla-Camps, *J Am Chem Soc* **1996**, *118*, 12989-12996.

[40] V. Svetlitchnyi, H. Dobbek, W. Meyer-Klaucke, T. Meins, B. Thiele, P. Romer, R. Huber, O. Meyer, *Proc Natl Acad Sci U S A* **2004**, *101*, 446-451.

[41] H. Dobbek, V. Svetlitchnyi, L. Gremer, R. Huber, O. Meyer, *Science* **2001**, *293*, 1281-1285.

[42] S. W. Ragsdale, *Journal of Biological Chemistry* **2009**, *284*, 18571-18575.

[43] S. B. Mulrooney, R. P. Hausinger, *FEMS Microbiology Reviews* **2003**, *27*, 239-261.

[44] H. Kaluarachchi, K. C. C. Chung, D. B. Zamble, *Natural product reports* **2010**, *27*, 681-694.

[45] G. Diekert, R. Jaenchen, R. K. Thauer, *FEBS Letters* **1980**, *119*, 118-120.

[46] Y. Zhang, D. A. Rodionov, M. S. Gelfand, V. N. Gladyshev, *BMC Genomics* **2009**, *10*, 78.

[47] E. González-Toril, J. Peretó, in *Encyclopedia of Astrobiology* (Eds.: M. Gargaud, R. Amils, J. C. Quintanilla, H. J. Cleaves, W. M. Irvine, D. L. Pinti, M. Viso), Springer Berlin Heidelberg, Berlin, Heidelberg, **2011**, pp. 131-135.

[48] T. Fenchel, G. M. King, T. H. Blackburn, in *Bacterial Biogeochemistry (Third Edition)* (Eds.: T. Fenchel, G. M. King, T. H. Blackburn), Academic Press, Boston, **2012**, pp. 1-34.

[49] C. A. Carlson, D. A. Hansell, in *Biogeochemistry of Marine Dissolved Organic Matter (Second Edition)* (Eds.: D. A. Hansell, C. A. Carlson), Academic Press, Boston, **2015**, pp. 65-126.

[50] S. H. Fuchs G, *Allgemeine Mikrobiologie, Vol. 8*, **2007**.

[51] I. A. Berg, D. Kockelkorn, W. H. Ramos-Vera, R. F. Say, J. Zarzycki, M. Hugler, B. E. Alber, G. Fuchs, *Nat Rev Microbiol* **2010**, *8*, 447-460.

[52] G. Fuchs, *Annual Review of Microbiology* **2011**, *65*, 631-658.

[53] P. A. Lindahl, B. Chang, *Orig Life Evol Biosph* **2001**, *31*, 403-434.

[54] J. Peretó, *Chemical Society Reviews* **2012**, *41*, 5394.

[55] P. S. Adam, G. Borrel, S. Gribaldo, *Proc Natl Acad Sci U S A* **2018**, *115*, E1166-E1173.

[56] V. A. Svetlichny, T. G. Sokolova, M. Gerhardt, N. A. Kostrikina, G. A. Zavarzin, *Microb Ecol* **1991**, *21*, 1-10.

[57] V. A. Svetlichny, T. G. Sokolova, M. Gerhardt, M. Ringpfeil, N. A. Kostrikina, G. A. Zavarzin, *Systematic and Applied Microbiology* **1991**, *14*, 254-260.

[58] S. W. Ragsdale, E. Pierce, *Biochimica et Biophysica Acta (BBA) - Proteins and Proteomics* **2008**, *1784*, 1873-1898.

[59] S. I. Hu, E. Pezacka, H. G. Wood, *Journal of Biological Chemistry* **1984**, *259*, 8892-8897.

[60] D. Möller-Zinkhan, R. K. Thauer, *Archives of Microbiology* **1990**, *153*, 215-218.

[61] D. A. Grahame, *J Biol Chem* **1991**, *266*, 22227-22233.

[62] C. Darnault, A. Volbeda, E. J. Kim, P. Legrand, X. Vernede, P. A. Lindahl, J. C. Fontecilla-Camps, *Nat Struct Biol* **2003**, *10*, 271-279.

[63] C. M. Gregg, S. Goetzl, J. H. Jeoung, H. Dobbek, *J Biol Chem* **2016**, *291*, 18129-18138.

[64] J. H. Jeoung, T. Giese, M. Grunwald, H. Dobbek, *J Mol Biol* **2010**, *396*, 1165-1179.

[65] J. H. Jeoung, T. Giese, M. Grunwald, H. Dobbek, *Biochemistry* **2009**, *48*, 11505-11513.

[66] S. E. Hennig, S. Goetzl, J. H. Jeoung, M. Bommer, F. Lendzian, P. Hildebrandt, H. Dobbek, *Nat Commun* **2014**, *5*, 4626.

[67] J.-H. Jeoung, S. Goetzl, E. Hennig Sandra, J. Fesseler, C. Wörmann, J. Dendra, H. Dobbek, in *Biological Chemistry, Vol. 395*, **2014**, p. 545.

[68] T. I. Doukov, T. M. Iverson, J. Seravalli, S. W. Ragsdale, C. L. Drennan, *Science* **2002**, *298*, 567-572.

[69] T. I. Doukov, L. C. Blasiak, J. Seravalli, S. W. Ragsdale, C. L. Drennan, *Biochemistry* **2008**, *47*, 3474-3483.

[70] Y. Kung, T. I. Doukov, J. Seravalli, S. W. Ragsdale, C. L. Drennan, *Biochemistry* **2009**, *48*, 7432-7440.

[71] S. E. Cohen, M. Can, E. C. Wittenborn, R. A. Hendrickson, S. W. Ragsdale, C. L. Drennan, *ACS Catalysis* **2020**, *10*, 9741-9746.

[72] O. N. Lemaire, T. Wagner, *Biochimica et Biophysica Acta (BBA) - Bioenergetics* **2021**, *1862*, 148330.

[73] D. A. Grahame, E. DeMoll, *J Biol Chem* **1996**, *271*, 8352-8358.

[74] B. Bhaskar, E. DeMoll, D. A. Grahame, *Biochemistry* **1998**, *37*, 14491-14499.

[75] S. Gencic, E. C. Duin, D. A. Grahame, *J Biol Chem* **2010**, *285*, 15450-15463.

[76] W. Gong, B. Hao, Z. Wei, D. J. Ferguson, Jr., T. Tallant, J. A. Krzycki, M. K. Chan, *Proc Natl Acad Sci U S A* **2008**, *105*, 9558-9563.

[77] J. Seravalli, W. Gu, A. Tam, E. Strauss, T. P. Begley, S. P. Cramer, S. W. Ragsdale, *Proc Natl Acad Sci U S A* **2003**, *100*, 3689-3694.

[78] S. Gencic, D. A. Grahame, *J Biol Chem* **2003**, *278*, 6101-6110.

[79] M. R. Bramlett, X. Tan, P. A. Lindahl, *J Am Chem Soc* **2003**, *125*, 9316-9317.

[80] J. Seravalli, Y. Xiao, W. Gu, S. P. Cramer, W. E. Antholine, V. Krymov, G. J. Gerfen, S. W. Ragsdale, *Biochemistry* **2004**, *43*, 3944-3955.

[81] W. Shin, P. A. Lindahl, *Biochemistry* **1992**, *31*, 12870-12875.

[82] X. Tan, M. R. Bramlett, P. A. Lindahl, *J Am Chem Soc* **2004**, *126*, 5954-5955.

[83] D. P. Barondeau, P. A. Lindahl, *J Am Chem Soc* **1997**, *119*, 3959-3970.

[84] J. Seravalli, M. Kumar, S. W. Ragsdale, *Biochemistry* **2002**, *41*, 1807-1819.

[85] S. Gencic, D. A. Grahame, *Biochemistry* **2008**, *47*, 5544-5555.

[86] J. Seravalli, S. W. Ragsdale, *J Biol Chem* **2008**, *283*, 8384-8394.

[87] S. W. Ragsdale, *Chemical Reviews* **2006**, *106*, 3317-3337.

[88] P. Lindahl, *JBIC Journal of Biological Inorganic Chemistry* **2004**, *9*, 516-524.

[89] E. L. Hegg, *Acc Chem Res* **2004**, *37*, 775-783.

[90] G. Bender, T. A. Stich, L. Yan, R. D. Britt, S. P. Cramer, S. W. Ragsdale, *Biochemistry* **2010**, *49*, 7516-7523.

[91] P. A. Lindahl, E. Munck, S. W. Ragsdale, *J Biol Chem* **1990**, *265*, 3873-3879.

[92] K. C. Terlesky, M. J. Nelson, J. G. Ferry, *J Bacteriol* **1986**, *168*, 1053-1058.

[93] S. Menon, S. W. Ragsdale, *Biochemistry* **1998**, *37*, 5689-5698.

[94] S. Menon, S. W. Ragsdale, *J Biol Chem* **1999**, *274*, 11513-11518.

[95] H. Lebertz, H. Simon, L. F. Courtney, S. J. Benkovic, L. D. Zydowsky, K. Lee, H. G. Floss, *J Am Chem Soc* **1987**, *109*, 3173-3174.

[96] X. S. Tan, C. Sewell, P. A. Lindahl, *J Am Chem Soc* **2002**, *124*, 6277-6284.

[97] C. G. Riordan, *JBIC Journal of Biological Inorganic Chemistry* **2004**, *9*, 542-549.

[98] J. Jones, *Platinum Metals Review* **2000**, *44*, 94-105.

[99] J. F. Roth, *Platinum metals review* **1975**, *19*, 12-14.

[100] M. R. Villarejo, I. Zabin, *Journal of bacteriology* **1974**, *120*, 466-474.

[101] C. Papworth, J. Bauer, J. Braman, *Strategies* **1996**, *9*, 3-4.

[102] M. Wu, Q. Ren, A. S. Durkin, S. C. Daugherty, L. M. Brinkac, R. J. Dodson, R. Madupu, S. A. Sullivan, J. F. Kolonay, W. C. Nelson, L. J. Tallon, K. M. Jones, L. E. Ulrich, J. M. Gonzalez, I. B. Zhulin, F. T. Robb, J. A. Eisen, *PLoS Genetics* **2005**, *1*, e65.

[103] W. Yang, E. Chow, G. D. Willett, D. B. Hibbert, J. J. Gooding, *Analyst* **2003**, *128*, 712-718.

[104] W. Yang, D. Jaramillo, J. J. Gooding, D. B. Hibbert, R. Zhang, G. D. Willett, K. J. Fisher, *Chemical Communications* **2001**, 1982-1983.

[105] M. Nakamura, K. Saeki, Y. Takahashi, *J Biochem* **1999**, *126*, 10-18.

[106] U. K. Laemmli, *Nature* **1970**, *227*, 680-685.

[107] X. Zou, D. R. Evans, K. L. Brown, *Inorganic Chemistry* **1995**, *34*, 1634-1635.

[108] B. B. Buchanan, W. Lovenberg, J. C. Rabinowitz, *Proc Natl Acad Sci U S A* **1963**, *49*, 345-353.

[109] M. M. Bradford, *Analytical Biochemistry* **1976**, *72*, 248-254.

[110] H. C. Gasteiger E., Gattiker A., Duvaud S., Wilkins M.R., Appel R.D., Bairoch A., *Humana Press* **2005**, 571-607.

[111] S. Gencic, D. A. Grahame, *Biochemistry* **2008**, *47*, 5544-5555.

[112] D. A. Grahame, *Methods Enzymol* **2011**, *494*, 189-217.

[113] W. D. Robertson, A. M. Bovell, K. Warncke, *JBIC Journal of Biological Inorganic Chemistry* **2013**, *18*, 701-713.

[114] R. M. C. E. Dawson, Daphne C.; Elliott, William H.; Jones, Kenneth M., *Data for Biochemical Research Vol. 3rd*, Clarendon Press, **2002**.

[115] E. J. van Kampen, W. G. Zijlstra, in *Advances in Clinical Chemistry, Vol. 23* (Eds.: A. L. Latner, M. K. Schwartz), Elsevier, **1983**, pp. 199-257.

[116] S. Keller, C. Vargas, H. Zhao, G. Piszczek, C. A. Brautigam, P. Schuck, *Analytical Chemistry* **2012**, *84*, 5066-5073.

[117] 7.0 ed., OriginLab Corporation, Northampton, MA, USA.

[118] M. Gerlach, U. Mueller, M. S. Weiss, *Journal of large-scale research facilities JLSRF* **2016**, *2*.

[119] H. R. Powell, T. G. G. Battye, L. Kontogiannis, O. Johnson, A. G. W. Leslie, *Nature Protocols* **2017**, *12*, 1310-1325.

[120] K. M. Sparta, M. Krug, U. Heinemann, U. Mueller, M. S. Weiss, *Journal of Applied Crystallography* **2016**, *49*, 1085-1092.

[121] W. Kabsch, *Acta Crystallographica Section D* **2010**, *66*, 133-144.

[122] W. Kabsch, *Acta Crystallographica Section D* **2010**, *66*, 125-132.

[123] I. J. Tickle, Flensburg, C., Keller, P., Paciorek, W., Sharff, A., Vonrhein, C., Bricogne, G., Cambridge, United Kingdom: Global Phasing Ltd., **2018**.

[124] Version 2.1 ed., Helmholtz-ZentrumBerlin.

[125] D. Liebschner, P. V. Afonine, M. L. Baker, G. Bunkóczi, V. B. Chen, T. I. Croll, B. Hintze, L.-W. Hung, S. Jain, A. J. McCoy, N. W. Moriarty, R. D. Oeffner, B. K. Poon, M. G. Prisant, R. J. Read, J. S. Richardson, D. C. Richardson, M. D. Sammito, O. V. Sobolev, D. H. Stockwell, T. C. Terwilliger, A. G. Urzhumtsev, L. L. Videau, C. J. Williams, P. D. Adams, *Acta Crystallographica Section D Structural Biology* **2019**, *75*, 861-877.

[126] A. J. McCoy, R. W. Grosse-Kunstleve, P. D. Adams, M. D. Winn, L. C. Storoni, R. J. Read, *Journal of Applied Crystallography* **2007**, *40*, 658-674.

[127] P. Emsley, B. Lohkamp, W. G. Scott, K. Cowtan, *Acta Crystallogr D Biol Crystallogr* **2010**, *66*, 486-501.

[128] P. V. Afonine, R. W. Grosse-Kunstleve, N. Echols, J. J. Headd, N. W. Moriarty, M. Mustyakimov, T. C. Terwilliger, A. Urzhumtsev, P. H. Zwart, P. D. Adams, *Acta Crystallographica Section D Biological Crystallography* **2012**, *68*, 352-367.

[129] E. F. Pettersen, T. D. Goddard, C. C. Huang, G. S. Couch, D. M. Greenblatt, E. C. Meng, T. E. Ferrin, *J Comput Chem* **2004**, *25*, 1605-1612.

[130] A. Urzhumtsev, P. V. Afonine, V. Y. Lunin, T. C. Terwilliger, P. D. Adams, *Acta Crystallographica Section D: Biological Crystallography* **2014**, *70*, 2593-2606.

[131] S. Götzl, Humboldt-Universität zu Berlin, Lebenswissenschaftliche Fakultät **2014**.

[132] M. K. Johnson, Robinson, A. E., & Thomson, A. J., *Iron-sulfur Proteins*, Wiley-Inter-science, New York, **1982**.

[133] T. Svetlitchnaia, V. Svetlitchnyi, O. Meyer, H. Dobbek, *Proceedings of the National Academy of Sciences* **2006**, *103*, 14331-14336.

[134] J. Seravalli, K. L. Brown, S. W. Ragsdale, *J Am Chem Soc* **2001**, *123*, 1786-1787.

[135] S. Brennan, P. Cowan, *Review of scientific instruments* **1992**, *63*, 850-853.

[136] D. T. Cromer, D. Liberman, *The Journal of Chemical Physics* **1970**, *53*, 1891-1898.

[137] D. T. Cromer, D. A. Liberman, *Acta Crystallographica Section A: Crystal Physics, Diffraction, Theoretical and General Crystallography* **1981**, *37*, 267-268.

[138] E. Krissinel, K. Henrick, *J Mol Biol* **2007**, *372*, 774-797.

[139] L. Pravda, D. Sehnal, D. Toušek, V. Navrátilová, V. Bazgier, K. Berka, R. Svobodová Vařeková, J. Koča, M. Otyepka, *Nucleic Acids Research* **2018**, *46*, W368-W373.

[140] W. K. Russell, P. A. Lindahl, *Biochemistry* **1998**, *37*, 10016-10026.

[141] P. V. Afonine, N. W. Moriarty, M. Mustyakimov, O. V. Sobolev, T. C. Terwilliger, D. Turk, A. Urzhumtsev, P. D. Adams, *Acta crystallographica. Section D, Biological crystallography* **2015**, *71*, 646-666.

[142] D. Liebschner, P. V. Afonine, N. W. Moriarty, B. K. Poon, O. V. Sobolev, T. C. Terwilliger, P. D. Adams, *Acta Crystallographica Section D* **2017**, *73*, 148-157.

[143] T. J. Dolinsky, J. E. Nielsen, J. A. McCammon, N. A. Baker, *Nucleic Acids Research* **2004**, *32*, W665-W667.

[144] N. A. Baker, D. Sept, S. Joseph, M. J. Holst, J. A. McCammon, *Proceedings of the National Academy of Sciences* **2001**, *98*, 10037.

[145] C. Engel, R. Wierenga, *Current Opinion in Structural Biology* **1996**, *6*, 790-797.

[146] F. Mancia, N. H. Keep, A. Nakagawa, P. F. Leadlay, S. McSweeney, B. Rasmussen, P. B. secke, O. Diat, P. R. Evans, *Structure* **1996**, *4*, 339-350.

[147] W. T. Wolodko, M. E. Fraser, M. N. James, W. A. Bridger, *J Biol Chem* **1994**, *269*, 10883-10890.

[148] B. E. Wilson, P. A. Lindahl, *J Biol Inorg Chem* **1999**, *4*, 742-748.

[149] S. A. Raybuck, N. R. Bastian, W. H. Orme-Johnson, C. T. Walsh, *Biochemistry* **1988**, *27*, 7698-7702.

[150] S. W. Ragsdale, H. G. Wood, *J Biol Chem* **1985**, *260*, 3970-3977.

[151] W. P. Lu, S. W. Ragsdale, *J Biol Chem* **1991**, *266*, 3554-3564.

[152] M. Can, L. J. Giles, S. W. Ragsdale, R. Sarangi, *Biochemistry* **2017**, *56*, 1248-1260.

[153] S. Gencic, K. Kelly, S. Ghebreamlak, E. C. Duin, D. A. Grahame, *Biochemistry* **2013**, *52*, 1705-1716.

[154] E. L. Maynard, P. A. Lindahl, *J Am Chem Soc* **1999**, *121*, 9221-9222.

[155] S. E. Cohen, E. J. Brignole, E. C. Wittenborn, M. Can, S. Thompson, S. W. Ragsdale, C. L. Drennan, *Structure* **2020**.

[156] X. Tan, H. K. Loke, S. Fitch, P. A. Lindahl, *J Am Chem Soc* **2005**, *127*, 5833-5839.

[157] C. D. James, S. Wiley, S. W. Ragsdale, B. M. Hoffman, *J Am Chem Soc* **2020**, *142*, 15362-15370.

[158] E. L. Maynard, C. Sewell, P. A. Lindahl, *J Am Chem Soc* **2001**, *123*, 4697-4703.

[159] S. W. Ragsdale, H. G. Wood, W. E. Antholine, *Proc Natl Acad Sci U S A* **1985**, *82*, 6811-6814.

[160] S. Remington, G. Wiegand, R. Huber, *J Mol Biol* **1982**, *158*, 111-152.

[161] T. Shanmugasundaram, G. K. Kumar, B. C. Shenoy, H. G. Wood, *Biochemistry* **1989**, *28*, 7112-7116.

[162] G. C. Tucci, R. Holm, *J Am Chem Soc* **1995**, *117*, 6489-6496.

[163] S. J. George, J. Seravalli, S. W. Ragsdale, *J Am Chem Soc* **2005**, *127*, 13500-13501.

[164] H. B. Gray, C. Ballhausen, *J Am Chem Soc* **1963**, *85*, 260-265.

[165] G. Everett Jr, R. Holm, *J Am Chem Soc* **1965**, *87*, 2117-2127.

[166] R. Holm, K. Swaminathan, *Inorganic Chemistry* **1963**, *2*, 181-186.

[167] R. H. Holm, A. Chakravorty, G. Dudek, *J Am Chem Soc* **1964**, *86*, 379-387.

[168] C. E. Webster, M. Y. Darensbourg, P. A. Lindahl, M. B. Hall, *J Am Chem Soc* **2004**, *126*, 3410-3411.

[169] W. Gu, S. Gencic, S. P. Cramer, D. A. Grahame, *J Am Chem Soc* **2003**, *125*, 15343-15351.

List of Abbreviations

Å	angstrom
aa	amino acids
ACDS	acetyl-CoA decarbonylase/synthase
ACS	acetyl-CoA Synthase
ADP	adenosine diphosphate
APS	ammonium persulfate
ATP	adenosine triphosphate
BSA	bovine serum albumin
BTP	bis(tris(hydroxymethyl)methylamino) propane
Cb	Carbenicillin
Cbd	Cob(I)inamide
cc	correlation coefficient
C. hydrogenoformans	*Carboxydothermus hydrogenoformans*
CoA	coenzyme A
CODH	carbon monoxide dehydrogenase
COM	coenzyme M
CoFeSP	corrinoid iron sulfur protein
CV	column volume
Da	Dalton
DFT	density functional theory
DNA	deoxyribonucleic acid
DT	dithionite
E. coli	*Escherichia coli*
EDTA	ethylenediaminetetraacetic acid
EPR	electron paramagnetic resonance
EXAFS	extended X-ray absorption fine structure
$F_{420}H_2$	cofactor F420, reduced
FAD	flavin adenine dinucleotide
H_4MPT	tetrahydromethanopterin
HEPES	(4-(2-hydroxyethyl)-1-piperazineethanesulfonic acid
IPTG	isopropyl β-D-1-thiogalactopyranoside

ITC	isothermal titration calorimetry
LB	lysogeny broth
Km	Kanamycin
MeCbl	methylcobalamin
MeCbd	methylco(III)binamide
MES	2-(N-morpholino)ethanesulfonic acid
M. thermophila	*Methanosarcina thermophila*
MeTr	methyl transferase
M_d	distal metal
M_p	proximal metal
M. thermoacetica	*Moorella thermoacetica*
NADH	nicotinamide adenine dinucleotide, reduced
Ni_d	distal nickel
Ni_p	proximal nickel
OD_{600}	optical density at 600 nm
PCR	polymerase chain reaction
PDB	protein data bank
PEG	polyethylene glycol
RACo	reductive activator of CoFeSP
RubisCo	Ribulose-1,5-bisphosphate carboxylase-oxygenase
RMS	root-mean-square
Rpm	revolutions per minute
SDS(-PAGE)	sodium dodecyl sulfate (polyacrylamide gel electrophoresis)
SOB	super optimal broth
TAE	Tris-acetate-EDTA
TB	terrific broth
TCEP	tris(2-carboxyethyl)phosphine
TEMED	N,N,N´,N'-tetramethylethylendiamin
Tet	Tetracyclin
TEV protease	tobacco etch virus protease
THF	tetrahydrofolate
Tris	tris(hydroxymethyl)aminomethane
UV/vis	ultraviolet / visible

v/v	volume / volume
w/v	weight / volume
XANES	X-ray absorption near edge spectroscopy
XRF	X-ray fluorescence

List of Figures

List of Tables

Acknowledgements

To begin with, I am thankful to Prof. Dr. Holger Dobbek for provisioning this ambitious and exciting project and for his supervision over the last years.

I am also very grateful to Dr. Jae-Hun Jeoung, who supported and advised me with his sensational expertise, especially in the protein crystallography. I will always enjoy thinking back to long working days at the synchrotron with nice coffee breaks during the nightshifts.

I would like to thank Felix in particular, with whom I went through my time as a PhD student. We shared all the ups and downs, motivated each other, and during this time as colleagues, we became friends.

Jakob Ruickholdt, thanks to you for your unwavering positive thinking. You managed to make me laugh every day and I am grateful that both of us shared the same passion for our favorite hot beverage: coffee.

Rainer is simply the best. He is the most irreplaceable person in the laboratory and always helpful and devoted if someone needs him. Thank you very much for the wonderful time and the experience to working with you.

Many thanks to Gisa and all the wonderful, lovely, and amusing talks in the lab.

A huge “thanks” goes to all other colleagues over the past years who were there for each other every day: Andrew, Barbara, Berta, Frank, Friederike, Julia, Kathryn, Lilith, Martin B., Martin W., Mohammed, Piotr, Sabine, Stefan, Tobias and Yudhajeet.

Naturally, I would also like to thank all student assistants, who contributed notably to the nice atmosphere in the lab, especially Florian, Jakob W. and Sarah.

I am grateful to Jakob R. and Jae-Hun for proofreading my thesis.

Aside from my colleagues, I am thankful for all my friends and my family supporting me this long way by all available means, including and in particular my longstanding friends Stefan A., Jakob D., Jule, Sascha and Steve.

I am very thankful for my girlfriend Sina. It wasn’t always easy for you, but you were always there for me and motivated me to keep going.

Finally, a special thanks to my daughter Milena. You enrich my life every day.

Declaration

Hiermit erkläre ich, dass ich die vorliegende Arbeit selbstständig verfasst und keine anderen als die angegebenen Quellen und Hilfsmittel verwendet habe.

I hereby declare, that I have prepared this work independently, using only references and resources which I marked as such.

Berlin, _____

_____

Julian Kreibich